Particle Trapping Mechanisms in Biological Hydrogels

im Fachbereich Physik der Freien Universität Berlin eingereichte
Dissertation

zur Erlangung des akademischen Grades eines Doktors der
Naturwissenschaften (Dr. rer. nat.)

vorgelegt von
Johann Hansing

Berlin, 2018

Erster Gutachter:	Prof. Dr. Roland R. Netz Freie Universität Berlin
Zweiter Gutachter:	Prof. Dr. Ralf Metzler Universität Potsdam
Tag der Disputation:	29. August 2018

Contents

1. Introduction 1

1.1. Outline of this Work 4

2. Nanoparticle Filtering in Charged Hydrogels: Effects of Particle Size, Charge Asymmetry and Salt Concentration 6

2.1. Introduction 6

2.2. Methods 8

2.2.1. Brownian dynamics simulation 8

2.2.2. Gel model 9

2.2.3. Analytical model 11

2.3. Results 12

2.3.1. Point particles 13

2.3.2. Finite-size particles 16

2.4. Comparison with Experiments 18

2.4.1. Polymer concentration effects 18

2.4.2. Particle size effects 21

2.4.3. Salt concentration effects 22

2.5. Conclusion 26

3. Particle Trapping Mechanisms are Different in Spatially Ordered and Disordered Interacting Gels 28

3.1. Introduction 28

3.2. Methods 30

3.3. Results 31

3.3.1. Purely steric gels 32

3.3.2. Interacting gels 34

3.4. Discussion 41

3.5. Conclusion 44

3.6. Supplementary Information 46

4. Diffusion in Polymer Gels with Mixed Attractive and Repulsive Interactions 47

4.1. Introduction 47

4.1.1. Experimental methods 48

4.1.2. Simulation methods 52

4.2. Results and Discussion 54

4.3. Comparison of experiments and model predictions 58

4.4. Conclusions 60

4.5. Supplementary Information 63

5. Hydrodynamic Effects on Particle Diffusion in Polymeric Hydrogels with Steric and Electrostatic Particle-Gel Interactions 67
5.1. Introduction 67
  5.1.1. Theory 68
  5.1.2. Simulations 70
5.2. Results and Discussion 71
  5.2.1. Purely steric gels 71
  5.2.2. Interacting gels 75
5.3. Summary and Conclusion 81
5.4. Supplementary Information 82

6. Summary and Outlook 87

Appendix A. Saddle-point potential 90

Appendix B. Modified Stokesian dynamics method 93

Appendix C. Ewald sum of the Rotne-Prager tensor 95

Appendix D. Lubrication approximation 97

Appendix E. Mid-point-scheme 100

Appendix F. Precomputing the far-field mobility matrix 101

Appendix G. Hydrodynamic friction during trapping and barrier crossing 102

List of Publications 104

Bibliography 105

Abstract 115

Zusammenfassung 117

Erklärung 119

Danksagung 121

1. Introduction

Understanding solute diffusion in hydrogels, which are polymer networks swollen in water, is a topic of investigation where research from different scientific branches such as physics, chemistry, biology and medicine merges. Biological hydrogels (biogels) are ubiquitously found in biological systems. Prominent examples are the extracellular matrix (ECM), mucus and the vitreous humor, a clear fluid in the mammalian eye. Biogels form selective diffusion barriers in human and animal bodies. They regulate the passage of some particles like signaling proteins and nutrients and can prevent the passage of pathogens, toxic agents and drugs [1]. Thus, biogels serve as biological particle filters and their filtering capabilities are a vital factor for human and animal health. Consequently, it is important for medical purposes to understand why in some cases biogels allow the passage of toxic agents and pathogens. In addition, in pharmaceutical research, it is desirable to design drugs that can traverse biogel barriers, in order to allow targeted application of drugs to increase their effectiveness [2, 3]. Synthetic hydrogels are used, for example, for biosensor devices to detect molecules or viruses [4, 5] or as delivery system for drugs and proteins [5–7].

Existing experimental research indicates that the detailed structure of hydrogels varies strongly for different hydrogels: Kirch and coworkers [8] showed that synthetic hydrogels form flexible networks with a relatively homogeneous fiber mesh while mucus hydrogels form a stiffer network with numerous large openings in the fiber network [8]. Collagen gels can include regions with highly aligned fibers, as well as regions with uncorrelated fiber orientation [9]. For biological gels, the mesh size is estimated to lie on the order of 100 nm up to 1µm [1, 10–13].

As the microscopic mechanism determining the mobility of particles in gels, a pure size-exclusion mechanism was initially assumed, where particles larger than mesh size of the polymer network are immobilized inside the gel due to steric hindrance, while particles smaller than mesh size can pass. However, a simple size filtering mechanism has been challenged in numerous recent experimental studies which showed that interaction filtering also plays an important role in regulating diffusion in biogels. Interaction filtering is a generic filtering principle introduced by Lieleg and Ribbeck [1, 14] where strong nonsteric interactions determine whether a particle can traverse gel barriers. In other words, some particles are trapped inside hydrogels due to their surface properties, and not their size. For example, according to their surface coating, some nanoparticles are immobilized in mucus, while others are highly mobile [1, 2, 14]; e.g. uncoated polystyrene nanoparticles are immobilized in mucus, but polystyrene particles coated with hydrophilic poly(ethylene glycol) (PEG) can diffuse relatively freely [1,2]. Furthermore, it was initially assumed that cervical mucus has a mesh size of about 100 nm, since small viruses like the Norwalk (38 nm) and human papilloma virus (55 nm) traverse cervical mucus almost unhindered with a diffusivity similar to their diffusivity in pure water, whereas the large herpes simplex virus with a diameter of about 180 nm is immobilized [2, 15]. However, it was eventually reported that nanoparticles with diameters of 200 and 500 nm are able to diffuse rapidly in human cervical mucus, directly contradicting the estimate of 100 nm for the mesh size of cervical mucus, which was based on the immobilization of the herpes simplex virus [2]. Naturally, size filtering also plays a role, when nonsteric particle-gel interactions are present, since transport of particles larger than the mesh size of the gel is inhibited due to steric hindrance alone, but for particles smaller than the mesh size, the passage through gel barriers is governed by interaction filtering.

For biological gels, nonsteric particle-gel interaction is often of electrostatic nature [1,14,16,17,17–22], depending on the ionic strength inside the gel and the surface charge of the particle. An interesting aspect of electrostatic interaction filtering is that electrostatic interactions can be attractive or repulsive, depending on the sign of the particle surface charge and the charge of the gel polymers. Many experiments indicate that the sign of the electrostatic interaction between particle and gel polymer heavily influences the particle diffusivity. Attractive electrostatic interactions lead to strong trapping of the particle in the gel [11, 14, 17, 21, 23], whereas repulsive electrostatic interactions appear to have a weaker effect on the particle mobility [17, 22, 23]. Thus, one might expect interaction filtering to be in general sensitive to the sign of the particle surface charge. However, some diffusion experiments with biopolymer gels report that particles of either surface charge sign are immobilized [14, 21, 24]. For example, Lieleg and coworkers [21] measured the diffusivity of liposome particles with tuneable surface charge densities in the ECM. They found that particles with a weak surface charge are mobile in the ECM, while strong particle surface charges of either sign lead to immobilization of the particles. Furthermore, they found that the mobility of immobilized charged particles can be restored when charged mobile ions which shield the electrostatic particle-gel attraction are added to the gel. To explain these experimental results, it is hypothesized that charged particles stick to oppositely charged segments on the gel polymers [14, 21]. In other words: Biopolymers carry functional groups with different biophysical properties. Thus, in biogels both positively and negatively charged interaction sites are present and consequently, charged particles of either sign are immobilized near oppositely charged interaction sites.

In addition to experimental research, there also exists a substantial body of theoretical research on the diffusion of nanoparticles in hydrogels. Already in 1958 Ogston [25] developed a formula for the diffusivity of a spherical particle performing a stochastic random walk in a network of randomly oriented cylindrical fibers. Even though his model only took into account excluded volume effects, the formula qualitatively reproduced the characteristic exponential dependency between the excluded volume fraction and the diffusivity seen in experiments. In particular computer simulations have been proven a powerful tool to test physical models for the diffusion in crowded media, a complex problem for which it can be difficult to obtain analytical solutions. In 1989, Phillips, Deen and Brady used numerical simulations with hydrodynamic interactions to predict the diffusivity of spherical particles in gels [26, 27]. The polymer network was modeled with parallel cylindrical rigid fibers, arrayed on a square lattice. They provided a heuristic fit formula for the short-time diffusion constant of the particle inside the gel as a function of the excluded volume fraction. Overviews of the mathematical models for diffusion in hydrogels can be found in references [15, 28, 29].

With increasing available computer power, dynamical simulations became widely used to model diffusion of spherical particles in hydrogels [9,30–41]. For example, in 1997 Netz and Dorfmüller employed Brownian dynamics (BD) simulations to investigate particle diffusion in various cubic arrays of fibers, modeled with linear arrays of hard spheres [32]. They found that up to intermediate excluded volume fractions, the diffusive behavior for different lattice geometries is similar to diffusion in a system of randomly placed point obstacles. For large excluded volume fractions, however, cubic structures lead to much stronger steric hindrance than randomly placed obstacles. Other theoretical research on particle diffusion in polymer networks without electrostatic particle-gel interactions [9,39] also indicates that particle diffusion depends only weakly on the spatial arrangement of the fibers for small particles. Masoud and Alexeev generated random networks of cross-linked fibers to model diffusion in hydrogels and showed that for disordered fiber networks, the diffusive behavior of the particle is practically independent of the fiber network geometry, i.e. the average length of the fibers and the cross-linking density, but only depends on the excluded volume fraction of the fiber network [33].

Flexibility of the hydrogel mesh is another aspect that was examined in theoretical studies. To include network flexibility the gel is usually modeled with spring-connected beads [35, 36, 40, 41]. It was found that for low excluded volume fractions the network flexibility has only a very limited effect on particle diffusivity inside the gel [36,41]. Only for large particles or volume fractions, network flexibility becomes important.

Theoretical studies confirm a significant hindrance effect due to electrostatic interactions on particle diffusion in gels [34, 36–38], in accordance to experimental studies, as stated above. One study examined both attractive and repulsive interactions with their model system and reported stronger particle trapping due to the electrostatic attraction than due to electrostatic repulsion between particle and gel [36]. Furthermore, only in one simulation study on particle diffusion in gels with electrostatic interactions, a quantitative comparison with experimental results was attempted, based on two data points only [34]. To fill this gap is one of the main goals of this dissertation.

Particles diffusing in hydrogels experience hydrodynamic interactions (HI). For simulations with only steric interaction in addition to HI, it was reported that HI can have a significant quantitative effect on the tracer diffusivity but do not alter the qualitative diffusive behavior [9].

In this dissertation we present different models to investigate the effect of long-range nonsteric particle-gel interactions on the diffusivity of a single spherical particle in a hydrogel. Our gel models are aimed to be simple and general in order to simulate biogels like mucus and the ECM, but also synthetic gels. The gel fibers are approximated as rigid, straight cylinders. The nonsteric particle-gel interactions are modeled with an exponentially screened interaction potential that can be either attractive or repulsive. With this basic setup for our models we aim to identify the key factors influencing interaction filtering in hydrogels.

We use the highly established BD simulation technique to model the diffusive motion of the particle. BD is a coarse-grained simulation technique with implicit solvent. The effect of the solvent particles on the motion of the diffusing particle is incorporated by a combination of a random force and a frictional term in the equation of motion of the diffusing particle. The friction and the random force are linked by the fluctuation-dissipation relation [42]. In other words: The motion of a particle inside a fluid is governed by random collisions with the solvent molecules or atoms. These collisions are incorporated into the equation of motion of the diffusing particle through the random force, which creates the diffusive Brownian motion of the particle, named after the Scottish botanist Robert Brown who published his observations of the seemingly random jittery motion of pollen grain suspended in water in 1827. At the same time, the diffusing particle has to push against solvent particles when it moves through the fluid. This effect is included in the solute equation of motion as the frictional term. Using an implicit solvent simulation technique allows for the use of much larger time steps for the integration of the particle equation of motion than would be possible with an explicit solvent. Thus, BD is a natural choice for our models, since we are interested in the long-time diffusive behavior of the particle inside the hydrogel.

1.1. Outline of this Work

In chapter 2, we present detailed simulation results for the diffusion of point particles and finite-size particles in a spatially ordered gel with electrostatic interactions. The polymer network is modeled with periodic boundary conditions as a cubic lattice of straight fibers. In collaboration with Catrin Cziemer and Dr. Won Kyu Kim, we derive an analytical scaling model to describe the diffusion of point particles in the periodic system. Furthermore, we perform quantitative comparison to published experimental data and theoretical models.

In chapter 3 we study the influence of spatial disorder of the fiber network on the diffusion of the particle. We examine the transition from a spatially ordered, cubic network to a spatially disordered, random network and identify different trapping mechanisms for spatially ordered and disordered gels with attractive and repulsive long-range particle-gel interactions. We demonstrate that for attractive particle-gel interactions, spatial disorder slows down diffusion, since the particle becomes trapped in regions of high local fiber density. For repulsive interactions, the diffusivity is minimal for intermediate spatial disorder strength, since highly disordered gels contain ample diffusion passageways of low local fiber density. We compare our simulations to published experimental data.

In chapter 4 we model diffusion in mixed anionic/cationic hydrogels. This is achieved by including random distributions of attractive and repulsive fiber segments into our model gel. Our model reproduces and confirms various experimental findings on interaction filtering in biogels. Furthermore, our simulations elucidate many details of the microscopic mechanisms for particle trapping in mixed anionic/cationic gels. We use our model to systematically examine the effect of spatial disorder and interaction disorder on the tracer diffusivity in hydrogels. In collaboration with the group of Prof. Jason E. DeRouchey we compare simulations to an experimental model system for particle diffusion in mixed anionic/cationic gels, consisting of mixtures of positively charged and negatively charged dextran gel polymers. We report that even a small fraction of attractive interaction sites inside the gel results in strongly hindered particle diffusion.

Finally, in chapter 5, we gauge the effect of hydrodynamic interactions in conjunction with long-ranged attractive or repulsive particle-gel interactions. Due to the implicit solvent, hydrodynamic interactions have to be included manually. Owing to the widespread use of BD simulations, there exists extensive literature on techniques to include HI in BD simulations [26, 43, 44]. We use the Stokesian dynamics method introduced by Banchio, Brady and Phillips [26]. We show that HI improve agreement between our simulations and published experimental data. Furthermore, we systematically examine the effect of HI in conjunction with the exponential interaction potential. Repulsive particle-gel interactions decrease the effect of hydrodynamic interactions on the particle diffusivity compared to purely steric gels. Attractive particle-gel interactions, on the other hand, strongly increase the effect of hydrodynamic interactions on the diffusivity. We find that this asymmetric behavior with respect to the sign of the interaction is due to the positioning of the particle during the simulations.

2. Nanoparticle Filtering in Charged Hydrogels: Effects of Particle Size, Charge Asymmetry and Salt Concentration

Bibliographic information: Parts of this chapter and the content of appendix A have previously been published. Reprinted with permission from Ref. [ii]. Copyright 2016 Springer Nature.

2.1. Introduction

The diffusive properties of nanoparticles and molecules in biopolymeric and synthetic hydrogels are of high interest in biological and medical sciences. Biopolymer based hydrogels play an important role in the human body, acting as protective barriers against pathogens and toxic agents. Only nanoparticles and molecules with certain properties can traverse biogel layers. Naturally, it is of great interest to determine the underlying mechanisms. Numerous experimental studies examined the filtering capability of biopolymer gels like mucus, the cytoplasm, the extracellular matrix or the biopolymer barrier in the nuclear pore complex [10, 12, 14, 16, 21, 45–49].

With the help of experimental techniques such as photobleaching, fluorescence correlation spectroscopy (FCS) and, more recently, single particle tracking, it was found that some particles (like viruses) are able to rapidly cross the hydrogel barrier, while others are immobilized [12]. In 2010, Ribbeck and coworkers introduced the concepts of size filtering and interaction filtering to explain the distinct diffusivities of miscellaneous particles [14]. Size filtering means that particles can rapidly traverse the hydrogel barrier only if they are small enough to travel between the polymer chains, i.e. smaller than the average mesh size of the hydrogel. The mesh size is determined by the polymer concentration [8, 50–52] and also to some extent by the degree of cross-linking [50–52]. Recent experimental findings suggest however, that interactions between diffusing particle and hydrogel polymers are often more influential for the particle mobility [10, 14, 16, 21, 45–49]. One contribution to these interactions seems to be of electrostatic nature, since the particle mobility is highly dependent on the particle surface charge [10, 14, 16, 21, 45–47] and the salt concentration [14, 21]. In fact, in one study 100 nm sized, coated polystyrene beads were found to be much more strongly immobilized inside human cervicovaginal mucus than 200 and 500 nm polystyrene beads with the same surface chemistry [10]. This directly contradicts the idea that the finite mesh size of cross-linked hydrogels is solely responsible for hindered diffusion. Thus, the filtering capability of a hydrogel is in many cases dominated by nonsteric interactions between diffusing particle and hydrogel polymers.

There are a couple of simulation studies on tracer diffusion in charged and uncharged porous media and hydrogels [30, 32, 34–38, 40, 53]. Many papers focused on the effects of excluded volume, network flexibility and degree of cross linking as well as on anomalous diffusion. Electrostatic interactions between particles and the hydrogel have been included by Miyata and coworkers [37, 38] as well as by Zhou and Chen [36]. In these works electrostatic interactions were found to strongly affect particle mobility but, in contrast to our work, no comparison with experimental results was attempted. Also, in the papers by Miyata and coworkers, only the case of oppositely charged tracer particles and hydrogel was investigated. Their model predicts that attractive electrostatic interactions slow down diffusion, especially at small ion concentrations, and they derive an analytic scaling expression for the relative diffusivity of the tracer particle.

Stylianopoulos and coworkers [34] modeled the extracellular matrix as a spatially periodic square array of straight fibers. They included hydrodynamic interactions, as well as repulsive electrostatic interactions between a spherical tracer particle and the polymer chains and showed that repulsive electrostatic interactions in combination with hydrodynamic effects can substantially slow down the mobility of nanoparticles, in qualitative agreement with experimental measurements for the diffusivity of nanoparticles in collagen gels [34]. In another recent work, Stylianopoulos and coworkers modeled an uncharged polymer gel of straight fibers with different degrees of alignment [9]. They found that the diffusive behavior of tracer particles is qualitatively very similar for different geometries of the polymer network.

Our model is designed to simulate diffusion of particles that are subject to steric and nonsteric interactions with hydrogel polymers. It consists of a single spherical tracer particle, diffusing in a cubic lattice comprised of straight, rigid, infinitely long rods. The nonsteric interaction potential is of a generic exponential form with varying strength and range that can be either repulsive or attractive. This design is chosen to investigate basic mechanisms governing the diffusion of generic particles inside different kinds of cross-linked hydrogels. Brownian dynamics (BD) simulations are employed to investigate the long-time particle diffusion for varying screened electrostatic interaction range and strength as well as mesh size and particle size. We neglect hydrodynamic interactions, which reflects that hydrodynamics is screened in highly concentrated polymer solutions.

We find that our model reproduces several experimentally observed trends. This includes, for example, a decreased diffusivity for particles with larger surface charge and a sensitivity for the sign of the surface charge of the diffusing particle. Furthermore, our model reproduces the peculiar particle size dependency of the diffusivity of nanoparticles inside human cervicovaginal mucus, where it occurs that smaller particles are more strongly hindered than larger particles [10]. Interestingly, using different model parameters, the opposite behavior can also be reproduced, i.e. smaller particles diffusing faster than larger ones.

In our previous study [54] we experimentally measured the diffusivity of charged nanoparticles in charged hydrogels under varying ion concentrations. We employed FCS and used Alexa488 molecules as fluorescent probes which carry a negative net charge. The diffusion in both positive and negative dextran hydrogels was tested. We found attractive electrostatic interactions to hinder nanoparticle diffusion much more effectively than re-

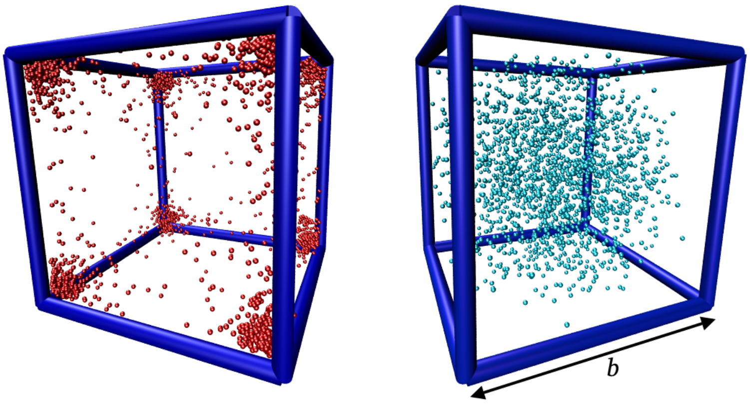

Figure 2.1. Schematic sketch of the simulation cell with 2000 particle-position snap shots. The red dots indicate snap shots in an attractive interaction potential with $U_0 = -5k_BT$ (*left*), the light blue dots indicate snap shots in a repulsive interaction potential with $U_0 = 5k_BT$ (*right*). The steric diameter is $s = 0.1b$ and the interaction range is $k = 0.2b$ in terms of the cubic lattice constant b.

pulsive electrostatic interactions which was qualitatively reproduced by our simulation model data. The present work goes beyond our previously published paper in a number of respects. We include a detailed discussion of the influence of the particle size on the diffusion and compare with experimental data on diffusion in mucus for differently sized nanoparticles. We also include an analysis of the polymer concentration dependency of the particle diffusion in our model system. In addition, we present a simple analytic approximation based on diffusion in a free energy landscape that captures our simulation results very well. In order to present a complete analysis of our model, we include a detailed quantitative comparison with our previously published experimental data on Alexa488 diffusion in dextran hydrogels [54].

2.2. Methods

2.2.1. Brownian dynamics simulation

The random Brownian motion of a particle in a solvent is described by the overdamped Langevin equation

$$\dot{r}_i(t) = -\mu_0\,\partial_i U(\vec{r}(t)) + \zeta_i(t)\;, \quad (i = x, y, z)\;, \tag{2.1}$$

where $\dot{r}_i$ is the time derivative of the particle position and ∂_i the spatial derivative. U is the potential and μ_0 the bulk sphere mobility. The random velocity ζ_i is a stochastic variable, modeled with Gaussian white noise

$$\langle \zeta_i(t) \rangle = 0\;, \tag{2.2}$$

$$\langle \zeta_i(t)\,\zeta_j(t') \rangle = 2\mu_0 k_B T\,\delta(t-t')\,\delta_{ij}\;. \tag{2.3}$$

δ_{ij} is the Kronecker delta, T is the temperature and the indices i, j denote Cartesian coordinates. Since we are interested in the long-time diffusivity of the particle, the particle mass is neglected in the equation of motion (2.1). By discretizing the Langevin equation one obtains an iterable expression for the particle position, where the particle displacement evaluated at each timestep is

$$\Delta\tilde{r}_i \;=\; -\,\tilde{\mu}\,\tilde{\partial}_i\tilde{U} \,+\, \sqrt{2\tilde{\mu}}\,\tilde{\zeta}_i\;. \tag{2.4}$$

The tilde denotes rescaled variables. All lengths are scaled by the box size b indicated in fig. 2.1, and energies by the thermal energy k_BT. $\tilde{\zeta}$ is a Gaussian distributed random number with zero mean and variance $\langle\tilde{\zeta}_i\,\tilde{\zeta}_j\rangle = \delta_{ij}$. The rescaled timestep $\tilde{\mu}$ is defined as

$$\tilde{\mu} = \frac{\Delta t\,\mu_0 k_B T}{b^2}\;, \tag{2.5}$$

which is chosen small enough, such that the resulting data is independent of $\tilde{\mu}$. For the simulations in this chapter a timestep of $\tilde{\mu} = 10^{-6}$ is used, which is well within the continuum limit.

2.2.2. Gel model

In our cubic lattice model the lattice edges represent the polymer chains and the box size of a single cell b corresponds to the average mesh size of the hydrogel (compare fig. 2.1). The symmetry of the system allows for the usage of periodic boundary conditions. In eq. (2.1) the total potential $U(\vec{r})$ that acts on the diffusing particle is

$$U(\vec{r}) = U^{\mathrm{s}}(\vec{r}) + U^{\mathrm{i}}(\vec{r})\;. \tag{2.6}$$

where the superscripts s and i denote steric and nonsteric interactions, respectively.

$$U^{\mathrm{s}}(\vec{r}) = \sum_{n=1}^{N}\begin{cases}4\epsilon\left[\left(\frac{s}{2\rho_n}\right)^{12} - \left(\frac{s}{2\rho_n}\right)^{6} + \frac{1}{4}\right], & \rho_n \leq 2^{-5/6}s\\ 0\,, & \rho_n > 2^{-5/6}s\,,\end{cases} \tag{2.7}$$

where the energy depth is $\epsilon = 1\,k_BT$, ρ_n is the distance between the particle and the nth fiber and $s = a + p$ is the steric diameter, i.e. the sum of the diameters of the fibers a and the particle p. The potential is shifted such that it is positive and continuously reaches zero at the cutoff distance $\rho_n = 2^{-5/6}\,s$, at which the LJ potential has its minimum.

Nonsteric interactions between the particle and the rods are included in the form of an exponential interaction potential

$$U^{\mathrm{i}}(\vec{r}) = \sum_{n=1}^{N} U_0 \exp\left(-\frac{\rho_n}{k}\right)\;, \tag{2.8}$$

where k is the interaction range and U_0 the strength of the potential. For negative U_0 the potential is attractive and for positive U_0 it is repulsive. The individual rods are static and do not interact with each other. For electrostatic interactions, the interaction range k corresponds to the Debye screening length determined by [55]

$$k^2 = \frac{1}{4\pi l_B I}\,, \tag{2.9}$$

where $l_B = e^2/4\pi\epsilon k_B T$ is the Bjerrum length, e the elementary charge and ϵ the permittivity. $I = \frac{1}{2}\sum_j n_j\, z_j^2$ is the ionic strength and z_j the valence of salt ion j and n_j its bulk number density. The bulk number density n is related to the molar ion concentration through $C_{\text{Ion}} = n/N_A$, where N_A is the Avogadro constant. For a molar ion concentration $C_{\text{Ion}} = 100\text{mM}$ the Debye length is $k \approx 1\,\text{nm}$.

The strength of the potential U_0, scaled with $k_B T$, can be interpreted as the product of the particle charge and the linear polymer charge density. In the Debye-Hückel approximation, the surface potential of a charged cylinder in units of $k_B T$ is [56]

$$U_{\text{cyl}}/k_B T = 2 l_B \tau K_0\big(p/2k\big) I_0\big(p/2k\big)\,, \tag{2.10}$$

where τ is the line charge density, s the diameter of the cylinder and K_0 and I_0 the modified Bessel functions. In our model, the effective cylinder diameter s incorporates the polymer chain diameter as well as the particle diameter. The potential strength U_0 defined in eq. (2.8) thus follows as

$$U_0 = z_p\, U_{\text{cyl}}\, \exp(p/2k)\ . \tag{2.11}$$

where z_p is the particle charge number.

For computational efficiency the summation in eq. (2.8) is limited to a finite number of N nearest neighbor rods. A *first order* summation includes $N = 12$ rods at the edges of the cubic simulation box. A *second order* summation includes $N = 48$ rods at the edges of the adjacent unit cells. For the investigated values of the interaction range k going from $k = 0.01b$ to $k = 0.5b$ it is sufficient to include $N = 12$ rods for ranges $k < 0.2b$ and $N = 48$ rods for ranges $k \geq 0.2b$, since the contributions of more distant rods are negligible.

In the long-time limit the mean-squared displacement (MSD) of the particle becomes proportional to the diffusion constant D [36, 37, 57]

$$\lim_{t\to\infty} \langle \Delta r^2(t)\rangle \;=\; 6\, D\, t\,, \tag{2.12}$$

with $\Delta r^2(t) = (\vec{r}(t) - \vec{r}(0))^2$. Hence, the diffusivity D of the particle is obtained by linearly fitting the MSD in the long-time limit. To obtain reliable data, the MSD is calculated over 10^4 simulation runs, with each run consisting of at least 10^6 steps. The diffusion constant for a freely diffusing particle without interactions is $D_0 = \mu_0 k_B T$. Most of the results are presented in terms of the relative diffusivity D/D_0 to show how much the particle diffusion is inhibited inside the hydrogel. The fluctuations of the relative diffusivities resulting from the simulation output is below $\delta(D/D_0) = \pm 5\%$ for values of $D/D_0 \geq 0.001$.

2.2.3. Analytical model

The analytical calculations were done in collaboration with Catrin Cziemer and Dr. Won Kyu Kim.

We now derive a simple analytic theory for the effective diffusion of a point particle in the three-dimensional potential landscape defined above. The laterally averaged probability density, which depends on only one spatial coordinate x, is obtained by integrating over the two other spatial coordinates y and z. This yields for the one-dimensional effective potential

$$U_{\text{eff}}(x) = -k_BT \ln\left(\frac{1}{b^2}\int_0^b\int_0^b \mathrm{d}y\mathrm{d}z\mathrm{e}^{-U(x,y,z)/k_BT}\right), \tag{2.13}$$

which is the projection of the free energy landscape onto the spatial coordinate x. The relative diffusivity can now be calculated according to [58]

$$\frac{D}{D_0} \simeq b^2\left[\int_0^b \mathrm{d}x\mathrm{e}^{U_{\text{eff}}(x)/k_BT}\int_0^b \mathrm{d}x\mathrm{e}^{-U_{\text{eff}}(x)/k_BT}\right]^{-1}. \tag{2.14}$$

Due to the symmetry of our hydrogel model, U_{eff} is periodic with the periodicity $L = b$. The results of solving eq. (2.14) are presented in section 2.3.1. For numerical integration nearest neighbor interactions are taken into account, hence a second order summation of the potential in eq. (2.8) is performed, as described above.

To obtain further insight, we determine an analytic approximation to eq. (2.14). Performing a saddle-point approximation on eq. (2.13) we obtain

$$\begin{aligned} U_+(x) = {} & U^{\mathrm{i}}(x, y_0, z_0) + \frac{k_BT}{2}\log[\partial_y^2 U^{\mathrm{i}}(x,y,z)/k_BT]_{y_0,z_0} \\ & + \frac{k_BT}{2}\log[\partial_z^2 U^{\mathrm{i}}(x,y,z)/k_BT]_{y_0,z_0}, \end{aligned} \tag{2.15}$$

for a repulsive interaction potential, $U_0 > 0$, and we approximate

$$U_-(x) = U^{\mathrm{i}}(x,0,0), \tag{2.16}$$

for the case of an attractive interaction potential, $U_0 < 0$. Here, $y_0 = z_0 = 0.5b$. Inserting eqs. (2.15) and (2.16) into eq. (2.14) and performing another saddle-point approximation leads to the analytical expressions

$$\frac{D^+}{D_0} \approx b^2\frac{\sqrt{-U_+''(x_1^+)\,U_+''(x_2^+)}}{2\pi k_BT}\mathrm{e}^{\left(U_+(x_1^+)-U_+(x_2^+)\right)/k_BT}, \tag{2.17}$$

for a repulsive interaction potential, $U_0 > 0$, and

$$\frac{D^-}{D_0} \approx b^2\sqrt{\frac{-U_-''(x_2^-)}{2\pi k_BT}\,\frac{U_-'(x_1^-)}{2k_BT}}\,\mathrm{e}^{\left(U_-(x_1^-)-U_-(x_2^-)\right)/k_BT}, \tag{2.18}$$

for the case of an attractive interaction potential, $U_0 < 0$. The positions $x_2^- = 0.5b$ and $x_1^- = 0$ denote the locations of the maximum and the minimum of eq. (2.13) for $U_0 < 0$. For $U_0 > 0$, $x_1^+ = 0.5b$ is the location of the minimum and $x_2^+ = 0$ the location of the maximum. The prime represents a differentiation in x. The saddle point approximations become valid for large potential strengths. A more detailed derivation is presented in the appendix, as well as the explicit expressions for the derivatives of U^{i}, U_+ and U_-.

From eqs. (2.17) and (2.18) the asymptotic behavior of the relative diffusivities for large positive and negative interaction strengths U_0 follows as

$$\lim_{U_0 \to \infty} \frac{D^+}{D_0} \propto U_0 \, \mathrm{e}^{c_+ U_0 / k_B T} \,, \tag{2.19}$$

$$\lim_{U_0 \to -\infty} \frac{D^-}{D_0} \propto (-U_0)^{3/2} \, \mathrm{e}^{c_- U_0 / k_B T} \,. \tag{2.20}$$

The scaling in U_0 follows from the fact that U and its derivatives linearly depend on U_0. The k dependent parameters c_+ and c_- are determined by sums and given explicitly in the appendix.

The exponential dependency of the diffusivity D on the potential strength U_0 in eqs. (2.19) and (2.20) is in agreement with the standard Kramers law [59] and agrees also with explicit results for the diffusion of charged tracer particles in oppositely charged polymer networks [38].

2.3. Results

We first consider point particles, i.e. the steric potential U^{s} in eq. (2.7) is set to zero. Figure 2.2a shows exemplary MSD data for different potential strengths U_0. While the $U_0 = -1$ and $5 k_B T$ data follow the free diffusion curve indicated as dotted line, three regimes are clearly visible for $U_0 = -5 k_B T$. In the short-time regime, the tracer particle moves on average like a freely diffusing particle in water. In the intermediate regime, the tracer particle MSD is reduced due to the interaction potential and it exhibits a t^α power law with $\alpha < 1$. This anomalous diffusion behavior is referred to as sub-diffusion and is a known characteristic of diffusion in crowded environments [35, 60]. To examine the anomalous diffusion behavior more closely, fig. 2.2b shows the local diffusion exponent α as a function of time, defined as [61]

$$\alpha = \frac{\mathrm{d} \log \langle \Delta r^2(t) \rangle}{\mathrm{d} \log t} \,. \tag{2.21}$$

We estimate the local exponent by linearly fitting the MSD data points at times t_i in a finite range defined by $|\log_{10}(t_i/t)| < 0.15$. One can see a sub-diffusive region for $U_0 = -5 k_B T$ with a broad minimum of $\alpha \approx 0.37$. Subsequently, α increases until it reaches a value of 1, i.e. normal diffusion, for long times. For $U_0 = -1$ and $5 k_B T$, the diffusion remains in the normal diffusion regime. In the following, we only evaluate the long-term relative diffusivity D/D_0.

In fig. 2.2c, which shows the same MSD data divided by time, one can see that these ratios approach a constant value in the long-time limit, which is reached after a displacement

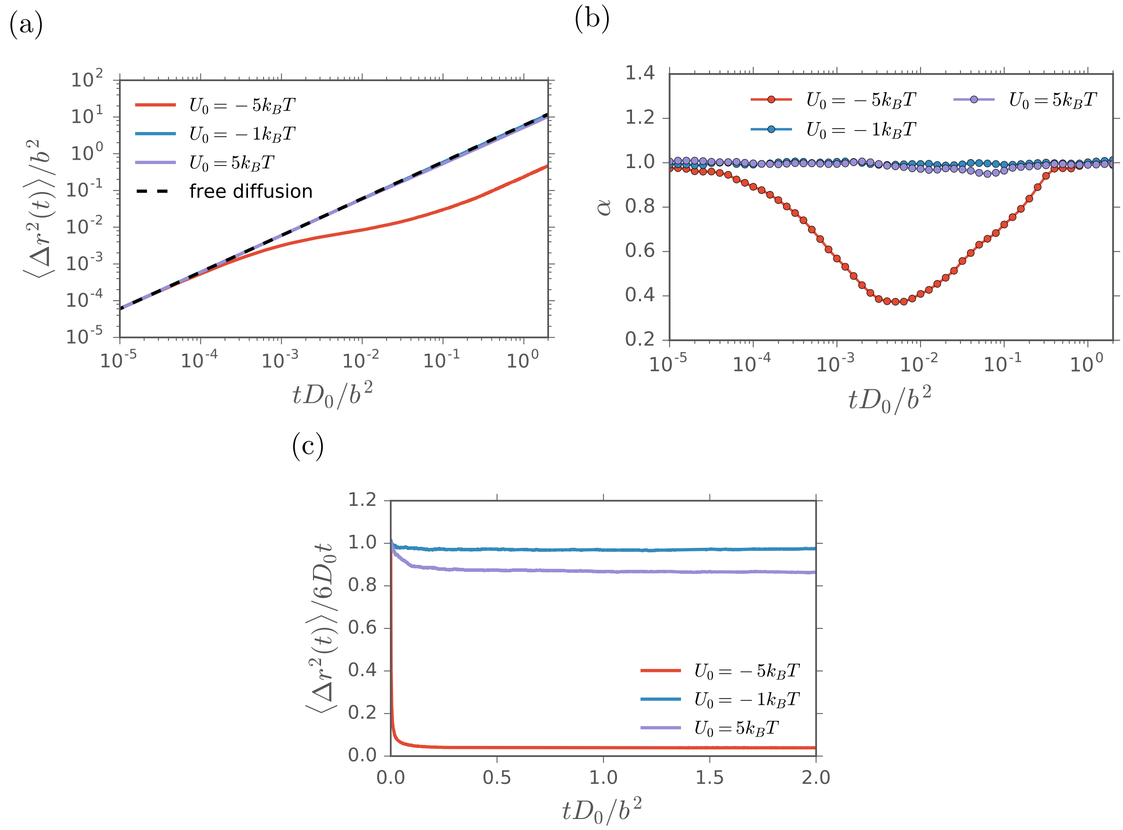

Figure 2.2. Typical MSD simulation data for different potential strengths U_0 for point particles at constant interaction range $k = 0.1b$. Plot (a) shows the MSD, $\langle \Delta r^2(t) \rangle$, as a function of time in a double logarithmic plot. (b) shows the scaling exponent α defined in eq. (2.21) as a function of time. (c) shows $\langle \Delta r^2(t) \rangle / t$ in a semi-log plot and demonstrates the approach to a constant value in the long-time limit. This long-time value corresponds to the relative diffusivity D/D_0 of the particle.

of roughly $\Delta r^2 > k^2$ for attractive potentials and $\Delta r^2 > b^2$ for repulsive potentials. This reflects the distance the particle has to diffuse in order to escape the potential minimum.

An interesting aspect of our model can already be observed here, namely, that attractive and repulsive potentials of equal absolute potential strength $U_0 = -5$ and $+5k_BT$ lead to different diffusivities. This will be more closely examined in the following section.

2.3.1. Point particles

For the diffusion of point particles, characterized by a steric diameter $s = 0$, the only relevant parameters are the potential strength U_0/k_BT and the interaction range k/b. In fig. 2.3, the dependency of the relative diffusion coefficients D/D_0 on the potential strength U_0 is presented for different k, indicated by differently colored curves. The curves are shown over an interval of $-10k_BT \leq U_0 \leq 20k_BT$. The simulation data, shown as symbols, exhibits free diffusion for zero potential strength U_0. D/D_0 decreases for both

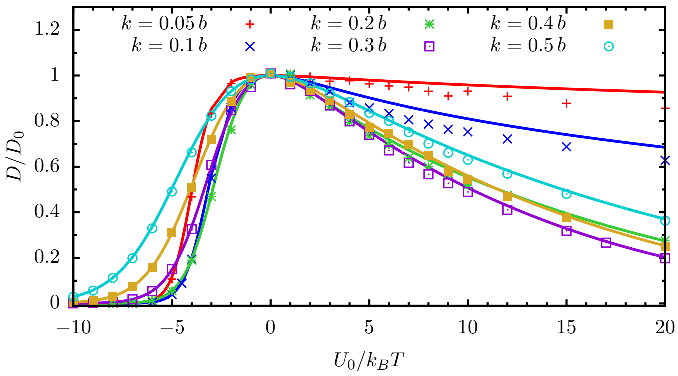

Figure 2.3. The relative diffusivity of point particles D/D_0 as a function of the potential strength U_0 at different ranges k. The points are BD simulation data, the lines obtained by numerical integration of eqs. (2.13) and (2.14).

increasing attractive, $U_0 < 0$, and increasing repulsive, $U_0 > 0$, potential strengths. In the case of strong attractive interactions at $U_0 = -10k_BT$ the simulations exhibit very small relative diffusivities near zero. This is due to a strong and localized potential minimum near the intersections of the rods, where the potentials of three perpendicular rods add up. If the particle diffuses into such a minimum it will *stick* there. In the case of repulsive interactions, $U_0 > 0$, the decrease in diffusivity is much less pronounced. Here, an *exclusion* effect occurs, where the particles tend to be "pushed" by the repulsive interactions into the potential minimum in the center of the box. This minimum can be seen in fig. 2.4a, where the effective potential $U_{\text{eff}}(x)$ according to eq. (2.13) for a repulsive potential, the analytical approximation $U_+(x)$ according to eq. (2.15) and the potential along the central axis of the simulation box $U^{\text{i}}(x, 0.5b, 0.5b)$ are compared. Figure 2.4b shows $U_{\text{eff}}(x)$ for an attractive potential and $U^{\text{i}}(x, 0, 0)$, the interaction potential along the edge of the simulation box. Comparing figs. 2.4a and 2.4b one can see that the minimum in the attractive case in fig. 2.4b is much more pronounced than in the repulsive case in fig. 2.4a, which is why exclusion (for $U_0 > 0$) produces a weaker effect on diffusion than sticking (for $U_0 < 0$). The simulation snap shots in fig. 2.1 visually demonstrate sticking (left figure) and exclusion (right figure).

We also observe in fig. 2.3 that, in the repulsive regime, $U_0 > 0$, the diffusivity is most affected when the range is $k = 0.3b$. At larger ranges the electrostatic potential difference between the center and the faces of the box decreases, i.e. the potential barrier the particle has to overcome decreases and thus the particle diffuses more rapidly. At smaller ranges k the particle spends more time outside the range of the individual polymer chain interaction potentials and is thus less strongly immobilized. This range dependency is studied more closely in fig. 2.5, which shows D/D_0 as a function of the interaction range k at constant potential strengths U_0. Except for a strong attractive potential at $U_0 = -10k_BT$ or a weak one at $-1k_BT$, a clear minimum is always visible, which lies at an interaction range of around $k \approx 0.3b$ for repulsive potentials and around $k \approx 0.15b$ for an attractive potential of strength of $U_0 = -5k_BT$. We again see that the diffusivity is smaller for attractive potentials compared to repulsive potentials of similar strength.

(a)

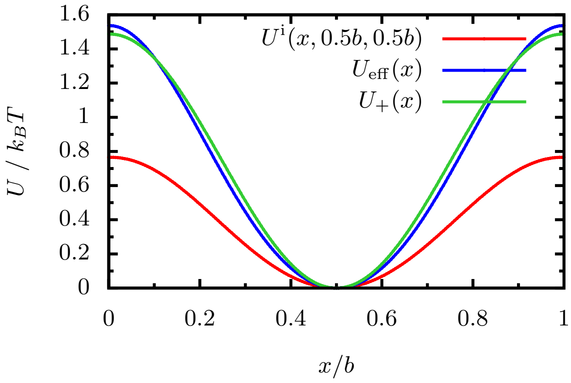

(b)

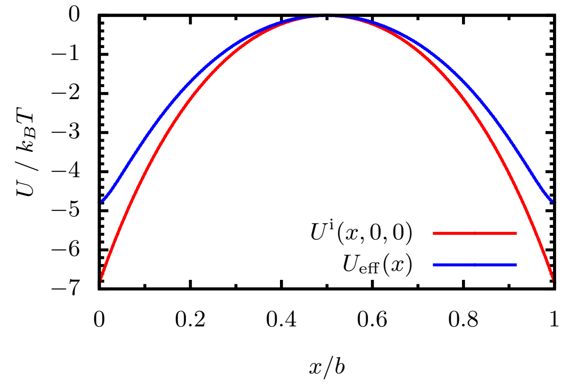

Figure 2.4. Plot (a) shows the interaction potential $U^i(x, 0.5b, 0.5b)$ according to eq. (2.8) along the central axis of the simulation box for the repulsive case $U_0 = 5k_BT$, compared with the numerically determined effective potential $U_{\mathrm{eff}}(x)$ according to eq. (2.13) and the analytical approximation $U_+(x)$ presented in eq. (2.15). Plot (b) shows $U^i(x, 0, 0)$ along the edge, compared with $U_{\mathrm{eff}}(x)$ for the attractive case $U_0 = -5k_BT$. The interaction range is $k = 0.3b$. Note that the potential curves are shifted to overlap at $x = 0.5b$, for better comparison.

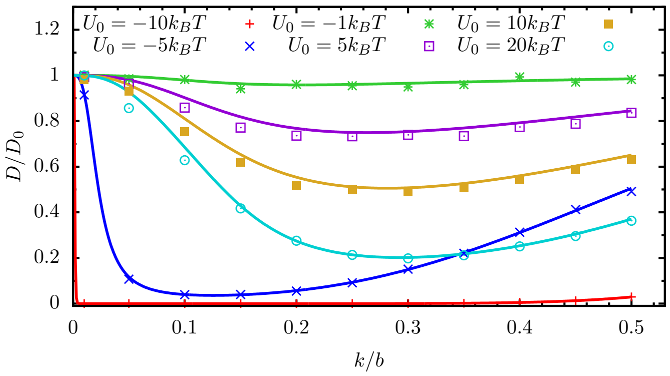

Figure 2.5. The relative diffusivity D/D_0 as a function of the interaction range k for point particles. The different colors of the data indicate simulations at different potentials strengths U_0. The points are BD simulation data, the lines are obtained by numerical integration of eqs. (2.13) and (2.14).

In both figs. 2.3 and 2.5, the data obtained by 3D numerical integration of eqs. (2.13) and (2.14), presented as colored lines, agrees well with the results of the BD simulation, indicated by similarly colored symbols. It follows that the simple analytic theory captures the diffusive behavior and in particular the symmetry breaking between attractive and repulsive potentials very well.

In fig. 2.6 we present the results of our analytical approximations eqs. (2.17) and (2.18) in comparison to the numerical integration of eqs. (2.13) and (2.14) and simulation data for an intermediate interaction range of $k = 0.3b$. The data is presented in a lin-log plot to reveal the asymptotic scaling behavior. The simulation data (red crosses) and the analytic approximations eqs. (2.17) and (2.18) (denoted by blue lines) converge at large negative and positive U_0, as expected, since the saddle point approximation, by construction, captures the effects of large barriers. Furthermore, both the analytic approximation and the simulation data exhibit the same scaling behavior as the asymptotic expansion for large $|U_0|$, eqs. (2.19) and (2.20), which is indicated in fig. 2.6 by green lines. Hence, the repulsive and attractive cases both exhibit asymptotic exponential scaling in U_0, but with different power law prefactors.

2.3.2. Finite-size particles

Introducing steric effects characterized by a non-zero steric diameter $s > 0$ has a strong impact on the diffusive behavior. This can be observed in fig. 2.7 where the interaction strength is set to $U_0 = 0$ and only steric interactions as described by eq. (2.7) are included. The relative diffusivity D/D_0 approaches unity as the steric diameter s goes to zero. For s approaching the width of the simulation box b, the relative diffusivity goes to zero, since the particle eventually cannot cross between the rods anymore, due to steric hindrance.

The effect of combining steric and nonsteric interaction is presented in fig. 2.8. The diffusivity is highly dependent on the steric diameter s. For attractive potentials, $U_0 < 0$, larger particles experience weaker sticking than smaller particles, since larger particles cannot get as close to the potential minima. Figure 2.8a reveals that at a small interaction

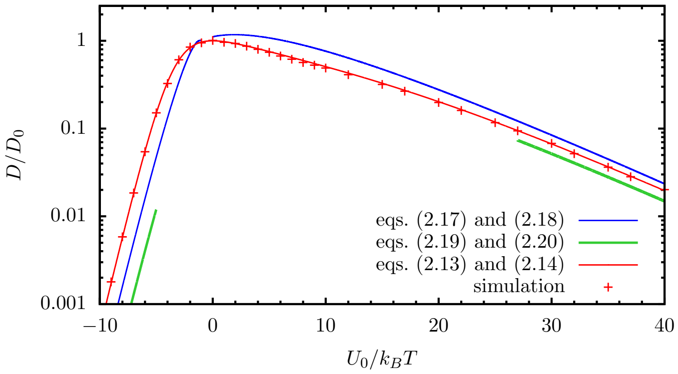

Figure 2.6. Comparison of the numerical and analytical approximations for D/D_0 and the simulation results (*red crosses*) for an interaction range $k = 0.3b$. The analytical approximations presented in eqs. (2.17) and (2.18) are shown as *blue lines*, the numerical integration of eqs. (2.13) and (2.14), as a *red line*. The asymptotics for large $|U_0|$, presented in eqs. (2.19) and (2.20), are shown as *green lines*.

range $k = 0.05b$, particles with larger effective diameter $s > 0.2b$ are not affected by changes in the potential strength U_0 and only small particles with $s < 0.1b$ experience strong sticking for sufficiently negative U_0. The same trend is seen also for the larger interaction ranges $k = 0.1$ and $0.2b$ in figs. 2.8b and 2.8c. This is noteworthy, since it implies that an attractive interaction potential actually immobilizes smaller particles more efficiently than larger particles.

In contrast, in the repulsive regime, $U_0 > 0$, size effects vanish towards larger potential strengths U_0 for particles with an effective diameter between $0.1b$ and $0.5b$. This occurs because for $U_0 \gg 0$ the particle tends to be near the center of the box outside the range of the LJ potential in eq. (2.7), as can be observed in fig. 2.1 (right figure).

Figure 2.8c shows that particles with a large effective diameter $s = 0.9b$ experience an increase in diffusivity as the potential becomes more attractive. This occurs, since the attractive potential between polymer chains and particle counteracts the repulsive steric interaction, i.e. the truncated LJ potential, leading to a lowering of the total potential barrier which the particle has to cross between adjacent lattice boxes. This effect of enhanced diffusion through attractive interaction has been observed in other models before, and was rationalized by a reduction of roughness of the coarse-grained excess chemical potential landscape [62].

To examine steric effects more closely we show the relative diffusivity D/D_0 as a function of the steric diameter s in fig. 2.9 at different potential strengths U_0. One can see that, in the strongly repulsive cases $U_0 = 10, 20k_BT$, as the steric diameter s increases, the relative diffusivity decreases monotonously and approaches a value close to zero for $s = b$. For small $s < 0.5b$ steric effects almost completely vanish and the relative diffusivity remains almost constant. For negative $U_0 = -3, -10, -20k_BT$ on the other hand, we observe a maximum at an intermediate steric diameter. The maximum occurs, since as the steric diameter s increases, sticking becomes weaker but beyond an intermediate steric diameter, the hindrance effect due to steric interaction becomes dominant. This interesting difference

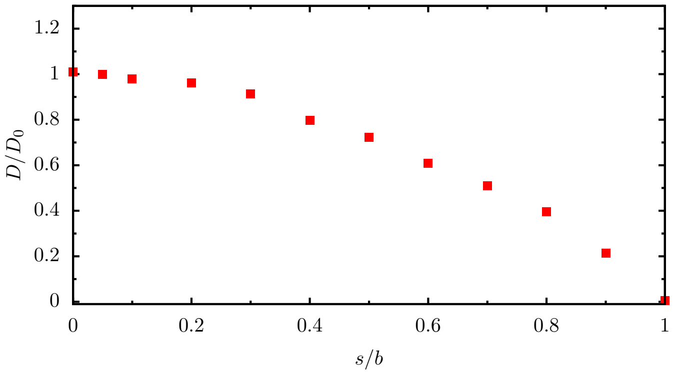

Figure 2.7. The relative diffusivity D/D_0 as a function of the steric diameter s relative to the box size b. This figure shows the purely steric hindrance included via the truncated LJ potential, eq. (2.7), with U_0 set to zero.

between attractive and repulsive interaction potentials will be further discussed in the next section, in comparison with experimental findings.

2.4. Comparison with Experiments

We consider three different experimental situations, namely, changes in polymer concentration, in the size of the diffusing particle and in the salt concentration.

2.4.1. Polymer concentration effects

For hydrogels, an increase in polymer concentration leads to a smaller mesh size [52], which corresponds to a larger relative steric diameter s/b. Increasing s/b at $U_0 = 0$ leads to a decreasing diffusivity, as can be seen in fig. 2.7, which is in qualitative accordance with experimental results [14, 28, 30, 54, 63]. To enable a quantitative comparison with experimental data we relate the polymer mass concentration C_{poly} of a hydrogel to the box size b. For this, we assume that the polymer chains form a cubic lattice, similar to our simulation model. This approximation is reasonable for hydrogels that form tetrafunctional cross-links [50] and is also often used for non cross-linked hydrogels [32]. It leads to the following equations

$$\begin{aligned} n_d &= \left(\frac{3b}{a} - 2\right)\frac{1}{b^3} = \frac{C_{\text{poly}}}{m_a}\,, \\ \rightarrow\; C_{\text{poly}} &= \frac{(3b-2a)\,m_a}{ab^3}\,, \end{aligned} \tag{2.22}$$

where a is the diameter of the hydrogel monomers, m_a the monomer mass and n_d the monomer number density. For comparison between simulation and experimental data the steric diameter s, is equated to the sum of the experimental tracer particle diameter p plus the monomer diameter a. To produce explicit results, we use dextran as an example. Dextran has a monomer width of $\sim 0.4\,\text{nm}$ and a monomer weight of $m_a \approx 162\,\text{Da}$ [30].

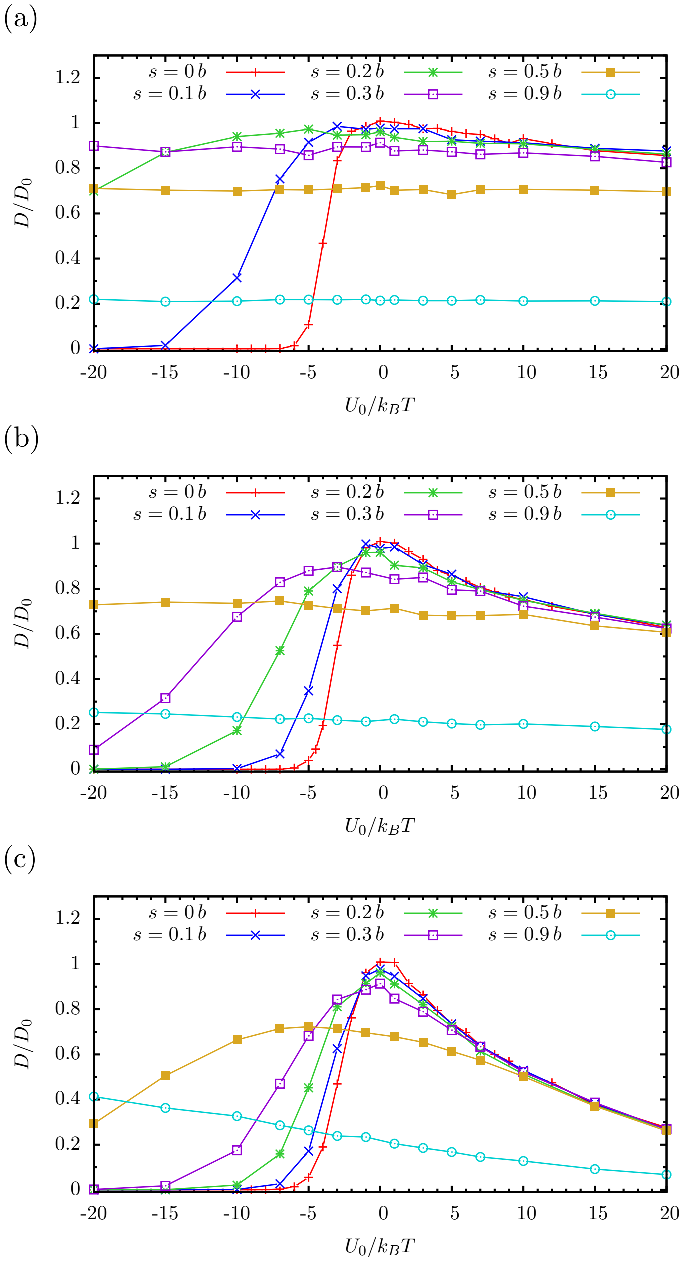

Figure 2.8. Comparison of simulation results for D/D_0 as a function of U_0 including steric interactions. The simulation data is shown for different steric diameters s and for different interaction ranges of (a) $k = 0.05b$, (b) $k = 0.1b$ and (c) $k = 0.2b$. The lines are included to guide the eye.

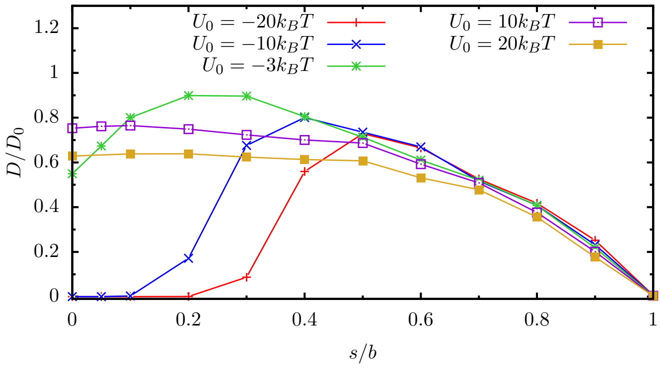

Figure 2.9. The steric diameter s dependency of the relative diffusivity D/D_0 is presented for attractive interaction potentials, $U_0 = -20, -10, -3k_BT$, as well as repulsive interaction potentials $U_0 = 20, 10k_BT$. For all data presented here, the interaction range is $k = 0.1b$. The lines are included to guide the eye.

The nanoparticle diameter is set to $p \approx 1.5\,\text{nm}$, which corresponds to the diameter of an Alexa488 molecule [54]. Furthermore, we add the width of a water hydration layer of $w \approx 0.4$ nm [54, 64]. We thus have $s = a + p + w = 2.3\,\text{nm}$. Accordingly, our simulation data is presented as a function of diffusivity over polymer concentration in fig. 2.10. We find a linear relation between polymer concentration and diffusivity.

A number of different analytical models have been developed for particle diffusion in polymer networks [25, 28–30, 65]. For comparison to our data in fig. 2.10, we include predictions by analytical models developed by Johansson et al. [30], Ogston et al. [25] and Tsai and Strieder [65] for nanoparticle diffusion in gels with rigid polymer chains without hydrodynamic interactions. The three different models were derived under the common basis, that the particle diffuses in a random network of straight fibers. We find rough agreement between our simulations and the analytical models for small polymer concentrations. For large C_{poly} the diffusivity in our model system becomes zero and diverges from the analytical model predictions. It has been noted before, that the analytical models by Johansson et al. and Tsai and Strieder show best agreement to simulations at low fiber volume fractions, while the model by Ogston has been found to only qualitatively agree with experiments [28]. Furthermore, our model consists of an ordered array of straight fibers. Hence, in the case where the steric diameter s is of the order of the polymer chain spacing b the particles are entirely immobilized inside the polymer network. The difference to a random array of straight polymer chains, where diffusing particles typically can find openings larger than the mesh size b, presumably plays an important role at higher polymer concentration.

Experiments on nanoparticle diffusion in synthetic hydrogels typically report a stretched exponential dependency on the polymer concentration [28, 54, 63, 66, 67] that has been shown to be caused by hydrodynamic effects [28], which are neither included in our simulation model, nor in the analytical models presented in fig. 2.10.

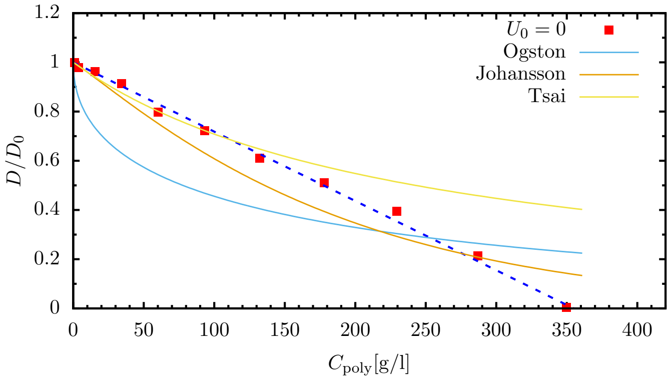

Figure 2.10. The relative diffusivity D/D_0 as a function of the polymer mass concentration C_{poly} from our simulations for vanishing electrostatic interactions ($U_0 = 0$), using the conversion eq. (2.22). The exemplary polymer parameters correspond to an Alexa488 particle diffusing in a dextran hydrogel (see text for details). The dashed line indicates the linear decrease of D/D_0. The solid lines represent predictions by different analytic models.

2.4.2. Particle size effects

A number of experimental studies have examined the diffusion of nanoparticles with different surface chemistries in different kinds of mucus [10, 16, 47, 49]. It was reported that in some cases the smallest particles with a diameter of 100 nm are most effectively immobilized, while in other cases the biggest particles with a diameter of $p > 500$ nm are more strongly immobilized. Figure 2.9 suggests that indeed both situations are encountered in our model. In an attractive interaction potential, smaller particles move slower than particles of intermediate size. In a repulsive interaction potential on the other hand, the diffusivity monotonously decreases for increasing particle diameter.

A quantitative comparison with the aforementioned experimental results is difficult, since the experimental studies do not include information about the salt concentration inside the mucus which would be needed to compute the interaction range k. Furthermore, estimates of the average mesh size of mucus range from about 0.1 µm [12] to 0.8 µm [10, 49] and the distribution of pore sizes is presumably very broad, such that larger particles can move in regions with larger pores and still be quite mobile inside the mucus, even if they are larger than the average mesh size [16, 48, 49].

Example 1 - Larger particles diffuse faster: Lai and coworkers have studied the diffusivity of PEG coated polystyrene particles with diameters 100, 200 and 500 nm in undiluted cervicovaginal mucus [10]. They report large 500 nm particles diffusing at a greater relative diffusivity D/D_0 than smaller 200 and 100 nm particles. For our comparison we assume that the interaction range is $k = 0.1b$, i.e. small compared to the mesh size b. Figure 2.11a shows how our simulation results can be matched with the experimental data by assuming attractive interactions with a strength $U_0 = -10$ or $-20k_BT$ for particles that have similar size ratios as in the experiment, namely, $p/b = 0.1, 0.2, 0.5$ and $p/b = 0.2, 0.4, 0.9$, respectively. Note, that we are neglecting the polymer chain diameter a, due to the large size of the tracer particles, i.e. $p \approx s$. According to our simulations, the experimentally observed behavior that small particles are more effectively immobilized can be explained as follows; small particles diffuse into regions of stronger electrostatic attraction where they are strongly immobilized, whereas larger particles cannot access these regions.

Example 2 - Larger particles are slower: Xu and coworkers have studied the diffusivity of PEG coated polystyrene particles with diameters 100, 200, 500, 750 and 1000 nm in fresh bovine vitreus [16]. They report a behavior which is similar to our simulation data for repulsive interaction potentials ($U_0 > 0$). They found that the smaller particles (100 to 500 nm) diffuse relatively freely with diffusivities around $D/D_0 = 0.5$. The larger 750 nm and 1000 nm particles diffuse slower with $D/D_0 = 0.23$ and 0.014, respectively. In fig. 2.11b, the experimental data is compared to our simulation data for $U_0 = 10$ and $20k_BT$ for particle diameters $p/b = 0.1$, 0.2, 0.5, 0.75 and 1. Qualitative similarity between the experimental and the simulation results is achieved at an interaction range of $k = 0.2b$. Our model suggests the following diffusive mechanism in bovine vitreus; due to predominantly repulsive interactions between particles and the hydrogel polymers, charged particles have a tendency to stay away from the polymer chains. Only large particles experience strong steric hindrance and are thus more strongly immobilized than smaller ones.

In our simulations even non-monotonic size dependence is observed for attractive interaction potentials, see fig. 2.9. It would be interesting to test this prediction by performing experiments on cervicovaginal mucus with particles larger than 500 nm. In our comparisons in fig. 2.11 we keep the interaction strength constant for different steric diameters, in a more refined model, one would have to derive the particle diameter dependent interaction strength more accurately, e.g. by assuming a constant particle surface charge density.

2.4.3. Salt concentration effects

Ribbeck and coworkers found that an increase in ion concentration leads to an increase in diffusivity for charged particles in human mucus [14]. This increase in diffusivity is not related to a reorganization of the polymer network, but to modified electrostatic interactions between particle and hydrogel, since neutral particles did not experience an increase in diffusivity. Such behavior is qualitatively reproduced in our simulations, since according to eq. (2.9), an increase in ion concentration causes a decrease in interaction range k. Figure 2.12 shows the ion concentration C_{Ion} dependency of the diffusivity D/D_0 at different potential strengths U_0 for a steric diameter of $s = 0.1b$. To calculate the ion concentration, it is necessary to convert the relative interaction range k/b to physical units. For this we choose an exemplary mesh size of $b = 100$ nm on the order of experimentally reported mesh sizes for mucus [10, 48]. Particles that interact strongly with the polymer chains experience a very pronounced increase in diffusivity as the ion concentration increases. At high ion concentrations, the relative diffusivity approaches the value obtained for purely steric hindrance. At very small decreasing ion concentrations an increase in diffusivity occurs, similar to the results in fig. 2.5. This increase corresponds to very small ion concentrations $C_{\mathrm{Ion}} < 0.5$ mM, which experimentally might be difficult to reach.

In order to quantitatively test our model, we compare our simulation data for the relative diffusivity D/D_0 with experimental measurements on Alexa488 diffusion in charged

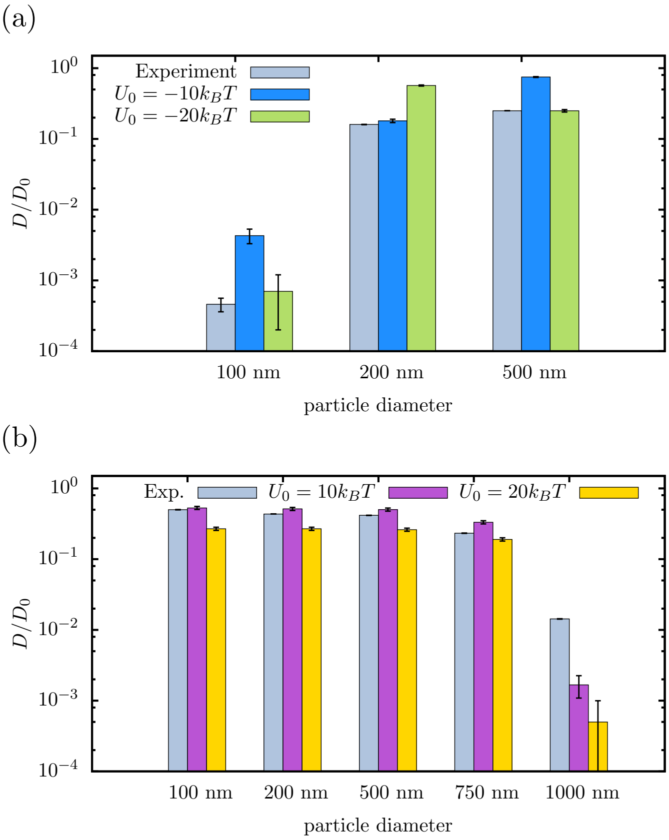

Figure 2.11. Comparison of simulation results (in color) and experimental data (in grey). (a) Experimental data by Lai and coworkers [10] and simulation data obtained for particle diameters $p/b = 0.1, 0.2, 0.5$ and $p/b = 0.2, 0.4, 0.9$ for $U_0 = -10k_BT$ and $U_0 = -20k_BT$, respectively, with the interaction range set to $k = 0.1b$. (b) Experimental data by Xu and coworkers [16] and simulation data obtained at repulsive potential strengths $U_0 = 10$, $20k_BT$ for $p/b = 0.1$, 0.2, 0.5, 0.75 and 1.0, with the interaction range set to $k = 0.2b$. The labels on the x-axis correspond to the experimental particle diameters.

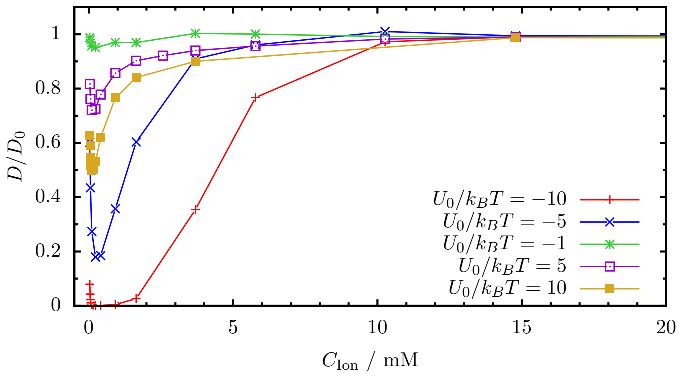

Figure 2.12. Relative diffusivity D/D_0 in dependence on the molar ion concentration C_{Ion} for different electrostatic interaction strengths U_0. The steric diameter is $s = 0.1b$ with an exemplary mesh size of $b = 100\,\text{nm}$. C_{Ion} is calculated by use of eq. (2.9). The lines are included to guide the eye.

dextran hydrogels. Alexa488 is a negatively charged fluorescent molecule and dextran a synthetic, cross-linked hydrogel. For the experimental methods we refer to our previous publication [54]. The experimental data is presented as full symbols in fig. 2.13a, where the D_0 value corresponds to the diffusivity of Alexa488 in buffered solution without any dextran polymers [54]. Alexa488 in negatively charged dextran(-) (blue diamonds) diffuses with the same relative diffusivity over the full range of investigated ion concentrations, i.e. at $D/D_0 \approx 0.9$. This indicates that repulsive electrostatic interactions do not, or only very little, affect the diffusivity. In positively charged dextran(+) however, negatively charged Alexa488 molecules are highly immobilized at small ion concentrations (red squares). Their mobility strongly increases with increasing ion concentration up to a value of $D/D_0 \approx 0.9$, which corresponds to the mobility of Alexa488 in similarly charged dextran(-). Hence, negatively charged Alexa488 particles are immobilized due to electrostatic interactions with oppositely charged dextran(+) and at increasing ion concentration, those interactions are screened. To compare the experimental data to simulation data we, as in section 2.4.1, set the steric diameter to $s = a + p = 2.3\,\text{nm}$. There is no definitive data on the mesh size of dextran hydrogels available. Some experimental studies report a mesh size on the order of 10 nm [7, 50]. We choose a mesh size of $b = 23\,\text{nm}$, which is reasonably close to the experimental estimations and leads to good agreement between simulation and experimental data. We use the interaction strength U_0 as a parameter to fit the D/D_0 simulation data to the experimental data for Alexa488 diffusion in dextran(+). As shown in fig. 2.13a, we find good qualitative, almost quantitative agreement at a potential strength of $U_0 = -8k_BT$, particularly at low ion concentration. The ratio of the linear charge densities of dextran(-) to dextran(+) is 0.6, since dextran(+) has about one positive amine group per three glucoses, and dextran(-) about one negative charge per five glucoses. Hence, to simulate the repulsive case of Alexa488 in dextran(-), we set the interaction potential strength to $U_0 = 5k_BT$, as an approximation to the experimental charge ratio. At ion concentrations $C_{\text{Ion}} > 40\text{mM}$, the experimental and simulation data curves are qualitatively similar, but with an offset of $\Delta D/D_0 \approx 0.1$, which can be

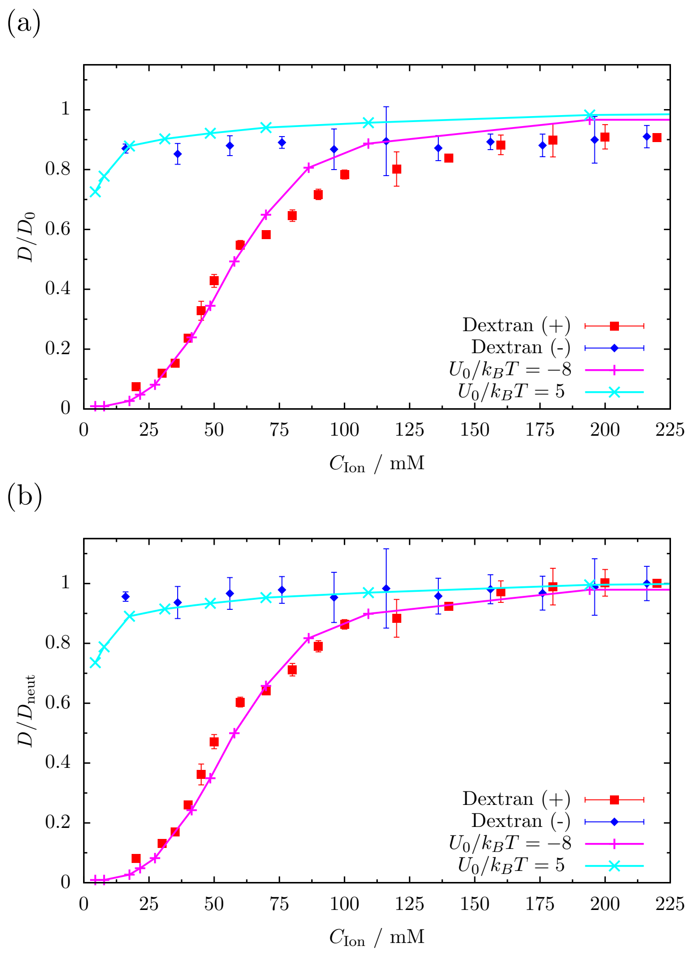

Figure 2.13. Comparison of simulation data to experimental results [54]. Simulations, indicated by connected crosses and plus signs are performed with a steric diameter of $s = 0.1b = 2.3$ nm. The experimental data, indicated by unconnected, filled symbols, is obtained by fluorescence correlation spectroscopy of Alexa488 molecules in charged dextran hydrogels, under 10 mM MES buffer solution and under varying NaCl concentration [54]. In plot (a) the relative diffusivity D/D_0 is plotted over the total ion concentration C_{Ion}, including buffer and NaCl. In plot (b) the same data is shown with D scaled by D_{neut}, which is the experimentally determined diffusivity of Alexa488 in neutral dextran [54]. The lines are included to guide the eye.

attributed to the simple way our model treats the neutral gel, i.e. the neglect of attractive non-electrostatic interactions and hydrodynamic effects. This effect can be canceled by dividing the diffusivities by the diffusivity in a neutral gel D_{neut}. Experimentally, this is the diffusivity of Alexa488 in neutral dextran of comparable molecular mass at 1 %w/v polymer concentration [54]. In this form, presented in fig. 2.13b, the simulation data and experimental data are in even better agreement. There remains a discrepancy in the diffusive behavior for small C_{Ion} at a repulsive potential strength $U_0 = 5k_BT$. The simulation data shows a decrease in diffusivity, whereas the experimental data remains constant. This may be due to cancellation of repulsive charge interactions by attractive hydrogen-bonding interactions between the particle and the polymer chain or residual attractive hydrophobic interactions.

By use of eq. (2.11) we can estimate U_0 for the electrostatic interaction between a dextran polymer and an Alexa488 monomer. Assuming that the charge along the dextran polymer is approximately uniformly distributed, the line charge density follows as $\tau^+ = 1/(3\,a) \approx 0.83\mathrm{nm}^{-1}$ for dextran(+) and $\tau^- = -1/(5\,a) \approx -0.5\mathrm{nm}^{-1}$ for dextran(-) where $a = 0.4\mathrm{nm}$. Since Alexa488 has a net charge of $-2e$, we set $z_p = -2$. The expression in eq. (2.11) depends on the Debye length k. Consequently, we obtain a range of $-3.5k_BT > U_0 > -6k_BT$ for dextran(+) and $2.1k_BT < U_0 < 3.6k_BT$ for dextran(-) for the ion concentration range between 2 and 225 mM. These values for U_0 are on the same order as our fit values of -8 and $5k_BT$ for dextran(+) and dextran(-). Considering the simplicity of our model and the neglect of non-linear charge effects, we consider this agreement satisfactory.

2.5. Conclusion

A simple model is used to simulate nanoparticle diffusion in cross-linked hydrogels. The hydrogel structure is modeled via a rigid, cubic periodic lattice. Steric interactions are described by a short-range potential, while nonsteric interactions are included via an exponential potential between the hydrogel polymers and the diffusing particle. We find that the long-term relative diffusivity behaves very different for attractive and repulsive interactions in the limit of strong interaction strengths. A simple analytical approximation reproduces our simulation results for point particles very well.

To test our model predictions, we compare with published experimental data on Alexa488 nanoparticle diffusion in synthetic dextran hydrogels, measured by FCS [54]. This comparison confirms that electrostatic interactions greatly influence the filtering capacity of hydrogels, in a highly asymmetric fashion regarding the sign of the interaction. Attractive electrostatic interactions greatly reduce the mobility of the charged tracer particles, whereas repulsive electrostatic interactions have a much weaker effect. An attractive interaction potential causes *sticking*, i.e. the particle tends to remain near the polymer chain intersections at the corners of the simulation box. A repulsive potential leads to *exclusion*, where the particle tends to remain in the center of simulation box. The good agreement between simulation and experimental data suggests that our model indeed captures the mechanism governing charged nanoparticle diffusion in hydrogels, namely the competition between steric hindrance and electrostatic interactions.

For attractive interaction potentials anti-size filtering can occur, i.e. smaller particles can be more strongly immobilized than larger ones, which agrees with experimental findings for 100, 200 and 500 nm particle diffusion in cervicovaginal mucus [10]. In our simulations, a maximum in relative diffusivity appears for intermediate particle diameters for attractive interaction potentials. This non-monotonic size dependence predicted by our model could, in principle, be tested by performing further experiments on cervicovaginal mucus with particles larger than 500 nm. In contrast, experimental data on diffusion of similar nanoparticles in bovine vitreus shows that diffusing particles over a wide range of diameters (100 to 500 nm) experience the same relative diffusivity [16]. This effect is reproduced by our model, for a repulsive interaction potential. Hence, we suggest that the different experimental findings may be due to predominantly repulsive electrostatic interactions in bovine vitreus and attractive electrostatic interactions in cervicovaginal mucus.

We find sticking and exclusion to be maximal at intermediate interaction ranges. Since the interaction range is related to the ionic strength, our model predicts a maximal filtering capacity of a hydrogel at a certain ion concentration.

Our model exhibits a linear dependency of the diffusivity on the polymer concentration. This is in contrast to experimental findings that typically report a stretched exponential dependency. The stretched exponential dependency may arise, if hydrodynamic interactions are included into our model. Furthermore, Kirch and coworkers [8] have suggested that larger particles might be able to locally break up cross-links between polymer chains in synthetic hydrogels. Biopolymer hydrogels, on the other hand, form a stiff network and our model might be more applicable here [8]. To further refine our model, additional effects may be included like random pore sizes and polymer network flexibility. This would create a possibility for particles larger than the average mesh size to diffuse with nonzero diffusivity. Lieleg and coworkers suggest that the charge distribution along mucin polymer chains is heterogeneous [14, 21]. Our model could also be adjusted to accommodate randomly distributed patches of attractive and repulsive interactions.

3. Particle Trapping Mechanisms are Different in Spatially Ordered and Disordered Interacting Gels

Bibliographic information: The contents of this chapter have been published in a peer-reviewed journal. Reprinted with permission from Ref. [iii].

3.1. Introduction

Hydrogels like mucus, the extracellular matrix (ECM) and the nuclear pore complex form natural barriers for pathogens and play an important role in regulating the exchange of molecules and particles between organelles and cells [1]. Even though the filtering capabilities of such hydrogels are of high importance for biological function, they are still not fully understood. Numerous experimental and theoretical studies investigated the mechanisms that determine the mobility of particles inside gels, as one main result it was found that nonsteric interactions between the gel and the diffusing particle, which can be attractive or repulsive, are a major factor in addition to purely steric obstruction effects. Electrostatic interactions in particular determine the mobility of charged particles in mucus [1,10,16–18,21,23,24,68,69], the ECM [1,11,14,20] and bacterial biofilms [19]. Charge is also suggested to be a main ingredient regulating diffusion through the nuclear pore complex [1,70]. Regarding the sign of the electrostatic interactions, a number of experimental papers report different diffusive behavior for positively and negatively charged particles in gels that have a given net charge [17,18,22,23,54,71]. We previously have investigated diffusion of spherical particles in an ordered cubic lattice of rigid cylindrical fibers as a hydrogel model [54,71]. Straight rigid fibers have previously been used successfully to model the stiff collagen network of the ECM [9,34] and mucus [71]. For mucus, recent experimental research has shown that nanoparticle motion is obstructed by a relatively rigid polymer scaffold [8]. Furthermore, single particle tracking revealed that some particles are almost completely immobilized in mucus inside a small volume, while others are rather mobile [10,14], indicating that mucus consists of fairly stiff and spatially inhomogeneous polymeric structures. In our previous model we included the effects of attractive and repulsive interactions on particle diffusivity with an exponentially screened interaction potential between the fibers and the particle [54,71]. With this simple gel model, we demonstrated that nonsteric interactions determine the effective particle diffusivity in a crucial fashion and usually dominate over steric hindrance effects. In particular, we showed the particle filtering to be charge asymmetric, meaning that particles are more strongly immobilized in oppositely charged gels, i.e. for attractive interactions, than in similarly charged gels, in agreement with experimental findings [17,18,22,23,54]. There

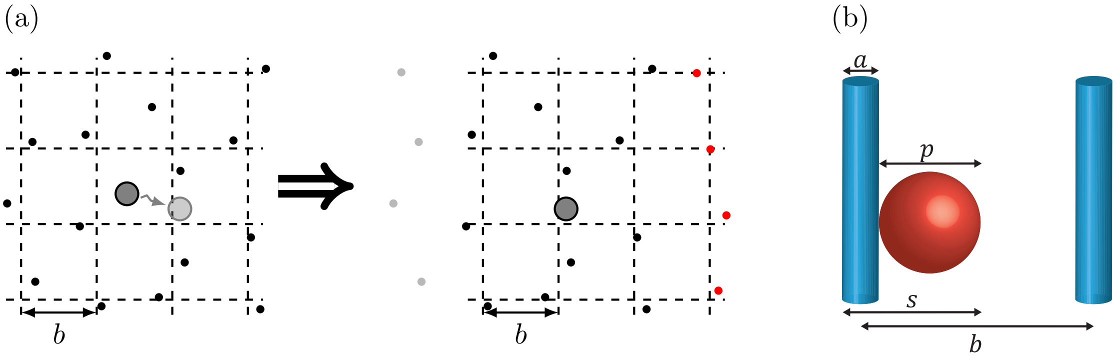

Figure 3.1. (a) The black dots indicate the positions of the fibers parallel to the z-axis. In the presence of spatial disorder, the fibers are displaced from their positions on the reference square lattice of spacing b by Gaussian random numbers with a standard deviation of $\sigma_d/b = 0.2$. The diffusing particle, drawn as a circle, crosses the boundary of the central cell in x-direction (left figure). In the simulation model, when this happens, the gray fibers to the left are removed and the red fibers are added at the right boundary (right figure). (b) Schematic definition of the particle diameter p, the fiber diameter a, the steric diameter $s = a + p$ and the gel mesh size b.

are a whole number of other pertinent theoretical studies on particle diffusion in crowded media [33, 36, 38–40, 60]. In the present paper, we consider disordered fiber lattices and in particular the transition from ordered cubic to spatially disordered gels in combination with attractive and repulsive nonsteric as well as steric interactions.

Our main results are as follows: While particle diffusion in purely steric gels depends only weakly on the spatial arrangement of the fibers if the particle is smaller than the mesh size, in accordance to previous theoretical results [9, 33, 39], the diffusive behavior in the presence of long-ranged, nonsteric interactions between particle and fibers depends drastically on the presence of spatial disorder of the gel. In particular, for attractive nonsteric particle-gel interactions we find different particle trapping mechanisms for spatially ordered and disordered gels. In highly ordered gels, particles are attracted to the vertices of the cubic fiber lattice where they become immobilized for small fiber volume fractions. In contrast, in disordered gels, regions of high local fiber density form trapping areas that strongly attract and thereby immobilize the particle very effectively, as has previously been proposed on the basis of experimental findings [11, 16]. The influence of gel disorder is less pronounced for repulsive nonsteric interactions. To test our model, we compare our simulated particle diffusivities with previously published experimentally measured particle diffusivities in different biogels. For negatively charged Alexa488 fluorophore molecules in gels consisting of neutral, positive and negative dextran polymers [54] we find good qualitative agreement of the diffusivity between experiment and simulation as a function of the fiber volume fraction.

3.2. Methods

The diffusive motion of the particle is governed by the overdamped Langevin equation

$$\dot{r}_i(t) = -\mu_0\, \partial_i U(\vec{r}(t)) + \zeta_i(t)\ , \quad (i = x, y, z)\ , \tag{3.1}$$

where $\dot{r}_i$ is the i-th component of the particle velocity, ∂_i the spatial derivative, U is the potential and μ_0 the bulk particle mobility. The random velocity ζ_i is a stochastic variable, modeled with Gaussian white noise

$$\langle \zeta_i(t) \rangle = 0\ , \tag{3.2}$$

$$\langle \zeta_i(t)\, \zeta_j(t') \rangle = 2\mu_0 k_B T\, \delta(t - t')\, \delta_{ij}\ , \tag{3.3}$$

where δ_{ij} is the Kronecker delta, k_BT is the thermal energy and the indices i, j denote Cartesian components. Since we are interested in the long-time diffusivity of the particle, the particle mass is neglected in the equation of motion (3.1). By discretizing the Langevin equation with time step Δt, an iterable equation for the change of the particle position is obtained,

$$\Delta\tilde{r}_i \ = \ -\, \tilde{\mu}\, \tilde{\partial}_i \tilde{U} \ + \ \sqrt{2\tilde{\mu}}\, \tilde{\zeta}_i\ , \tag{3.4}$$

where $\Delta\tilde{r}_i$ is the displacement of the particle and $\tilde{\zeta}_i$ is a Gaussian distributed random number with zero mean and variance $\langle \tilde{\zeta}_i\, \tilde{\zeta}_j \rangle = \delta_{ij}$. The tilde indicates rescaled variables. The potential $\tilde{U}$ is rescaled by the thermal energy k_BT and all lengths $\tilde{r} = r/b$ are rescaled by the mesh size b (c.f. fig. 3.1a). The rescaled timestep is defined as

$$\tilde{\mu} = \frac{\Delta t\, \mu_0 k_B T}{b^2}\ . \tag{3.5}$$

For the simulations a small enough rescaled time step $\tilde{\mu}$ must be chosen. We tested different time steps and found no increase in accuracy for $\tilde{\mu} < 5 \times 10^{-6}$. To ensure that we are within the continuum limit we chose $\tilde{\mu} = 10^{-6}$ for all data presented in this chapter.

The diffusivity D of the particle is obtained by linearly fitting the mean-squared displacement $\langle \Delta r^2(t) \rangle$ in the long-time limit according to

$$\langle \Delta r^2(t) \rangle \ = \ \int_0^{(T-t)} \frac{dt'}{T - t} (\vec{r}(t + t') - \vec{r}(t'))^2 \ = \ 6D\, t\ , \tag{3.6}$$

where T denotes the trajectory length. The diffusivity of the particle if no gel is present is denoted by $D_0 = \mu_0 k_B T$. For each data point, we perform a single long simulation consisting of at least 10^9 steps. Due to the stochastic nature of the resulting trajectory, extracted relative diffusivities D/D_0 exhibit a residual error of not more than 5% for $D/D_0 > 0.01$. For smaller diffusivities, the error becomes substantially larger. In the supplementary information in fig. 3.11, we show that the long-time limit in eq. (3.6) is always reached in our simulations.

The simulated gel consists of 48 fibers, i.e. 16 fibers parallel to each axis x, y and z. We introduce spatial disorder by displacing the fibers from positions on a reference cubic lattice. The displacement of each fiber is a random vector orthogonal to the fiber axis, sampled from a Gaussian distribution with zero mean and standard deviation σ_d. In fig. 3.1a we present a sketch of our model for $\sigma_d/b = 0.2$, the reference cubic lattice with mesh size b is indicated by dashed lines. When the particle leaves the central cell of the reference cubic lattice, the eight distal fibers are removed and eight new fibers are added on the other side at new random positions. This process is illustrated in fig. 3.1a for a particle in the xy-plane that leaves the central cell in the positive x-direction. Thus, in our simulation model, the gel changes as the particle moves across cells. This avoids the particle from being trapped in a locally crowded gel configuration.

Steric hindrance between the particle and the fibers is modeled by a truncated, shifted Lennard Jones potential

$$U_{\text{steric}}(\vec{r}) = \sum_{n=1}^{48} \begin{cases} 4\epsilon \left[\left(\frac{s}{2\rho_n} \right)^{12} - \left(\frac{s}{2\rho_n} \right)^{6} + \frac{1}{4} \right], & \rho_n \leq 2^{-5/6} s \\ 0\,, & \rho_n > 2^{-5/6} s\,, \end{cases} \tag{3.7}$$

where the energy parameter is fixed at $\epsilon = 1\,k_BT$, ρ_n is the closest distance between the particle and the nth fiber and $s = a + p$ is the steric diameter, i.e. the sum of the diameters of the fibers a and the particle p, as shown in fig. 3.1b. The long-ranged nonsteric interaction potential between the fibers and the particle is defined as

$$U_{\text{int}}(\vec{r}) = \sum_{n=1}^{48} U_0 \exp\left(-\frac{\rho_n}{k} \right)\,, \tag{3.8}$$

where k is the interaction range and U_0 the strength of the potential. For negative U_0 the potential is attractive and for positive U_0 it is repulsive. For electrostatic interactions k corresponds to the Debye screening length [55]

$$k^{-2} = 4\pi l_B I\,, \tag{3.9}$$

where $l_B = e^2/4\pi\varepsilon k_BT$ is the Bjerrum length, e is the elementary charge and ε the permittivity. $I = \frac{1}{2}\sum_j n_j\, z_j^2$ is the ionic strength and z_j the valence of salt ion j and n_j its number density. The salt number density n is related to the molar ion concentration C_{Ion} through $C_{\text{Ion}} = n/N_A$, where N_A is the Avogadro constant. U_0 can be interpreted as the product of the particle charge and the linear polymer charge density [71]. Thus, eq. (3.8) becomes an effective electrostatic interaction potential between charged fibers and a charged particle. Following our previous research on particle diffusion in interacting gels [54, 71] we neglect hydrodynamic interactions.

3.3. Results

Before we discuss the resulting particle diffusivity D, we characterize the spatial gel structure for different disorder strengths σ_d. To illustrate the transition from a completely ordered gel, $\sigma_d/b = 0$, to a highly disordered gel, $\sigma_d/b = 0.9$, we show the distribution of the smallest distances d_{min} between parallel fibers for different σ_d in fig. 3.2. For the ordered gel, $\sigma_d = 0$, the distribution corresponds to a δ-peak. For increasing σ_d, d_{min}

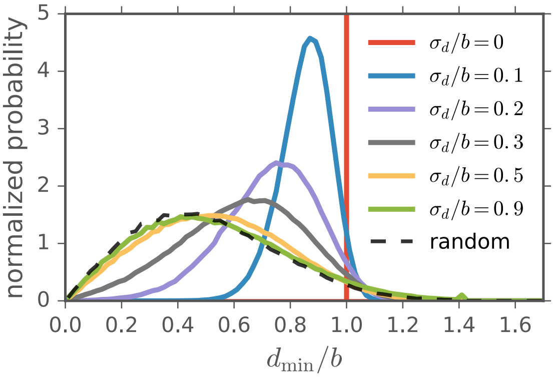

Figure 3.2. Distribution of the smallest distances d_{min} between parallel fibers for different disorder strengths σ_d. For $\sigma_d/b = 0$ the smallest distance is b and the distribution is a delta peak. The dashed line is the distribution for 16 parallel fibers that are placed on a $3b \times 3b$ square at random positions, which agrees well with the distribution for $\sigma_d/b = 0.9$.

becomes more broadly distributed. The dashed line in fig. 3.2 corresponds to the distribution for 16 parallel fibers that are placed within a $3b \times 3b$ square at uniformly distributed random positions, which agrees with the distribution for $\sigma_d/b = 0.9$ (green line). Thus, the value $\sigma_d/b = 0.9$ corresponds practically to an uncorrelated fiber placement.

The presentation of our simulation results is organized as follows. First, we examine diffusion in purely steric gels and compare our modeling results to experimental data for neutral gels. After this we investigate how disorder affects the diffusivity in the presence of long-ranged interactions between the particle and the gel and compare with experimental data for charged gels.

3.3.1. Purely steric gels

In fig. 3.3a we present the relative particle diffusivity D/D_0 as a function of the fiber volume fraction ϕ for purely steric gels with $U_0 = 0$ for various disorder strengths σ_d. The second x-axis at the top indicates the rescaled steric diameter $s/b = (a+p)/b$. The fiber volume fraction is given by

$$\phi = 3\pi(a/2b)^2 \tag{3.10}$$

and depends on the fiber diameter a. In order to present our results as a function of the volume fraction we thus have to make a specific choice for the value of a. In fig. 3.3a we use a small fiber particle size ratio $a/p = 0.05$, so in the numerical simulations, the fibers are very thin lines. Experimentally, a ratio of $a/p = 0.05$ corresponds to a range of particle diameters p of $60-200$ nm, for a range of fiber diameters a of $3-10$ nm which is realistic for mucin gels [72]. This means that for mucus the mesh size b in fig. 3.3a is between ~ 50 nm for large $\phi \sim 0.01$ and ~ 1000 nm for small $\phi \sim 0.0005$. Note, that in the simulations only the ratio a/p appears, which determines ϕ via eq. (3.10). For the completely ordered cubic lattice with $\sigma_d/b = 0$, the diffusivity becomes zero for $s > b$ ($\phi > 0.0053$), since the particle can not move between adjacent fibers anymore [71]. For increasing disorder $\sigma_d > 0$

this complete particle immobilization for $s > b$ is prevented. If the particle encounters a dead end, it will eventually return to where it came from and the fiber lattice is partially rebuilt (c.f. fig. 3.1a). As a consequence, irreversible particle trapping is avoided and the particle has a finite mobility even at large ϕ for $\sigma_d > 0$. In fig. 3.3b we plot the diffusivity as a function of the effective volume fraction ϕ_{eff}, which is the ratio of the gel volume that is accessible to the center of the particle to the total volume. We determine ϕ_{eff} by Monte-Carlo integration, similar to [39]. For 200 consecutive gel structures generated during a simulation, 10^6 random positions are sampled to check whether they collide with one of the fibers. For the $\sigma_d/b = 0$ data the effective volume fraction is given analytically by $\phi_{\mathrm{eff}} = (3\pi ba^2/4 - \sqrt{2}a^3)/b^3$. Figure 3.3b demonstrates that the data collapse onto a master curve, i.e., that the effects of the spatial disorder almost disappear in this representation, similar to previous findings [39]. Thus, a diffusion model based on the effective volume ϕ_{eff} describes particle diffusion in disordered purely steric gels very nicely.

Figure 3.3a includes the previously suggested scaling function [73]

$$D/D_0 = \exp(-0.84[\phi(1 + p/a)^2]^{1.09}) \ , \tag{3.11}$$

which is a heuristic fit to Brownian dynamics simulations for spherical particles in gels of randomly oriented, rigid straight fibers and has been shown to agree with other simulation models as well [29]. We find that our simulation results agree perfectly with eq. (3.11) for an intermediate value $\sigma_d/b = 0.5$. This indicates that our disordered gel model has similar diffusion properties as a model with random fiber orientations, in accordance to the findings by Masoud and Alexeev who have demonstrated that for purely steric random gels the diffusivity is almost independent of the exact fiber lattice geometry [33].

In fig. 3.3c we compare our diffusivity results to a general stretched exponential dependency

$$D/D_0 = \exp(-\alpha\phi^n) \ , \tag{3.12}$$

where we show the logarithm of D/D_0 in a log-log plot. As indicated by the straight lines, the exponent n varies slightly from $n = 1.04 \pm 0.04$ for $\sigma_d/b = 0.9$ to $n = 1.14 \pm 0.06$ for $\sigma_d/b = 0.5$ (c.f. table 3.1) for highly disordered gels, and thus is very close to the exponent $n = 1.09$ in eq. (3.11). In contrast, for most experimental data, the stretched-exponential parameter is between $n = 0.5$ and 1 [54, 63, 66, 74]. We are aware of only one experimental study that reports larger n values in the range of 1.1 to 2.4 for different probes in PDMS solution [67]. The effect of HI on particle diffusion in purely steric gels has been extensively studied [27, 29, 75]. It was found that the effect of HI can approximately be taken into account by multiplying the diffusivity for simulations without HI, D_{noHI}/D_0 (the steric part), by the spatially averaged short-time relative diffusion coefficient $\langle D_s\rangle/D_s^0$ (the hydrodynamic part), i.e. $D/D_0 \approx D_{\mathrm{noHI}}/D_0 \times \langle D_s\rangle/D_s^0$. For gels consisting of disordered, randomly oriented straight fibers the following expression was proposed [28, 29]:

$$D/D_0 = \exp(-\pi\phi^m)\ \exp(-[0.84(1 + p/a)^2\,\phi]^{1.09}) \ , \tag{3.13}$$

where the first exponential factor accounts for hydrodynamic effects and the second factor accounts for steric effects. Note that the steric part corresponds to eq. (3.11). The heuristic

Table 3.1. The parameters of a stretched exponential fit, eq. (3.12), to the data presented in figs. 3.3a and 3.3c. The errors correspond to the estimated standard deviations of the fit parameters.

σ_d/b	0	0.1	0.2	0.3	0.5	0.9
$\alpha \times 10^{-3}$	4 ± 3	2 ± 1	1.9 ± 0.7	1.0 ± 0.4	0.8 ± 0.2	0.35 ± 0.08
n	1.4 ± 0.2	1.3 ± 0.2	1.3 ± 0.1	1.16 ± 0.07	1.14 ± 0.06	1.04 ± 0.04

expression for the exponent $m = 0.174 \ln(59.6a/p)$ was obtained by fitting simulation data for the ratios $a/p = 0.1 - 2$ [28]. Figure 3.3a represents eq. (3.13) for $a/p = 0.05$ as a dashed red line. Comparing the lines for eqs. (3.11) and (3.13), one can see that the diffusivities are significantly smaller with HI. According to eq. (3.13), the effect of HI increases monotonically with increasing fiber volume fraction ϕ for purely steric gels. In fig. 3.3c we compare eq. (3.13) (red dashed line) with a simple stretched exponential eq. (3.12) with exponent $n = 0.35$ (black dotted line). In other theoretical work a scaling exponent of $n \sim 0.7$ was reported for simulations with HI of random, cross-linked fiber networks with different cross-linking densities and $a/p = 0.5$ and 0.3 [33]. Thus, we conclude that the increased value of n in our simulations in comparison to experiments can likely be attributed to the lack of hydrodynamics in our model. Comparisons to experimental data are presented in fig. 3.4. Figure 3.4a shows results for RNAse diffusion in polyacrylamide gel with a diameter ratio $a/p = 0.32$ by Tong and Anderson [76], fig. 3.4b for BSA diffusion in polyacrylamide gel with a ratio $a/p = 0.18$ by Tong and Anderson and Park et al. [76, 77] and fig. 3.4c for BSA diffusion in calcium alginate with a ratio $a/p = 0.1$ by Amsden [28]. The estimated fiber-particle diameter ratios a/p are taken from [29]. We find qualitative agreement between simulation and experiment in all three cases for highly disordered gels with $\sigma_d/b = 0.9$ and 0.5. For large ϕ the experimental and the simulation data agree quantitatively in figs. 3.4 b and c, this indicates that hydrodynamic interactions are irrelevant compared to steric hindrance effects for these dense systems. In contrast, at low ϕ our simulation model overestimates the diffusivity, as discussed above, presumably due to the lack of hydrodynamic interactions [29]. We conclude that the difference of the stretched-exponential parameters n extracted from our simulations ($n \sim 1.1$) versus experiments ($n \sim 0.7$) is mainly reflected by the deviation between experimental and simulated diffusivities at small to intermediate volume fractions. For ordered gels with $\sigma_d/b = 0$, we find significant disagreement between simulation and experiment, in particular at large volume fractions ϕ. This indicates that the gels used in the experiment are quite disordered and that our disorder model correctly describes the experimental gel structures.

3.3.2. Interacting gels

We move on to interacting gels. In figs. 3.5 and 3.6 we present the diffusivity D/D_0 as a function of the fiber volume fraction ϕ for repulsive and attractive interaction potential strength $U_0 = 10k_BT$ and $U_0 = -10k_BT$. The rescaled interaction range is $k/s = 0.5$ in fig. 3.5 and $k/s = 1.5$ in fig. 3.6. With the exception of fig. 3.5a we find the following

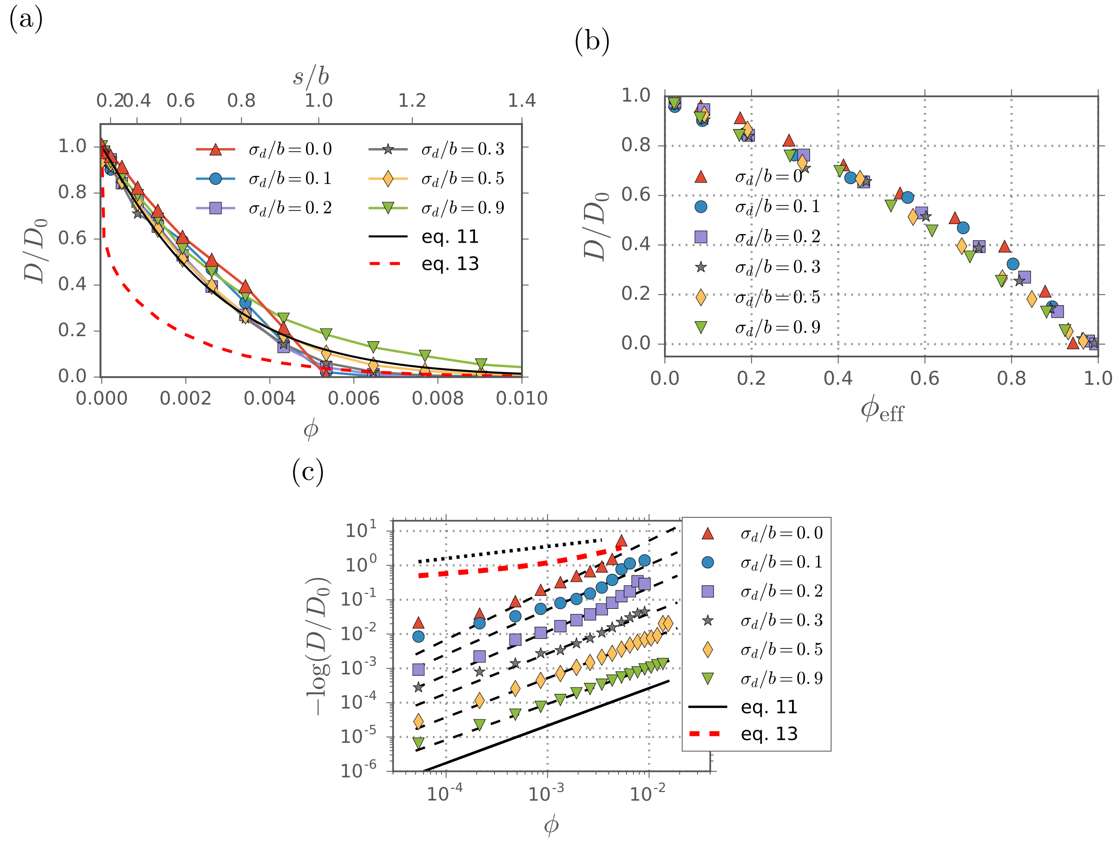

Figure 3.3. (a) Particle diffusivity in a purely steric gel as a function of the fiber volume fraction ϕ for a diameter ratio $a/p = 0.05$ and different disorder strengths σ_d. The plot includes an upper x-axis for the steric diameter s/b defined in fig. 3.1b. The continuous black line denotes the scaling function eq. (3.11), the dashed red line eq. (3.13). We find particularly good agreement between eq. (3.11) and our data for disorder strength $\sigma_d/b = 0.5$. (b) Particle diffusivity as a function of the effective fiber volume fraction ϕ_{eff} defined in the text for different σ_d, exhibiting collapse onto a master curve. In (c), the same data as in (a) is presented in a log-log versus log plot, shifted along the y-axis to avoid overlapping curves. The strongly disordered systems with $\sigma_d/b = 0.9$ and $\sigma_d/b = 0.5$ clearly exhibit a stretched exponential scaling. In contrast, for the ordered system with $\sigma_d = 0$ a stretched exponential scaling is only present for intermediate ϕ. The dashed straight lines are stretched exponential fits according to eq. (3.12), the fit parameters are given in table 3.1. The solid straight black line indicates a stretched-exponential eq. (3.11) with $n = 1.09$. The straight black dotted line denotes a stretched exponential in eq. (3.12) with $n = 0.35$.

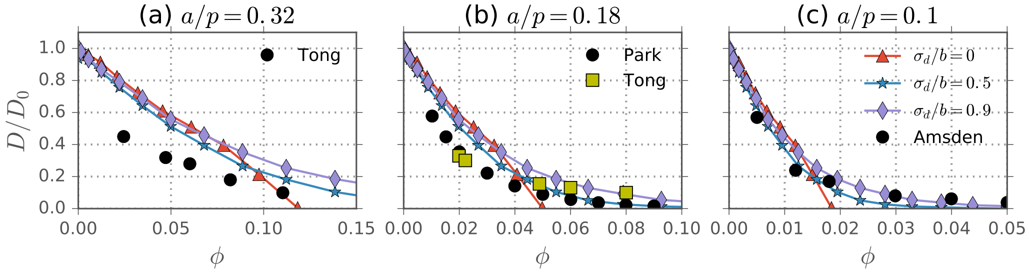

Figure 3.4. Particle diffusivity in purely steric gels as a function of the fiber volume fraction ϕ from simulations (connected symbols) for ordered ($\sigma_d/b = 0$) and disordered ($\sigma_d/b = 0.5$ and 0.9) gels in comparison to experimental data (unconnected symbols) for: (a) RNAse diffusion in polyacrylamide gel reported by Tong and Anderson [76] with a fiber/particle diameter ratio $a/p = 0.32$ [29]. (b) BSA diffusion in polyacrylamide gel reported by Tong and Anderson [76] and Park et al. [77] with $a/p = 0.18$ [29] and (c) BSA diffusion in calcium alginate gel reported by Amsden [28] with $a/p = 0.1$ [29]. The simulation data is the same in all three subfigures. We find qualitative agreement between our simulation model and the experiments for high disorder parameters $\sigma_d/b = 0.5$ and $\sigma_d/b = 0.9$ and not too low volume fraction.

behavior: In ordered gels, the particle diffusivity D exhibits a non-monotonic dependence on ϕ, whereas in disordered gels D decreases monotonically and steeply already at small ϕ. The non-monotonicity of D for ordered gels can be explained as follows. For increasing ϕ and fixed interaction range k/s, the interaction range relative to the mesh size increases. When the interaction range becomes comparable to the mesh size, roughly at $k/b \approx 0.2$, the interaction potentials of neighboring fibers start to overlap, which creates a rather smooth potential landscape and which thereby leads to an increase in diffusivity with increasing ϕ [71], as can be observed for small ϕ in figs. 3.5b, 3.6a and 3.6b for highly ordered gels. For larger values of ϕ, steric effects become important and give rise to a decrease of D with increasing ϕ. For all results in figs. 3.5 and 3.6, increasing the disorder generally leads to a decrease of D with some exceptions that will be discussed below.

Repulsive interactions induce mild exclusion trapping

In gels with repulsive nonsteric interactions the particle experiences mild *exclusion trapping*, i.e. it is confined to the space between the fibers. In ordered gels, $\sigma_d/b < 0.3$, the particle can travel in a relatively unobstructed fashion in between adjacent cells through the centers of the cubic cell faces [71], which is reflected in the high diffusivities in figs. 3.5a and 3.6a for particles with a diameter smaller than b which corresponds to $\phi < 0.0053$. For large $\sigma_d/b = 0.9$, the strong disorder creates random passageways of low fiber density, thus in figs. 3.5a and 3.6a the particle remains quite mobile even for large $\phi > 0.0053$, when the particle diameter exceeds the mesh size b. Intermediate disorder strengths $0.3 \leq \sigma_d/b \leq 0.5$ lead to the smallest particle mobilities. This non-monotonic dependence on σ_d is also visible in purely steric gels in fig. 3.3a, but in figs. 3.5a and 3.6a it is much more pronounced, due to the additional repulsive interaction potential. The qualitative similarity between

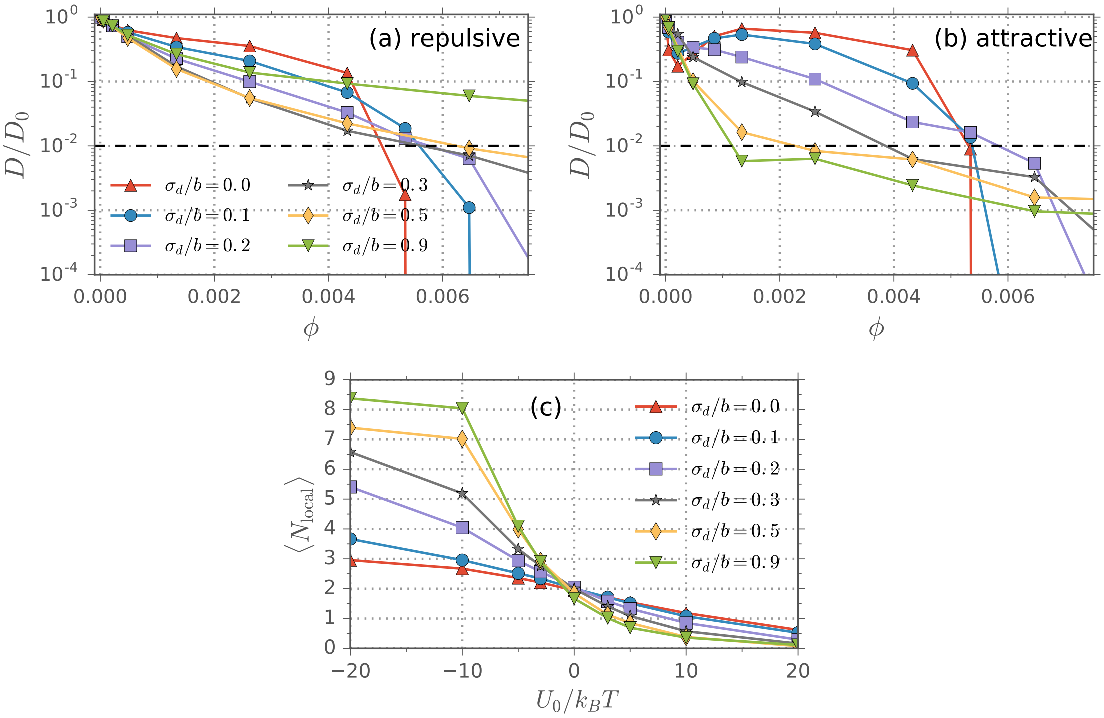

Figure 3.5. Particle diffusivity in interacting gels as a function of the fiber volume fraction ϕ for a fiber/particle diameter ratio $a/p = 0.05$ and short interaction range $k/s = 0.5$ for different σ_d for (a) repulsive interactions with $U_0 = 10k_BT$ and (b) attractive interactions with $U_0 = -10k_BT$. The diffusivity is much more sensitive to disorder for attractive than for repulsive interactions. The dashed line indicates the immobilization threshold defined by $D/D_0 = 0.01$. Figure (c) shows the average number of fibers $\langle N_{\mathrm{local}} \rangle$ within a distance of $b/2$ from the particle as a function of U_0. In attractive gels the particle moves into regions of high local fiber density (and thus high $\langle N_{\mathrm{local}} \rangle$) for increasing σ_d, in repulsive gels the particle moves into regions of small $\langle N_{\mathrm{local}} \rangle$.

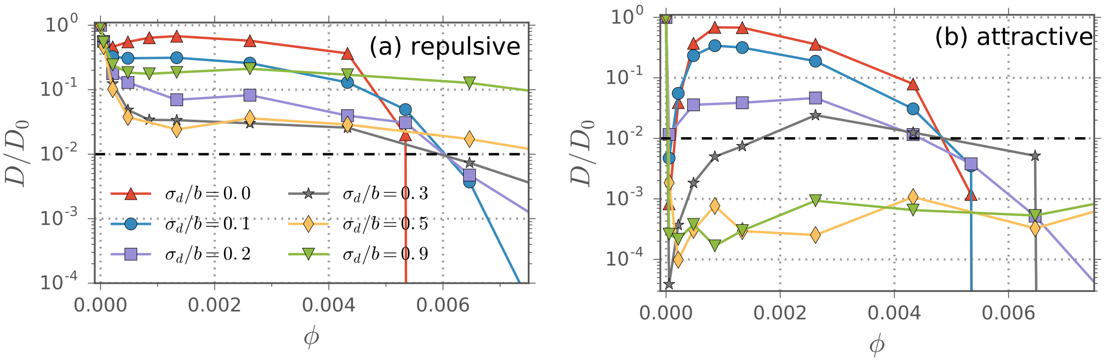

Figure 3.6. Particle diffusivity in interacting gels as a function of the fiber volume fraction ϕ for a fiber/particle diameter ratio $a/p = 0.05$ and large rescaled interaction range $k/s = 1.5$ for different σ_d for (a) attractive interactions with $U_0 = 10k_BT$ and (b) repulsive interactions with $U_0 = -10k_BT$. The dashed line indicates $D/D_0 = 0.01$. The interaction range is increased by a factor of 3 in comparison to fig. 3.5, which corresponds to a 9-fold decrease in terms of ionic strength (c.f. eq. (3.9)). This leads to a significant decrease in diffusivity for both attractive and repulsive U_0. Note that in (b) the data for $\sigma_d/b = 0.5$ and 0.9 exhibit large statistical errors due to limited sampling.

purely steric gels and gels with nonsteric repulsive interactions is also apparent when the diffusivity is plotted as a function of the disorder strength in fig. 3.7.

The different exclusion trapping mechanisms for repulsive interactions can be appreciated from the particle snapshots in fig. 3.8 for a highly ordered $\sigma_d/b = 0.1$ gel (top left) and a disordered $\sigma_d/b = 0.9$ gel (bottom left). The snap shots correspond to the case of $s = b$ ($\phi = 0.0053$) where the steric diameter is equal to the mesh size so the particle becomes strongly immobilized due to steric hindrance as well as the repulsive interaction effects. Both figures show particle position snap shots clustered in spaces of low local fiber density; for the disordered system, there are fewer and more pronounced clusters in regions that are devoid of fibers. Within these regions, the particle is quite mobile, thus D/D_0 is still relatively high for $\sigma_d/b = 0.9$ and $s = b$ ($\phi = 0.0053$) as seen in figs. 3.5a and 3.6a.

For attractive interactions disorder modifies trapping mechanism

For gels with attractive nonsteric interactions in figs. 3.5b and 3.6b the particle mobilities for disordered $\sigma_d/b = 0.3$ to 0.9 systems are significantly smaller than for ordered systems over almost the entire range of volume fractions ϕ. To understand this, it is instructive to consider the particle position snap shots in fig. 3.8 for $\sigma_d/b = 0.9$ gels and different steric diameters $s/b = 0.5$ ($\phi = 0.0013$, bottom center) and $s/b = 0.2$ ($\phi = 0.0002$, bottom right). The snap shots are from consecutive times during a single trajectory. They clearly indicate the tendency of the particle to stay in regions with locally increased fiber density during the simulation, which we refer to as *dense-region trapping*. The corresponding snap shots in ordered gels with identical k/s and U_0/k_BT are for an intermediate volume fraction $\phi = 0.0013$ evenly distributed (top center) and for a small volume fraction $\phi = 0.0002$ (top

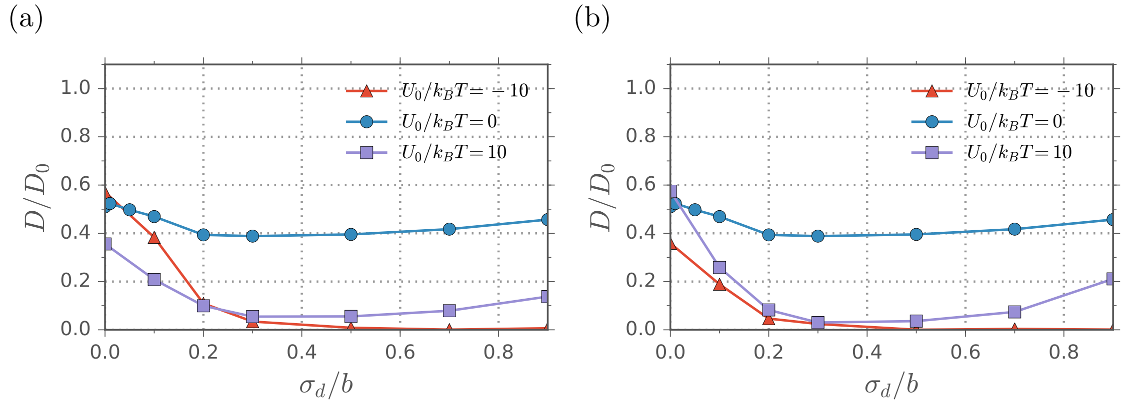

Figure 3.7. Particle diffusivity in interacting gels as a function of the disorder strength σ_d for $a/p = 0.05$ and a steric diameter of $s = 0.7b$ (corresponding to a gel volume fraction of $\phi \approx 0.003$). The rescaled interaction range is $k/s = 0.5$ for (a) and $k/s = 1.5$ for (b). The data for $U_0 \neq 0$ presented in (a) and (b) corresponds to data shown in figs. 3.5 and 3.6, respectively. Both the purely steric, $U_0 = 0$, and the repulsive case, $U_0/k_BT = 10$, exhibit a characteristic minimum around $\sigma_d/b \sim 0.3$. The attractive case, $U_0/k_BT = -10$, exhibits a monotonically decreasing diffusivity as a function of σ_d.

right) clustered around the vertices where three orthogonal attractive fibers create a local potential minimum. This illustrates that the *vertex trapping* mechanism in highly ordered attractive gels is most effective for small ϕ, as also seen in figs. 3.5b and 3.6b. In order to distinguish vertex and dense-region trapping, we show in fig. 3.5c the average number of fibers within a distance of less than $b/2$ from the particle, $\langle N_{\mathrm{local}} \rangle$, as a function of U_0 for $\phi = 0.0013$ ($s/b = 0.5$) and $k/s = 0.5$. For attractive interactions, $U_0 < 0$, the particle mostly stays in regions where several fibers are close together, corresponding to high $\langle N_{\mathrm{local}} \rangle$. The completely ordered $\sigma_d/b = 0$ gel has an upper bound of $\langle N_{\mathrm{local}} \rangle = 3$, which corresponds to three orthogonal fibers that meet at a vertex. For more disordered gels $\langle N_{\mathrm{local}} \rangle$ is significantly higher, confirming that in a disordered gel with attractive nonsteric interactions, particles are strongly immobilized in regions of high local fiber density. Lieleg and coworkers suggested that a similar effect leads to trapping of nanoparticles in the ECM, which they observed by studying single-particle trajectories of particles with a diameter comparable to the mesh size of the ECM [11]. The large difference of the trapping efficiency between vertex and dense-region trapping makes diffusion in gels with attractive nonsteric interactions particularly sensitive to spatial disorder, this is clearly demonstrated in figs. 3.5b and 3.6b.

For repulsive interaction potentials, $U_0 > 0$, in fig. 3.5c the particle tends to stay away from the fibers and preferentially stays in regions of small $\langle N_{\mathrm{local}} \rangle$, i.e. small local fiber density. Exclusion is reinforced in more disordered gels, since the particle can access regions with particularly small local fiber density. Figure 3.9 provides a schematic overview of the different trapping mechanisms for interacting gels.

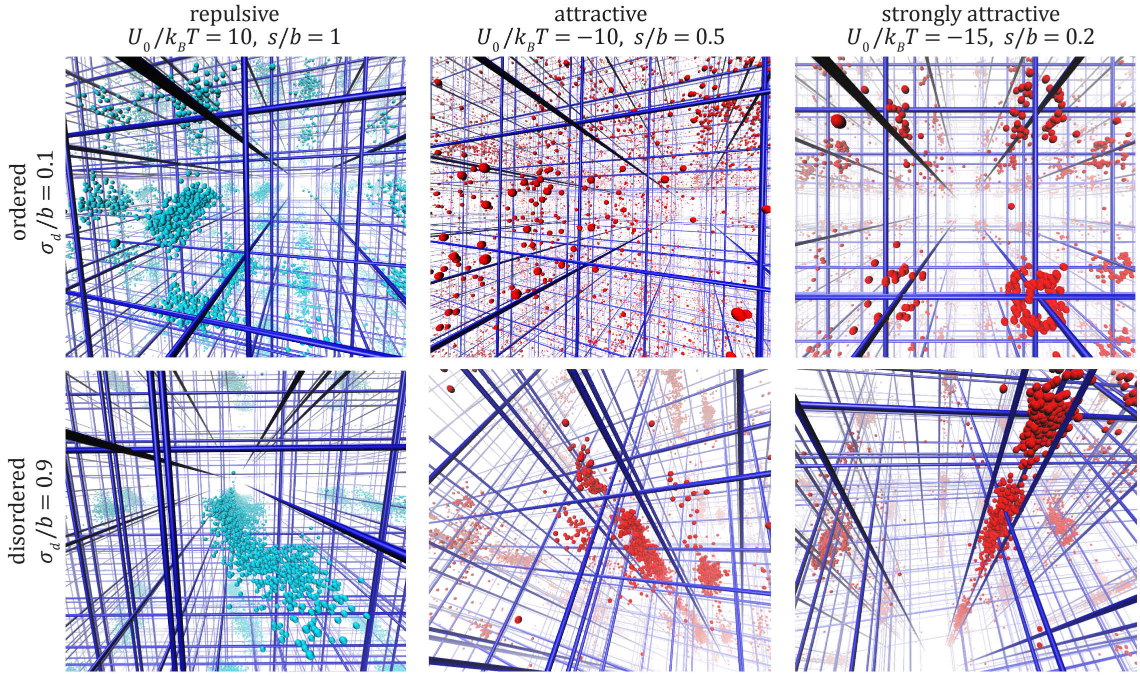

Figure 3.8. Particle position snap shots from a single trajectory at equally spaced consecutive times (colored spheres) in ordered and disordered gels taken from simulations of equal length. The spheres indicating the particle positions are not drawn to scale. The rescaled interaction range is fixed at $k/s = 0.5$. The top row shows results for highly ordered gels with a small disorder strength $\sigma_d/b = 0.1$ while the bottom row shows results for strongly disordered gels $\sigma_d/b = 0.9$. In the left figures, the particle-fiber interaction is repulsive with $U_0/k_BT = 10$, indicated by similarly colored spheres and fibers, and the steric diameter $s = b$ is equal to the mesh size, which corresponds to a fiber volume fraction of $\phi = 0.0053$ for $a/p = 0.05$. In the central column the fibers are attractive with $U_0/k_BT = -10$ and $s/b = 0.5$ ($\phi = 0.0013$). In the right figures the steric diameter is smaller, $s/b = 0.2$ ($\phi = 0.0002$), and the fibers are even more strongly attractive, $U_0/k_BT = -15$. The mean squared displacements over the particle trajectories are $\langle \Delta r^2(t) \rangle / b^2 = 3.5$ (top left), 215 (top center) and between 17 and 46 for the other figures. These figures visually demonstrate the three different trapping mechanisms, namely *exclusion trapping* (left figures) for repulsive nonsteric interactions, *vertex trapping* (top right) for ordered attractive gels and *dense-region trapping* (bottom middle and right) for disordered attractive gels.

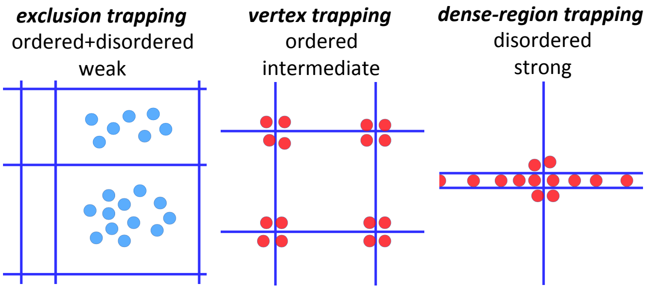

Figure 3.9. Schematic illustration of the different particle trapping mechanisms, namely *exclusion trapping*, *vertex trapping* and *dense-region trapping*.

3.4. Discussion

Particles in repulsive gels diffuse rapidly

Many experimental studies classify particles in terms of their ability to penetrate the mucus barrier, which is a desirable property for drug delivery purposes. Particles are typically classified as rapidly moving if they exhibit a relative diffusivity in mucus of more than $D/D_0 = 0.01$ [10,47,49,69]. Applying this classification scheme to our results, denoted by the broken horizontal lines in figs. 3.5 and 3.6, we find that particles always diffuse rapidly in gels with repulsive nonsteric interactions in figs. 3.5a and 3.6a as long as they are smaller than the average mesh size b. This is a consequence of the comparably weak exclusion trapping mechanism. Hence, particles that interact repulsively with the gel fibers, e.g. particles that are similarly charged as the gel or particles that are charge-neutral and hydrophilic, should be suitable for drug delivery purposes. Experimental studies for nanoparticle diffusion in mucus [17,22,23] and molecular dye diffusion in synthetic gels [54] arrive at the same conclusion.

Disordered gels immobilize interacting particles most effectively

The filtering capabilities of biopolymer gels like mucus and the ECM are of particular importance in biology. Interaction filtering can lead to the selective immobilization of a certain type of interacting particle, for example, in the ECM charged particles that interact with the fibers via electrostatic interactions are immobilized but not neutral particles [21]. For charged particles, interaction filtering can also involve filtering with respect to the sign of the charge, e.g. positively charged peptides are immobilized in porcine mucin hydrogel and negatively charged peptides are mobile [23]. Our results indicate that interaction filtering is much more effective for spatially disordered gels, than for ordered gels, since disordered gels hinder interacting particles for both interaction signs more strongly than ordered gels (c.f. fig. 3.7). In terms of the charge asymmetry, we find that disordered gels allow rapid diffusion for repulsive particle-gel interactions but effectively immobilize particles that are attracted to the gel by dense-region trapping. This can be seen, for example, for $\sigma_d/b \geq 0.5$ in fig. 3.7. For ordered gels, by contrast, exclusion trapping and vertex trapping are both comparably weak for most volume fractions, which makes them much less suitable for interaction filtering.

Ion concentration strongly impacts the diffusivity of charged particles in charged gels

According to eq. (3.9) the electrostatic interaction range k is related to the ion concentration as $C_{\mathrm{Ion}} \propto k^{-2}$. Hence, to appreciate how the diffusive behavior of charged particles in charged gels depends on the ion concentration, it is useful to compare our simulation data for interaction range $k/s = 0.5$ and $k/s = 1.5$, see fig. 3.5 and fig. 3.6, respectively. This increase in interaction range corresponds to a 9-fold decrease in terms of ion concentration. For repulsive interaction U_0 (figs. 3.5a and 3.6a) decreasing the ionic strength has a significant impact. On the one hand, it significantly decreases the particle diffusivity for small volume fractions $\phi < 0.004$. On the other hand, decreasing the ionic strength qualitatively changes the diffusive behavior for all σ_d, e.g. we find a non-monotonic dependence of D on ϕ for both very ordered $\sigma_d/b = 0$ gels and disordered $\sigma_d/b = 0.9$ gels in fig. 3.6a, due to increasing the interaction range relative to the mesh size k/b. For ordered gels with attractive interactions in figs. 3.5b and 3.6b lowering the ionic strength causes a severe reduction in the particle mobility for small volume fractions. For disordered gels with attractive interactions, $\sigma_d/b \geq 0.5$, the diffusivity also decreases significantly for intermediate volume fractions. Thus, both vertex trapping and dense-region trapping become more pronounced for lower ionic strengths.

Comparison to experimental data for charged and neutral dextran gels

In order to quantitatively test our model predictions we compare to previously published experimental data for the diffusion of Alexa488 molecules in dextran hydrogels that were obtained by fluorescence correlation spectroscopy methods [54]. Alexa488 has a net negative charge and neutral dextran (dextran(o)), positively charged DEAE-dextran (dextran(+)) and negatively charged CM-dextran (dextran(-)) gels have been studied. Here, we compare the experimental data for the diffusivity of Alexa488 under varying dextran mass concentrations to our simulations including spatial disorder. The following model parameters are dictated by the experiment: the particle diameter is 1.48nm [54] and the polymer chain diameter is 0.74nm [30], hence we obtain a size ratio $a/p = 0.5$. Using the partial specific volume $\nu_s = 0.61$ mL/g [30] for dextran, we calculate the fiber volume fraction from the polymer concentration C_{poly} in wt% as $\phi = C_{\mathrm{poly}} \times 0.0061$ from which we derive the gel mesh size b via eq. (3.10) i.e. we assume completely straight polymer fibers and do not allow for polymer crumpling. To calculate the electrostatic interaction range k using eq. (3.9), one has to note that the experiments were performed in buffer solution with an ion concentration of 10 mM. Furthermore, one has to take into account the ionic strength of the counterions that enter the solution upon addition of dextran(-) and dextran(+), which effectively renders the interaction range k dependent on ϕ. Increasing ϕ by 0.01 corresponds to an increase in ion concentration by approximately 3.7mM and 6.1mM for dextran(-) and dextran(+), respectively [54]. We use the interaction potential strength U_0 as a fit parameter, but constrain the ratio of the potential strength for dextran(+) and dextran(-) to be equal to the dextran charge ratio, which is 5/3 [54]. Figure 3.10a shows a comparison of experimental data (unconnected symbols) and simulation data (filled, connected symbols) for disordered $\sigma_d/b = 0.9$ gels with a neutral, an attractive and a repulsive interaction potential, $U_0 = 0$, $U_0/k_BT = -8$ and $U_0/k_BT = 4.8$, respectively. The simulation and experimental data show similar trends. For the attractive case, that means negative Alexa488 in positive dextran(+), the diffusivities increase with the fiber volume fraction ϕ. This at first sight surprising result can be rationalized by the fact that the salt concentration increases with rising ϕ and thus the electrostatic interaction range goes down as ϕ goes up. For the repulsive case of Alexa488 in negative dextran(-) the diffusivities decrease with ϕ, but the simulation diffusivities are significantly lower than the experimental data. The simulation data for the neutral case show a significantly higher diffusivity than for the repulsive case. This stands in contrast to the experimental data for Alexa488 in neutral dextran20(o) (20 kDa molecular weight) and neutral dextran500(o) (500 kDa), that show similar D/D_0 as for the repulsive dextran(-) case, indicating that in the experiment the effect of repulsive charges is significantly weaker than in our simulation model. This could be due to fiber flexibility, which is neglected in our simulation model, as will be discussed further below.

In the comparison between experimental and simulation data for an ordered $\sigma_d = 0$ gel in fig. 3.10b, the simulation data significantly deviates from the experimental data for the attractive case. We conclude that our disordered gel model describes the experimental situation better than an ordered cubic lattice model, in accordance to the fact that neutral dextran gels form disordered polymer networks [7, 28]. Note that we use the fitted interaction potential strengths of $U_0/k_BT = -12$ and $U_0/k_BT = 7.2$ in fig. 3.10b. A plot using parameters $U_0/k_BT = -8$ and $U_0/k_BT = 4.8$ like in fig. 3.10a for the ordered gel with $\sigma_d = 0$ is shown in the supplementary information in fig. 3.12. In our previous paper [54], we obtained qualitative agreement between simulations for an ordered gel model with $\sigma_d = 0$ and experimental data for Alexa488 diffusion in dextran(+) and dextran(-) as a function of added salt at a low fiber volume fraction of $\phi = 0.006$ (C_{poly} =1wt%). In that comparison the agreement between simulation and experiment was particularly good for intermediate to large salt concentrations, but for small salt concentrations, our ordered model underestimated the diffusivity. This is in agreement with our results in fig. 3.10b, where it is seen that the ordered model significantly underestimates the diffusivity for $\phi = 0.006$ in charged gel.

There are a number of potential reasons for the deviations between the experimental data and our model results in fig. 3.10a. First, our model might overestimate the strength of repulsive electrostatic interactions, since we approximate the discrete charges along the dextran polymers by a constant line charge density. The 1.48nm-sized Alexa488 molecules might be able to avoid the discrete repulsive charges on a dextran(-) polymer rather effectively, as their spacing is on average five times the dextran monomer width $5 \times 0.4\text{nm} = 2\text{nm}$ [30]; in this estimate we used the fact that only about one in five dextran monomers carries a charged carboxyl group [54]. Secondly, dextran polymers are rather flexible [28] and, thus, are in principle able to move away from a similarly charged particle and towards an oppositely charged particle, which would effectively weaken the electrostatic repulsion in the experiment and, conversely, increase the electrostatic attraction. Polymer flexibility will also tend to increase the effective mesh size b due to polymer crumpling. Thirdly, the increasing concentrations of dextran(+) and dextran(-) might change the pH of the gel solution enough to influence the number of charged amino and carboxyl

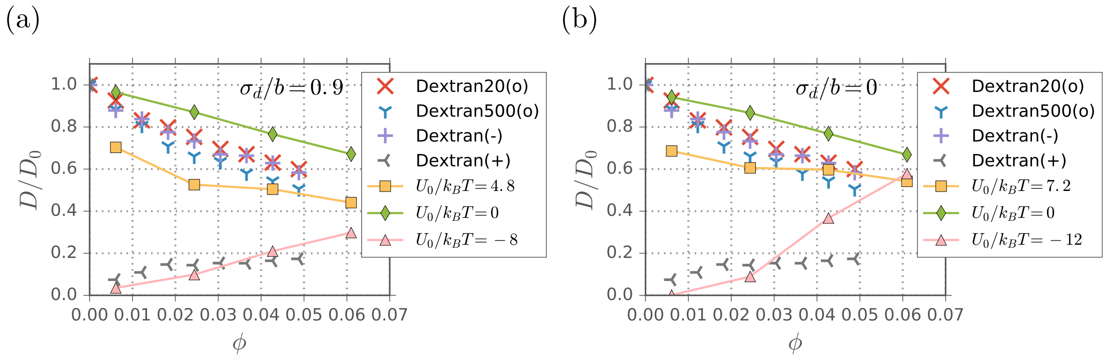

Figure 3.10. Comparison of particle diffusivity as a function of the fiber volume fraction ϕ from simulations for interacting gels (filled connected symbols) with experimental data for Alexa488 diffusion in different dextran hydrogels (unconnected symbols). The simulations use a fiber/particle diameter ratio $a/p = 0.5$ and a disorder strength of (a) $\sigma_d/b = 0.9$ and (b) $\sigma_d = 0$. The interaction range k is dictated by the experimental ionic strength as described in the text. The experimental data was obtained by fluorescence correlation spectroscopy in 10 mM buffer solution with a free solution diffusivity of $D_0 = 320\mu\text{m/s}^2$ [54]. We find qualitative agreement between simulations and experimental data for $\sigma_d/b = 0.9$ in (a). For $\sigma_d = 0$ in (b), the experimental and simulation data for attractive fibers disagree qualitatively.

groups on the dextran(+) and dextran(-) polymers, according to their respective pK_a and pK_b values. Finally, the Alexa488 molecule has an inhomogeneous charge distribution with three negative charges and one positive charge, which might affect its diffusivity in charged gels [23]. Hence, it is likely that the electrostatic interaction between the polymer chains and an Alexa488 particle is more complex than we capture with our simplified interaction potential eq. (3.8). Nevertheless, we find that our approximative, coarse-grained interacting gel model qualitatively reproduces the basic experimental trends.

3.5. Conclusion

We present a model to investigate the trapping mechanisms of nanoparticles in spatially disordered gels with attractive or repulsive nonsteric particle-gel interactions. By changing the disorder strength σ_d we generate ordered as well disordered gels. We find that particles that are attracted to gel fibers are generally more strongly trapped in spatially disordered than in ordered gels. We observe three distinct trapping mechanisms. In gels with repulsive nonsteric interactions particle diffusion is hindered through exclusion trapping. The particle is confined to regions with small local fiber density and an optimal trapping capacity is achieved for an intermediate degree of disorder (c.f. figs. 3.5a and 3.6a), since the particle can cross between cells in an almost unhindered fashion for low σ_d as well as for high σ_d. Diffusion in gels with repulsive nonsteric interactions is similar to diffusion in purely steric gels, which also achieve an optimal trapping capacity for an intermediate degree of disorder (c.f. fig. 3.3). For gels with attractive nonsteric interactions, disorder influences particle diffusion much more severely than for gels with repulsive interactions, and we find two distinct trapping mechanisms for ordered and disordered gels (c.f. fig. 3.9). In ordered gels, vertex trapping occurs, which is most effective for small fiber volume fractions. Thus, diffusion in ordered gels with attractive nonsteric interactions exhibits a peculiar non-monotonic dependence on ϕ (c.f. figs. 3.5b and 3.6b). Even a small degree of spatial disorder eliminates these non-monotonic effects, so to see them in experiments one would need spatially ordered gel structures as can be produced by DNA origami techniques [78]. In disordered gels with attractive nonsteric interactions we find dense-region trapping, which is the most effective immobilization mechanism. Here the particle is trapped in regions of high local fiber density, i.e. near several proximate fibers which create a deep valley in the potential landscape. A similar mechanism has previously been suggested on the basis of experimental data for the ECM [11] and mucus [16]. Numerous experimental results show that gels with attractive nonsteric particle-gel interactions filter nanoparticles much more effectively than gels with repulsive nonsteric particle-gel interactions [17,18,22,23,54]. We argue that this is due to the dense-region trapping mechanism, since we expect considerable spatial disorder in polymer gels [8,9,15,28,46,72,73].

Reducing the ion concentration by about an order of magnitude, i.e. increasing the electrostatic interaction range k by a factor of three between fig. 3.5 and fig. 3.6, severely enhances the effect of dense-region trapping in disordered gels with attractive electrostatic interactions, which makes the ionic strength a useful parameter to regulate charged particle mobility in charged gels [14, 21, 23, 54]. More systematic experimental research on the effects of ionic strength on diffusion in electrostatically interacting gels would be desirable.

We neglect the effect of polymer flexibility in our simulations. Theoretical research has shown that for purely steric systems, network flexibility increases the particle diffusivity compared to rigid networks, in particular for large particles [41, 79]. In our simulations, the fibers are rigid, but the network is not static for disordered gels and changes as the particle moves through the gel. Flexibility may mitigate the differences between ordered and disordered lattices. For future work, it would be interesting to examine the effect of flexibility for gels with nonsteric particle-gel interactions. Furthermore, we neglect that individual polymer chains have a finite contour length which is a good approximation as long as the contour length is much larger than the gel mesh size, as is the case for most hydrogels.

A great deal of pharmaceutical research is directed towards elucidating the barrier properties of biogels like mucus and the ECM. Our simulations indicate how polymer gels filter interacting particles regarding the sign and strength of their interaction. Attractive, e.g. oppositely charged, particles are immobilized and repulsive particles can rapidly traverse biopolymer layers like the mucus barriers, regardless of the fiber lattice geometry, as long as the particles are smaller than the average mesh size. The highest mobilities for particles in gels are of course achieved for inert particles, i.e. when no nonsteric particle-fiber interactions slow down the particle [21, 24, 34, 47, 49, 68, 69]. These insights can be used for the design of advanced drug delivery techniques with nanoparticle carriers through biogel layers. For example, large particles are considered particularly useful for drug delivery purposes since they are more suitable for drug loading and release than smaller particles [10]. In agreement with previous work [34], our simulations show that large particles with a diameter comparable to the mesh size, which can be on the order of 1µm in biogels [10, 11], are mobile in repulsive disordered gels, even in the presence of strong repulsive nonsteric particle-gel interactions, (c.f. fig. 3.6a) since the particle readily avoids the repulsive fibers. On the other hand, large particles in attractive gels are immobilized due to dense-region trapping. Thus, in order to achieve rapid diffusion of large nanoparticles through a biopolymer barrier they should be electrostatically repulsive towards the fibers, i.e. oppositely charged, or they should be charge neutral and hydrophilic.

3.6. Supplementary Information

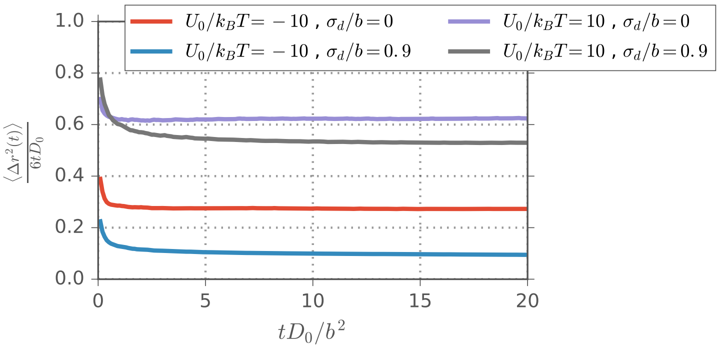

Figure 3.11. Exemplary results for the mean squared displacement divided by time, $\langle \Delta r^2(t)\rangle/6tD_0$, for simulations of spatially ordered and disordered gels with disorder strengths $\sigma_d/b = 0$ and $\sigma_d/b = 0.9$, respectively. The interaction potential is attractive ($U_0/k_BT = -10$) or repulsive ($U_0/k_BT = 10$) and the interaction range is $k/s = 0.5$ with a steric diameter of $s/b = 0.3$. The data reach a constant value in the long-time limit after a displacement of roughly $\langle \Delta r^2(t)\rangle > k^2$ for attractive potentials and $\langle \Delta r^2(t)\rangle > b^2$ for repulsive potentials, which reflects the distance the particle has to travel in order to escape the potential minimum [71]. The simulation time for the trajectory is $t_{\max} D_0/b^2 = 2 \times 10^4$

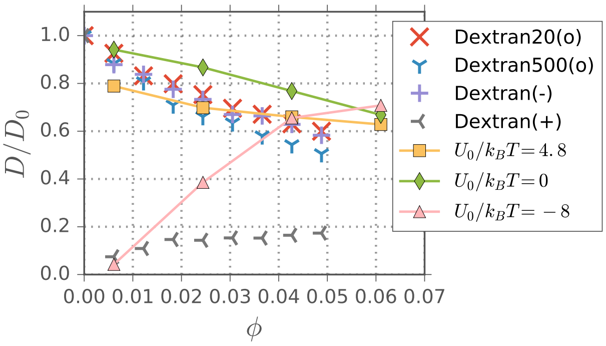

Figure 3.12. Particle diffusivity as a function of the fiber volume fraction ϕ from experiments (unconnected symbols) and simulations with $a/p = 0.5$ and $\sigma_d/b = 0$ (connected, filled symbols) with the same interaction strength parameters used for the disordered system in fig. 3.10a.

4. Diffusion in Polymer Gels with Mixed Attractive and Repulsive Interactions

Bibliographic information: Parts of this chapter have been published in a peer-reviewed journal. Reprinted with permission from Ref. [iv]. Copyright 2018 American Chemical Society.

4.1. Introduction

Biological hydrogels are known to fulfill a number of important physiological functions [1]. Besides regulating the mechanical properties of cells and serving as lubricants in joints, biogels act as barriers against pathogens, thus playing a vital role in protecting organisms. Biological hydrogels, such as mucus and the extracellular matrix (ECM), also serve as selective filters for nutrients, proteins, ions and drugs. Understanding the selective barrier properties of biogels is a research topic where different scientific branches such as physics, chemistry, biology and medicine merge. Alongside volume exclusion and hydrodynamic effects, it has been established that nonsteric interactions, which can be of electrostatic or hydrophobic nature, are a major factor that governs the mobility of particles in biogels [1, 16–20]. Through a combined theoretical and experimental approach, we have previously shown that particle transport in homogeneously charged gels is highly asymmetric [54, 71] in the following sense: Attractive electrostatic interations between particle and gel are much more effective than repulsive interations in hindering particle diffusion. This is due to the sticking of particles at the vertices of the oppositely charged polymer network. However, biopolymers in vivo typically are imhomogeneous and contain different hydrophobic or electrostatically charged monomers that can repel or attract the particle in a single polymer chain. For instance, the mucin protein MUC5AC contains numerous basic and acidic amino acids which can be positively or negatively charged, respectively, according to their pK value and the pH of the solution [14]. Furthermore, many biogels are in fact multicomponent gels, consisting of a mixture of several polymers with different biophysical properties. The ECM, for example, contains the biopolymers laminin and collagen IV with proteins including perlecan and nidogen acting as cross-linker agents [21]. Thus, nanoparticles and macromolecules diffusing in vivo experience a heterogeneous environment with mixed attractive/repulsive interactions, greatly impacting their transport properties. Prior studies showed that biogels such as the ECM [21] and mucus [14, 24] act effectively as an electrostatic bandpass. By this we mean that diffusion of both positively and negatively charged nanoparticles are hindered, while neutral and near neutral charged objects freely diffuse through the matrix. The magnitude of the net charge, not the sign, is the key determinant. To explain this diffusive behavior, Lieleg and coworkers proposed that biogels can be understood as a fiber network of localized positively and negatively charged fiber segments. Charged nanoparticles stick to oppositely charged fiber segments, which strongly reduces their mobility, while neutral particles can diffuse rapidly [14, 21].

In order to investigate this idea systematically, we here present a coarse grained simulation model for nanoparticle diffusion in interacting gels with a random distribution of interaction sites. A spherical particle diffuses inside a network of rigid cylindrical fibers. The fibers consist of segments which are randomly assigned to be attractive or repulsive towards the particle with an exponentially screened interaction potential. Furthermore, we investigate the effect of spatial disorder on the diffusion properties. We expand a previous model for nanoparticle diffusion in interacting gels where either all fibers are purely attractive or all fibers are purely repulsive with the fibers arranged on a cubic symmetric lattice [71]. In this paper, we systematically investigate the combined effects of spatial disorder and interaction disorder, which are both fundamental physical concepts governing diffusion in biological systems. Rigid cylindrical fibers have previously been employed to model the stiff collagen network of the ECM [9, 34] and mucus [71]. Furthermore, recent experimental research indicates that particles experience a rigid fiber network inside mucus gel [8], so a rigid network model presumably is a valid model. Our simulations confirm that in gels with randomly distributed, attractive and repulsive interaction sites, particles are strongly localized near attractive sections of the fiber network. As a consequence, interacting particles are immobilized in gels with mixed attractive and repulsive interactions and the trapping mechanism is closely related to the trapping mechanisms observed in gels with purely attractive electrostatic particle-fiber interactions. In fact, we show that gels with mixed interactions trap particles nearly as effectively as gels with purely attractive interactions.

We compare our simulations to an experimental model system studied by Joseph R. Duke III and Emily B. Fryman under supervision of Prof. Dr. Jason E. DeRouchey at the department of chemistry of the University of Kentucky. As an experimental model system, the translational diffusion coefficients of negatively charged Alexa488 probe molecules in mixed cationic/anionic hydrogels consisting of a mixture of electrostatically positive DEAE-dextran and negative CM-dextran polymer chains is measured by fluorescence correlation spectroscopy (FCS) measurements. Quantitative agreement between simulation and the experiment is found. Both experiment and simulation show that particle transport in mixed gels, over a broad range of compositions, is nearly identical to purely attractive gels despite the reduced number of attractive interaction sites.

4.1.1. Experimental methods

All experiments were conducted by Joseph R. Duke III and Emily B. Fryman under supervision of Prof. Dr. Jason E. DeRouchey.

Materials

Diethylaminoethyl-dextran (DEAE-dextran(+), Mw = 500kDa) and carboxymethyl-dextran (CM-dextran(-), Mw = 15-20kDa) were purchased from Sigma Aldrich. According to the manufacturer dextran(-) has between 1.1 and 1.5 mmol carboxymethyl per gram dextran.

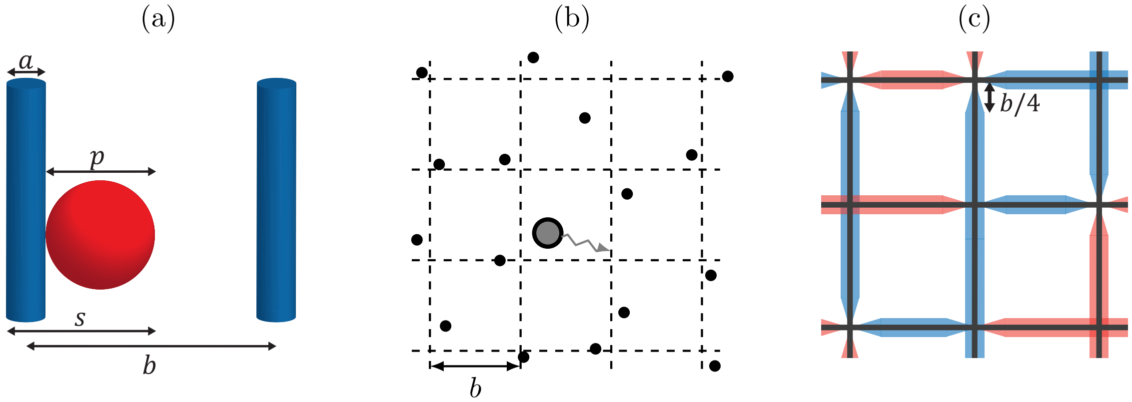

Figure 4.1. (a) Schematics of the simulation model, defining the particle diameter p, the fiber diameter a, the steric diameter $s = a + p$ and the mesh size b. Sketch (b) shows the positions of 16 parallel fibers, indicated as black dots, displaced from a reference cubic lattice with spacing b (dashed lines) by Gaussian random numbers with a standard deviation of $\sigma_d/b = 0.2$ and zero mean. Sketch (c) indicates the sign and strength of the interaction potential, where blue stands for attraction and red stands for repulsion.

The mean value of 1.3 mmol carboxymethyl per gram dextran corresponds to approximately two negative charges per nine monomers. For dextran(+) the nitrogen content is 2.9-3.5%, which corresponds to about one amine group per two monomers for the mean value of 3.2%. Alexa Fluor® 488 Succinimidyl Ester dye (Alexa488, Abs/Em peak: 495/519 nm), and Rhodamine 110 (Abs/Em peaks: 496/520 nm) were purchased from Fisher Scientific. Rhodamine 110 was used in calibration of the confocal volume of the FCS instrumentation. Probe diffusion was performed with Alexa488, which has a net -2 charge at near neutral pH. The fluorescent molecules were readily soluble in water, and did not require further purification prior to use.

Preparation of dextran solutions

Dextran polymer stock solutions were prepared by dissolving solid dextran in 10 mM MES buffer (pH = 6.4) to a final concentration of 8-20 %w/v. Solutions were briefly vortexed and incubated with gentle rocking overnight at room temperature to ensure homogeneity. Subsequent dilutions with MES were made from the stock solutions resulting in the desired final concentrations of polymer solutions. All polymer solutions were allowed to equilibrate for 24 hours before use. For FCS experiments, fluorescent probe molecules (Alexa488 dye) were prepared and mixed with the desired dextran solutions to achieve a final probe concentration of 5-10 nM. Samples were then mixed thoroughly and incubated at room temperature for more than 6 hours to ensure uniform dispersion of the probe molecules throughout the dextran polymer solution. 500 µL of sample from each solution were loaded into NUNC LabTek 8-well microscopy chambers and measured directly by FCS at room temperature. In prior studies, the dextrans were extensively dialyzed to remove salt. Probe diffusion coefficients, as determined by FCS, were within experimental error for dialyzed and non-dialyzed dextrans, suggesting the commercial dextrans used

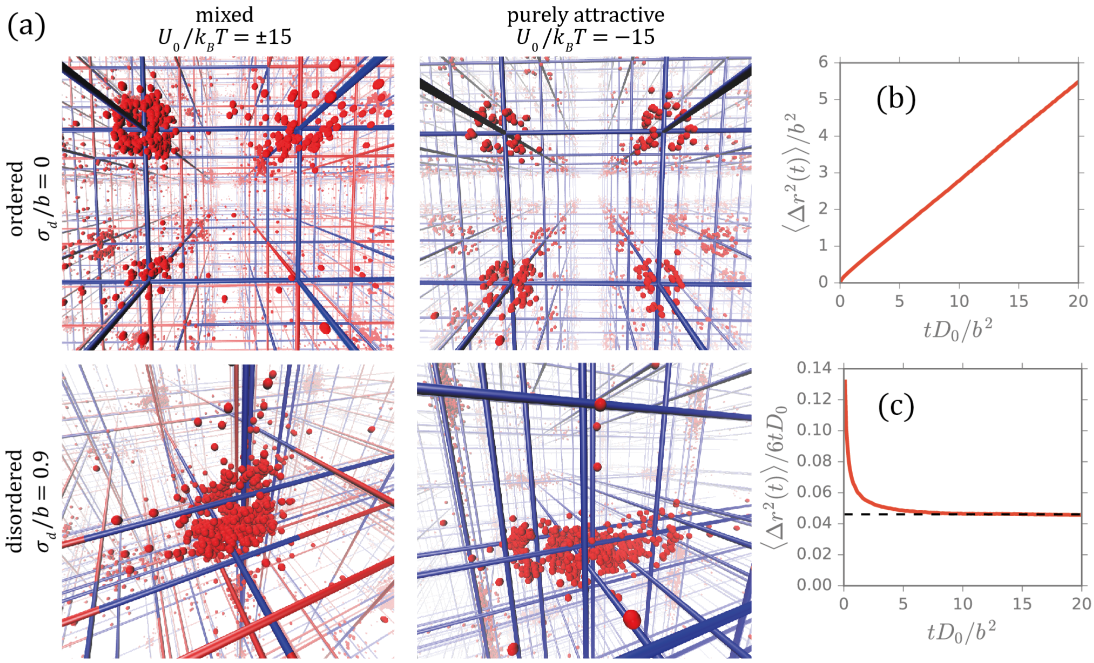

Figure 4.2. (a) Particle position snap shots (red spheres) sampled at consecutive times from simulations of gels with mixed interactions (left) and of gels with purely attractive fibers (right). The sign of the interaction potential along the linear fibers is indicated in red (repulsive) and blue (attractive). Note that in the mixed interaction case, the sign of each fiber segment is randomly chosen with equal probability ($\psi = 0.5$). The top row figures show spatially ordered gels with spatial disorder strength of $\sigma_d = 0$ and the bottom row figures show spatially disordered gels with $\sigma_d/b = 0.9$. The figures demonstrate similar trapping mechanisms for the mixed case (left) and for the purely attractive case (right). For spatially ordered gels (top figures) the particle is trapped at the fiber vertices (*vertex trapping*). In the gel with mixed interactions (top left), the degree of localization differs between the vertices and depends on the number of adjacent attractive fiber segments. In the spatially disordered gels (bottom figures) the particle is trapped in regions of high local fiber density (*dense-region trapping*). All simulations are performed over the same interval of 2×10^9 steps with the same absolute value for the interaction strength $|U_0|/k_BT = 15$, an interaction range of $k/s = 0.5$ and a steric diameter of $s/b = 0.2$. (b) Mean squared displacement (MSD) as a function of time for a mixed gel with $U_0/k_BT = \pm 15$ and $\sigma_d/b = 0.9$ (corresponding to the snap shots at the bottom left in (a)). (c) The MSD divided by time approaches a constant value which corresponds to the long-time diffusivity $D/D_0 = 0.046$ (broken black line). The constant long-time limit is reached after a displacement of roughly $\langle \Delta r^2(t) \rangle > b^2$.

in this study are sufficiently salt free to be used without further purification. For mixed solutions of dextran(+) and dextran(-), stock solutions of each were added together to achieve the desired volumetric ratio of each dextran with respect to total dextran. For all mixed dextran solutions studied, the resulting mixtures resulted in homogeneous polymer solutions.

FCS setup

Fluctuations in fluorescence intensity data were collected using a commercial dual-channel confocal spectrometer (ALBA FFS system, ISS, Champaign, IL). FCS experiments were made using a continuous wave 488 nm laser diode as an excitation source passed through a 514 nm long pass edge filter before detection. Excitation light was directed into experimental samples through a Nikon Ti-U microscope (60x/1.2 NA water-immersion objective lens). The emission signal was recorded by two separate Hamamatsu H7422P-40 photomultiplier tubes (PMTs). Confocal volume dimensions were determined through measurement of aqueous Rhodamine 110 at known concentrations with a diffusion coefficient of $D = 440$ ($\mu\mathrm{m}^2\mathrm{s}^{-1}$) [80]. In order to ensure solution homogeneity, reported results are the average of at least 9 measurements at different positions within the dextran solutions. Sampling times of 30 seconds were used for all measurements. FCS curves were analyzed using the VistaVision Software (ISS, Champaign, IL) to determine the diffusion coefficient.

FCS data analysis

The principles and experimental realization of FCS have been described in detail elsewhere [81–84], here only a brief overview is given. FCS measures the fluorescence fluctuations emitted from labeled molecules moving in and out of a small confocal volume (~1 fL). The size of the effective illumination volume is fixed by the confocal detection optics and the excitation profile of the focused laser beam and characterized by measurements against a standard of known diffusion constant (here Rhodamine 110). The measured time traces of fluorescent events are compared for self-similarity after a lag time τ by calculation of the normalized cross correlation, $G(\tau)$:

$$G(\tau) = 1 + \frac{\langle \delta F(t)\delta F(t+\tau)\rangle}{\langle F(t)\rangle^2} \; . \tag{4.1}$$

$\delta F(t)$ and $\delta F(t+\tau)$ represent deviation from the mean fluorescence $\langle F(t)\rangle$ at time t and after time $t+\tau$. For uniformly distributed fluorescent particles diffusing by Brownian motion, dynamic information can be determined from the intensity fluctuations by means of a time autocorrelation given by:

$$G(\tau) = 1 + \frac{1}{N} \cdot \left(\frac{1}{1+\tau/\tau_D}\right) \cdot \frac{1}{\sqrt{1 + w_0^2\tau/z_0^2\tau_D}} \tag{4.2}$$

where τ_D represents the dwell time of the particles in the confocal volume, whose shape can be approximated as a Gaussian ellipsoid with axial height z_0 and equatorial width w_0 as determined by calibration measurements. N is the average number of particles occupying the observation volume. The normalized autocorrelation can then be calculated by $G_{\mathrm{norm}}(\tau) = G(\tau)/G(0)$. Cross correlation with both detectors ensures that the resulting autocorrelation is free from the effects of detector after-pulsing. The translational diffusion coefficient D ($\mathrm{\mu m^2 s^{-1}}$) can be calculated from τ_D and the equatorial width using

$$\tau_D = w_0^2/4D. \tag{4.3}$$

FCS has been shown previously to be effective for measuring diffusion of probe molecules in polymeric solutions [51, 67, 85].

4.1.2. Simulation methods

The Brownian dynamics simulations are based on the discretized Langevin equation in three dimensions

$$\Delta r_i \;=\; -\,\mu\,\partial_i U(\vec{r}) + \sqrt{2\mu}\,\zeta_i\;, \tag{4.4}$$

where Δr_i is the displacement of the diffusing particle in direction $i = x, y, z$, ∂_i the spatial derivative and ζ a Gaussian distributed random number with zero mean and variance $\langle \zeta_i\,\zeta_j \rangle = \delta_{ij}$, where δ_{ij} is the Kronecker delta. The energy U is rescaled by the thermal energy $k_B T$. The lengths are rescaled by the mesh size b, which is indicated in fig. 4.1a. $\mu = \Delta t\,\mu_0 k_B T/b^2$ is the rescaled timestep, where μ_0 is the bulk sphere mobility. For the simulations a small enough rescaled timestep μ has to be chosen. Different time steps were tested and no increase in accuracy was found for $\mu \leq 10^{-6}$. For the simulations presented in this work, a rescaled timestep μ of 10^{-6} was therefore chosen.

The diffusivity D of the particle is obtained by linearly fitting the mean squared displacement (MSD) $\langle \Delta r^2(t) \rangle = \langle (\vec{r}(t) - \vec{r}(0))^2 \rangle$ in the long-time limit

$$\lim_{t\to\infty} \langle \Delta r^2(t) \rangle \;=\; 6D\,t\;. \tag{4.5}$$

The free diffusion diffusivity, $D_0 = \mu_0 k_B T$, corresponds to the diffusivity of the particle if no polymers are present. For each data point, we simulate a single long particle trajectory of about $\sim 10^9$ steps which is long enough so that the long time limit in eq. (4.5) is reached [71]. Sample repeat simulations have shown that the error for D/D_0 is always below 5%.

Polymer gel model

The polymer gel consists of 48 fibers; 16 fibers parallel to each axis x, y and z. Our model contains both interaction as well as spatial disorder. In recent work we have explored the effects of spatial fiber disorder on nanoparticle diffusion in the absence of interaction disorder (Ref. [ii]). We introduce spatial disorder by displacing the fibers from their positions on a reference cubic lattice with spacing b. The displacement of each fiber is a random vector orthogonal to the fiber axis, sampled from a Gaussian distribution with zero mean and standard deviation σ_d. A high standard deviation σ_d corresponds to increased spatial disorder. Thus, σ_d is henceforth referred to as the spatial disorder strength. Figure 4.1b shows a 2D projection of a weakly spatially disordered gel for $\sigma_d/b = 0.2$. When the particle leaves the central cell of the reference cubic lattice (dashed lines), the eight distal fibers are removed and eight new fibers are added at random positions on the side to which the particle has moved. Thus, the lattice changes as the particle moves across cells but the average mesh size b is conserved.

The steric interaction between the fibers and the particle is governed by a purely repulsive truncated shifted Lennard-Jones potential

$$U(\vec{r}) = \sum_{n=1}^{48} \begin{cases} 4\epsilon \left[\left(\frac{s}{2\rho_n} \right)^{12} - \left(\frac{s}{2\rho_n} \right)^{6} + \frac{1}{4} \right], & \rho_n \leq 2^{-5/6} s \\ 0\,, & \rho_n > 2^{-5/6} s\,, \end{cases} \tag{4.6}$$

where the energy depth is fixed at $\epsilon = 1\, k_B T$, ρ_n is the closest distance between the particle and the nth fiber. The steric diameter s is the sum of the fiber diameter and the particle diameter, $s = a + p$, as illustrated in fig. 4.1a.

To include interaction disorder, we randomly assign an attractive or a repulsive interaction strength, $U_- < 0$ and $U_+ > 0$, to fiber segments with a length of b along each fiber. The long-range, nonsteric interaction between the particle and fiber segments is defined as

$$U(\vec{r}) = U_\pm \exp\left(-\frac{\rho}{k} \right) . \tag{4.7}$$

Here, ρ is the radial distance between the particle and the fiber and k is the interaction range. To avoid discontinuities in the potential the particle experiences, the potential strength goes linearly to zero over a range of $b/4$, if two neighboring fiber segments have an interaction strength of opposite sign, as indicated in fig. 4.1c. The probability for an interaction site to be repulsive is ψ. $\psi = 1$ corresponds to a gel with purely repulsive particle-fiber interactions. For $\psi = 0.5$ both signs for the interaction potential are equally likely. Thus, if additionally the interaction strengths are the same, $U_+ = -U_- = U_0$, the gel is effectively net neutral. Renderings of model gels are presented in fig. 4.2a. The top figures show spatially ordered, cubic gels with $\sigma_d = 0$ and the bottom figures depict spatially disordered gels with $\sigma_d/b = 0.9$. The gels on the left are mixed gels ($\psi = 0.5$), whereas on the right, gels with purely attractive tracer-fiber interactions are shown ($\psi = 0$).

Equation (4.7) is a general nonsteric interaction potential that describes exponentially screened particle-gel interactions. For electrostatic interactions, $U_\pm$ can be interpreted as the product of the particle charge and the linear polymer charge density [71]. In this case, the interaction range k corresponds to the Debye screening length [55]

$$k^2 = \frac{1}{4\pi l_B I}\,, \tag{4.8}$$

where $l_B = e^2/4\pi\varepsilon k_B T$ is the Bjerrum length, e is the elementary charge and ε the permittivity. $I = \frac{1}{2}\sum_j n_j\, z_j^2$ is the ionic strength and z_j the valence of salt ion j and n_j its number density. The salt number density n is related to the molar ion concentration through $C_{\mathrm{Ion}} = n/N_A$, where N_A is the Avogadro constant. Following our previous work on particle diffusion in interacting gels [54, 71] we neglect hydrodynamic interactions.

4.2. Results and Discussion

We first present general simulation results for the diffusion of particles in mixed gels in comparison to diffusion in gels with purely attractive and gels with purely repulsive long-range particle-fiber interactions. First, we assume for the mixed case that the interaction strengths are equal and given by $U_+ = -U_- = U_0$ and $\psi = 0.5$, i.e. the mixed gels are effectively net neutral. Subsequently, we compare simulation and experiment for the diffusion of charged Alexa488 particles in dextran gels containing mixtures of cationic and anionic polymers. Here, U_+, U_- and ψ are dictated by the experiment. To demonstrate how the diffusivities for our simulations are obtained from the MSD in the long-time limit, exemplary MSD plots are shown in figs. 4.2b and 4.2c. It is seen that the long-time diffusive limit is reached when the MSD exceeds the squared lattice constant b^2.

Mixed gels are similar to gels with purely attractive electrostatic interactions

Figure 4.3 shows the relative diffusivity D/D_0 as a function of the interaction potential strength U_0 for different steric diameters $s/b = 0.1, 0.2$ and 0.5 and a rescaled interaction range of $k/s = 0.5$. We present data for spatially disordered and ordered gels with spatial disorder strengths of $\sigma_d/b = 0.9$ and 0, respectively, in figs. 4.3a and 4.3b. The data for the mixed gels (colored, filled symbols) is, by design of our model, symmetric around $U_0 = 0$. One can see that mixed gels trap particles more strongly with rising particle-fiber interaction strength U_0, regardless of the sign of U_0. This "bandpass" like behavior is qualitatively similar to what has been previously reported for the diffusion of charged nanoparticles in the ECM [21] and in mucus [14, 24].

The data indicated by open symbols, connected with dashed lines in figs. 4.3a and 4.3b, correspond to simulations with purely attractive (for $U_0 < 0$) or purely repulsive (for $U_0 > 0$) electrostatic interactions. For $U_0 > 0$, the diffusivities are much higher than for mixed gels. In contrast, for $U_0 < 0$ the data curves for purely attractive gels agree qualitatively with the data for mixed gels, for the disordered system in fig. 4.3a nearly quantitatively. An exception is the $s/b = 0.5$ case for a spatially ordered gel in fig. 4.3b. This is due to the peculiarities of the trapping mechanism in ordered gels with purely attractive electrostatic interactions and will be discussed in the next section. The similarity between D for gels with purely attractive electrostatic interactions and mixed gels is an indicator that both gel types give rise to similar particle trapping mechanisms. The simulation snap shots in fig. 4.2a illustrate which mechanisms govern particle trapping in mixed gels for a spatially ordered gel ($\sigma_d = 0$, top left) and a spatially disordered gel ($\sigma_d/b = 0.9$, bottom left). For each case in fig. 4.2a, the snap shots are obtained at consecutive times from a single particle trajectory. For spatially ordered mixed gels, the particle tends to stay near the attractive vertices of the cubic fiber lattice. For disordered mixed gels, the particle is strongly localized in regions with a high density of attractive fiber segments. Similar trapping mechanisms are observed in purely attractive gels in fig. 4.2a on the right hand side. This indicates that mixed gels and attractive gels both immobilize particles in a similar fashion.

The strong similarity between the trapping mechanisms for mixed and purely attractive gels can be quantified by calculating the average number of fibers $\langle N_{\text{local}} \rangle$ at a radial distance of less than $b/2$ from the particle. The magnitude of $\langle N_{\mathrm{local}} \rangle$ serves as a measure for the particle-fiber correlations and thus for the trapping mechanisms in different gels. Figure 4.4 shows $\langle N_{\mathrm{local}} \rangle$ as a function of U_0 for a steric diameter $s/b = 0.5$ for mixed gels, as well as for gels with purely attractive and gels with purely repulsive electrostatic interactions, for comparison. For the attractive case (fig. 4.4b) $\langle N_{\mathrm{local}} \rangle$ increases with increasing interaction strength, since the particle tends to stay closer to the attractive fibers. For ordered gels, $\sigma_d = 0$, the maximum value of $\langle N_{\mathrm{local}} \rangle$ is 3, which corresponds to the case where the particle is highly localized at the fiber vertices (c.f. fig. 4.2a top right), which we refer to as vertex trapping. With increasing spatial disorder, $\langle N_{\mathrm{local}} \rangle$ increases monotonically. This illustrates that for disordered gels, the particle tends to be trapped in regions of high local fiber density (c.f. fig. 4.2a bottom right), which we refer to as dense-region trapping. Comparing $\langle N_{\mathrm{local}} \rangle$ for gels with purely attractive electrostatic interactions, fig. 4.4b, to $\langle N_{\mathrm{local}} \rangle$ for mixed gels, fig. 4.4a, one sees that both gel types exhibit the same trapping mechanism, in accordance to our qualitative observations in fig. 4.2a. This explains the strong qualitative similarity between D for the mixed case and the attractive case in fig. 4.3. Dense-region trapping and vertex trapping are illustrated schematically for mixed gels in fig. 4.5. For gels with purely repulsive electrostatic interactions (fig. 4.4c), by contrast, $\langle N_{\mathrm{local}} \rangle$ decreases monotonically for all σ_d. The particle moves away from the fibers, into regions with low local fiber density.

We find that mixed gels and gels with purely attractive interactions exhibit similar microscopic trapping mechanisms. The trapping effectiveness for both types of gel is very similar for disordered fiber networks. Nanoparticle diffusion is known to be strongly hindered in gels with purely attractive electrostatic particle-gel interactions [23, 36, 54, 60, 71]; our simulation results indicate that nanoparticles are similarly immobilized in the presence of mixed attractive and repulsive electrostatic interactions of equal magnitude. This makes gels with mixed attractive and repulsive interactions very good particle filters since they filter out particles of positive and negative charge, as further discussed below.

Interaction and spatial disorder have a similar effect on particle diffusion

We next examine the effect of the spatial disorder strength σ_d on D for simulations with and without interaction disorder. Figure 4.6 shows D as a function of σ_d for an absolute interaction potential strength of $|U_0|/k_BT = 10$ and an interaction range of $k/s = 0.5$. Figure 4.6a shows data for a small steric diameter $s/b = 0.1$ and fig. 4.6b for an intermediate steric diameter $s/b = 0.5$. For the attractive case, the diffusivity varies strongly with respect to σ_d. This can be explained as follows: For purely attractive fibers the vertex trapping mechanism is strong for small interaction potential ranges $k \ll b$, when the vertices form strong, localized potential minima [71]. This is reflected in fig. 4.6a, where for a small $k/b = 0.05$, strong vertex trapping leads to small D for $\sigma_d = 0$. For intermediate to large $k \sim b$, by contrast, vertex trapping is weak for purely attractive gels, since the interaction potentials of neighboring fibers balance each other due to the ordered spatial alignment of the fibers [71]. Thus, in fig. 4.6b, an intermediate $k/b = 0.25$ leads to high diffusivities at $\sigma_d = 0$ and $U_0/k_BT = -10$. Also, in fig. 4.3b for $U_0 < 0$ and the largest steric diameter $s/b = 0.5$, weak vertex trapping causes significantly higher diffusivities for the purely attractive case, compared to the mixed case. More information on this can be

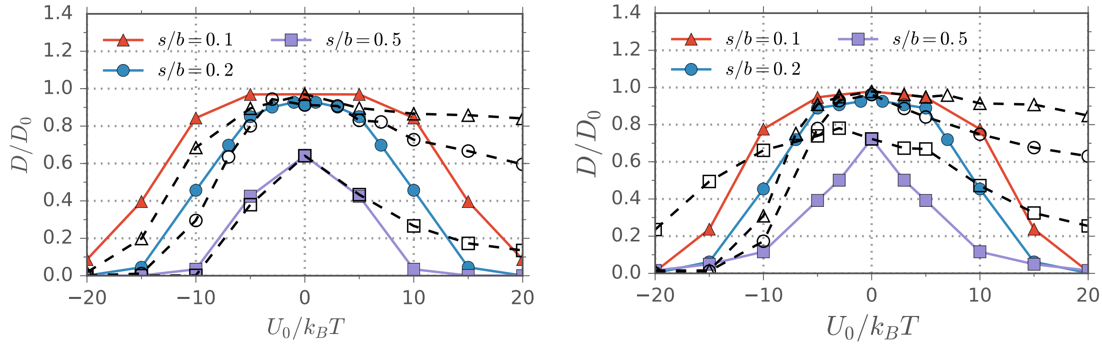

(a) $\sigma_d/b = 0.9$

(b) $\sigma_d = 0$

Figure 4.3. Particle diffusivity D as a function of the interaction potential strength U_0 for different steric diameters s for a rescaled interaction range of $k/s = 0.5$, $U_+ = -U_- = U_0$ and $\psi = 0.5$. (a) D for spatially disordered gels with $\sigma_d/b = 0.9$ and (b) D for ordered gels with $\sigma_d = 0$. Except for the $s/b = 0.5$ curve in (b), the diffusive behavior for mixed gels (colored symbols) and for gels with purely attractive electrostatic interactions ($U_0 < 0$, empty symbols) is qualitatively very similar, whereas gels with purely repulsive electrostatic interactions ($U_0 > 0$, empty symbols) differ strongly from the mixed case.

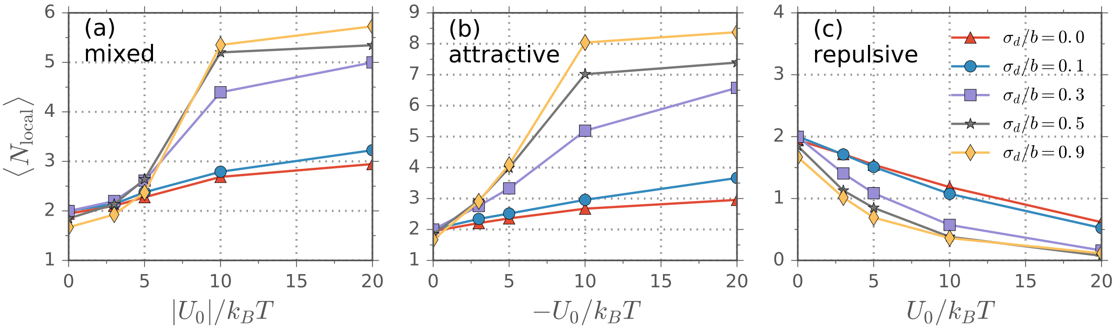

Figure 4.4. The average number of fibers $\langle N_{\mathrm{local}} \rangle$ at a radial distance of less than $b/2$ from the particle as a function of the interaction potential strength for particles of diameter $s/b = 0.5$ and a rescaled interaction range of $k/s = 0.5$ for (a) mixed interactions with $U_+ = -U_- = U_0$ and $\psi = 0.5$, (b) purely attractive electrostatic interactions with $U_0 < 0$ and (c) purely repulsive electrostatic interactions with $U_0 > 0$. The data for the mixed case resembles closely the data for the attractive case.

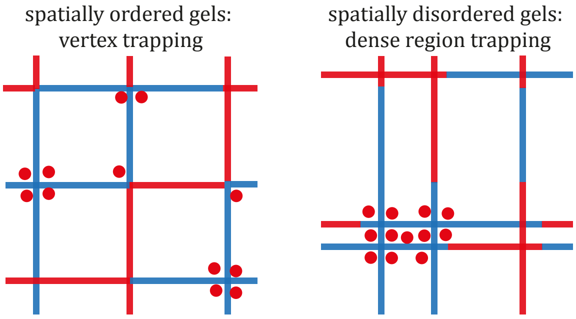

Figure 4.5. Schematic illustrations of the different particle trapping mechanisms for mixed gels: *Vertex trapping* for spatially ordered gels and *dense-region trapping* for spatially disordered gels. The color of the fiber segments indicates whether they are repulsive (red) or attractive (blue).

found in [71] and in the supplementary information in fig. 4.9, which shows the particle diffusivity as a function of the interaction potential range k/b without steric effects, i.e. for $s = 0$, in order to illustrate the effect of the interaction range in comparison to the mesh size b.

Comparison of the mixed and attractive cases in fig. 4.6a shows that for small interaction ranges k/b vertex trapping for ordered gels ($\sigma_d = 0$) becomes weaker when random interaction sites are introduced, resulting in an increased D. We attribute this to the fact that there are fewer and irregularly spaced strong potential minima at the fiber vertices as depicted in fig. 4.2a, top row. For intermediate k/b in fig. 4.6b, on the other hand, vertex trapping becomes much stronger when random interaction sites are introduced, since the irregularly spaced strong potential minima do not balance each other like they do in a purely attractive ordered gel. Thus, introducing interaction disorder via randomly mixed attractive and repulsive interaction sites into the model system mitigates the strong effect of the spatial disorder strength σ_d on the diffusive behavior in figs. 4.6a and 4.6b. In fact, interaction disorder and spatial disorder both randomize the potential landscape in the gel and therefore have a qualitatively similar effect on D. This is underlined in fig. 4.10 in the supplementary information, where we compare the diffusivity as function of U_0 for simulations with no disorder, only spatial disorder, only interaction disorder and both spatial and interaction disorder.

Mixed gels are strong particle filters

The concept of interaction filtering describes the selective immobilization of particles according to their interaction with the fibers in biogels like mucus and the ECM [1]. For the case of electrostatic interactions, the potential strength U_0 can be interpreted as the product of the particle charge and the linear fiber charge density [71]. Thus, according to fig. 4.3, gels with mixed electrostatically positive and negative interaction sites are very effective filters for charged particles, as they can immobilize strongly charged particles of either sign. By contrast, if the gel fibers contain, for example, only negative charges, positively charged particles may be immobilized due to vertex trapping or dense-region

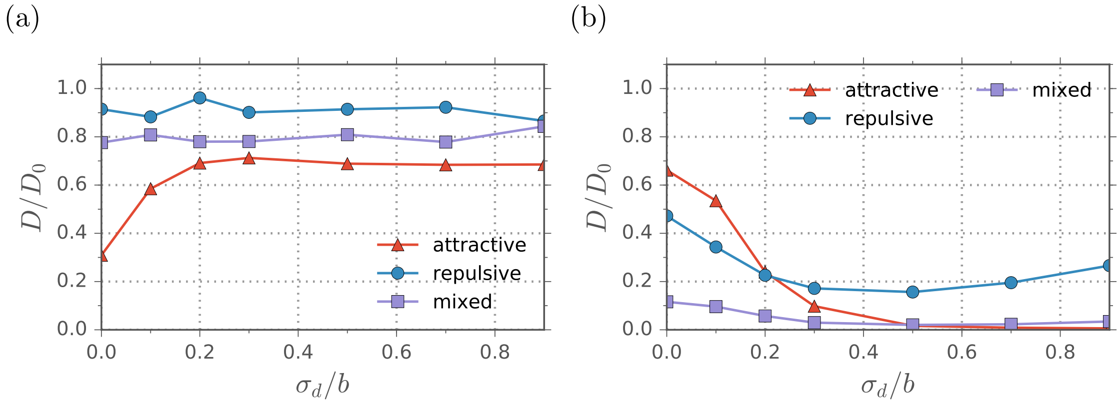

Figure 4.6. Particle diffusivity as a function of the spatial disorder strength σ_d for a rescaled interaction range of $k/s = 0.5$ in purely attractive ($U_0/k_BT = -10$) and purely repulsive ($U_0/k_BT = 10$) gels and mixed gels, $U_+ = -U_- = 10k_BT$ and $\psi = 0.5$. For (a) we employ a small steric diameter $s/b = 0.1$, which corresponds to a small interaction range $k/b = 0.05$ and for (b) a large steric diameter $s/b = 0.5$, corresponding to an intermediate $k/b = 0.25$. The effect of spatial disorder on the diffusivity is drastically reduced for mixed gels, compared to gels with purely attractive electrostatic interactions.

trapping (c.f. fig. 4.5), but negatively charged particles will be very mobile inside the gel, since purely repulsive electrostatic interactions lead to comparably weak particle trapping with relative diffusivities of $D/D_0 > 0.1$ compared to $D/D_0 \ll 0.1$ for strongly attractive $U_0/k_BT = -20$ as seen in fig. 4.3.

Furthermore, as shown in fig. 4.6, particle trapping in mixed gels depends only weakly on spatial disorder. Thus, our simulations illustrate why heterogeneous biogels with mixed interaction sites serve as highly effective, natural filters for interacting particles, whereas purely attractive gels exhibit a strong dependence on σ_d. The strong particle trapping capabilities of gels with mixed positive and negative interaction sites are demonstrated experimentally in the next section.

4.3. Comparison of experiments and model predictions

To test our theoretical model, we perform a quantitative comparison of simulation and experimental data. FCS is used to experimentally measure the diffusivity of negatively charged Alexa488 fluorescent particles in gels that are comprised of a mixture of positively charged dextran(+) and negatively charged dextran(-) polymers. Translational diffusion coefficients are obtained for pure dextran(-), pure dextran(+) and mixed dextran solutions for various mixing ratios and different polymer mass concentrations. Characteristic normalized fluorescence autocorrelation functions in pure and mixed dextran solutions are shown in fig. 4.7. In fig. 4.8 we present the relative diffusivity of Alexa488 particles (crosses) for varying mixtures of dextran(+) and dextran(-), defined by the ratio of dextran(-) to the total dextran mass concentration, i.e. $C_{\text{dex}(-)}/C_{\text{total}}$. Experiments shown are performed at total polymer concentrations of $C_{\text{total}} = 4\%$w/v, 6%w/v and 8%w/v in figs. 4.8 a to c, respectively. For $C_{\mathrm{dex}(-)}/C_{\mathrm{total}} = 0$, the electrostatic particle-gel interactions are purely attractive, which leads to strongly reduced diffusivities, compared to free diffusion of Alexa488. For $C_{\mathrm{dex}(-)}/C_{\mathrm{total}} = 1$, i.e. purely repulsive electrostatic particle-gel interactions, Alexa488 exhibits much higher diffusivities than for pure dextran(+), in accordance to our previously published results which showed that gels with purely attractive electrostatic interactions hinder particle diffusion more effectively than gels with purely repulsive electrostatic interactions [54, 71]. As shown in fig. 4.8, mixed dextran gels with $C_{\mathrm{dex}(-)}/C_{\mathrm{total}}$ between 0 and 0.5 show diffusivities nearly identical to purely attractive dextran(+) gels, even though the number of attractive interaction sites in mixed dextran gels is significantly lower than for pure dextran(+). So we observe a highly asymmetric behavior of the diffusivity with respect to the symmetric solution with 50% dextran(+) and 50% dextran(-). This is consistent with our theoretical predictions in fig. 4.3, which showed that mixed gels hinder charged particle diffusion practically as effectively as purely attractive gels. Furthermore, even at $C_{\mathrm{dex}(-)}/C_{\mathrm{total}} = 0.75$ in fig. 4.8 trapping is still strong, i.e. D is still significantly smaller than for 100% dextran(-). This shows that even comparably few attractive interaction sites inside the gel can still significantly hinder the diffusion of interacting particles, thus leading to strong interaction filtering for mixed gels.

In order to compare the experimental data to our theoretical model, we perform simulations using the following model parameters, dictated by the experiment: The probe particle diameter is $p = 1.48$nm [54] and the polymer chain diameter is $a = 0.74$nm [30] which approximates the dextran diameter, hence we obtain a fiber/particle diameter ratio $a/p = 0.5$. The ratio of the potential strengths for the attractive and the repulsive fiber segments, U_-/U_+, is dictated by the experiment and reflects the fact that dextran(+) has approximately one charged amino group per two glucoses, and dextran(-) has approximately two charged carboxyl group per nine glucoses, which leads to a ratio of dextran(+) to dextran(-) line charge densities of $(1/2)/(2/9) = 2.25 = U_-/U_+$. The density of charges on the polymer chains also influences the background ion concentration C_{Ion} of the solution, which determines the interaction range according to eq. (4.8). C_{Ion} increases by about 11 mM and 6 Mm upon addition of 1%w/v dextran(+) and dextran(-) to the solution, respectively. As dextran gels are known to be spatially disordered [7, 28], we use a spatially disordered gel in our simulations with a disorder strength of $\sigma_d/b = 0.9$. The magnitude of ψ for the simulations corresponds to the mixing ratio $C_{\mathrm{dex}(-)}/C_{\mathrm{total}}$. We choose the strength of the interaction potential with fixed ratio $U_-/U_+ = 2.25$ and the mesh size b for optimal agreement between simulation and experiment. The estimation of the optimal values of b and are shown in the supplementary information. As a result, we obtain $U_-/k_BT = -10.1$ and $U_+/k_BT = 4.5$ as well as $b = 11$, 9.0 and 7.8 nm for $C_{\mathrm{total}} =$ 4, 6 and 8%w/v, respectively. The simulation data is presented in fig. 4.8 as filled circles. For 4%w/v and 6%w/v the simulated diffusivities are in close correspondence to the experimentally observed diffusivities over a broad range of dextran ratios. For the highest dextran concentration of 8%w/v in fig. 4.8c, our simulations overestimate the diffusivities but the simulation and experimental curves are still in qualitative agreement. Assuming completely straight fibers, we can calculate b using the formula $C_{\mathrm{total}} \approx (3/l_{\mathrm{dex}}b^2)m_{\mathrm{mon}}$, where $l_{\mathrm{dex}} = 0.39$ nm [86] is the dextran monomer length, $3/l_{\mathrm{dex}}b^2$ the dextran monomer density and $m_{\mathrm{mon}} = 162$ Da the dextran monomer mass. For completely straight dextran

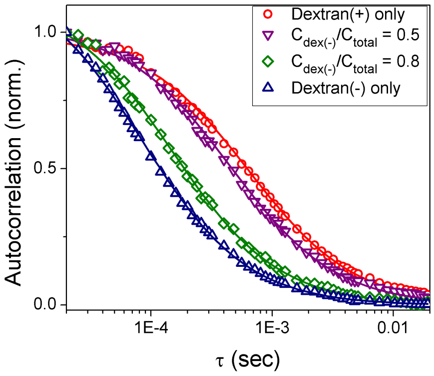

Figure 4.7. Characteristic normalized FCS autocorrelation curves for the diffusion of Alexa488 NHS ester (-2 charge) through a 10 mM MES buffer (pH = 6.4) solution of 6 %w/v total dextran concentration at a few different dextran(-) to dextran(+) concentration ratios $C_{\text{dex}(-)}/C_{\text{total}}$. Experimental autocorrelations (symbols) are fit to eq. (4.2) (solid lines) in order to determine translational diffusion coefficients.

fibers we obtain the substantially reduced mesh sizes of 7.2, 5.9 and 5.1 nm for $C_{\text{total}} =$ 4, 6 and 8%w/v, respectively. This suggests that in experimental dextran gels, the individual dextran polymers are significantly crumpled, which leads to an increase of the mesh size b. A comparison between simulation and experimental data using the mesh sizes for completely straight dextran fibers is shown in fig. 4.12. The agreement between experiment and simulation is still very good, which means that the resultant diffusivities in the simulation model only slightly depend on the precise value of b used.

Note that we also performed simulations for an alternative mixed gel model where entire fibers are randomly assigned to be either purely attractive or purely repulsive, instead of having fiber segments of varying charge sign. Qualitatively, the diffusive behavior for the alternative mixed gel model is the same as for the model used in this paper, as shown in the supplementary material (figs. 4.13 and 4.14).

4.4. Conclusions

In summary, for particle trapping in gels with mixed attractive and repulsive interaction sites, our simulations and experiments demonstrate that attractive interactions primarily determine the diffusive behavior of the particles (c.f. fig. 4.3). As a consequence, the particle trapping mechanisms observed in mixed gels are similar to the trapping mechanisms observed in gels with purely attractive fibers (c.f. figs. 4.2a and 4.4). For gels with spatially disordered fiber networks, dense-region trapping leads to immobilization of the diffusing particle as shown in fig. 4.5 on the right. For spatially ordered gels, particles are trapped at the fiber vertices (c.f. fig. 4.5 left). Previously, we have shown that vertex trapping can be ineffective for purely attractive electrostatic particle-fiber interactions, for intermediate to long interaction potential ranges due to the regular spacing of the potential minima at the vertices which balance each other [71]. This balancing effect

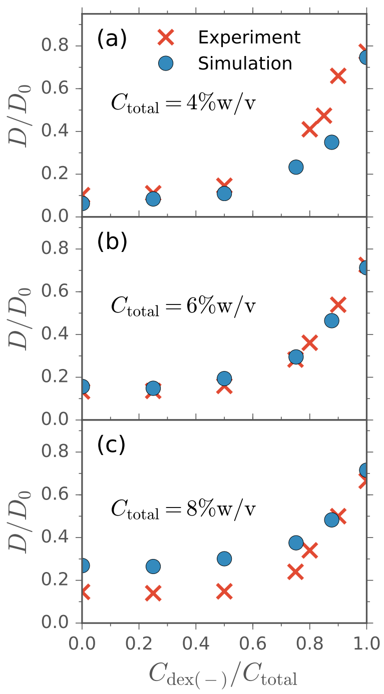

Figure 4.8. The diffusivity for Alexa488 in mixed solutions of oppositely charged dextran(+) and dextran(-) as a function of the dextran(-) to total dextran mass concentration ratio. The total mass concentration of the gel polymers is (a) 4 %w/v, (b) 6 %w/v and (c) 8 %w/v. For the simulations, we use b = 11, 9.0 and 7.8 nm, respectively. We find quantitative agreement between experiments and simulations for 6 %w/v. For 4 %w/v, the simulations and the experiments agree closely for small to intermediate $C_{\text{dex}(-)}/C_{\text{total}}$ concentrations, but some discrepancy is seen for high $C_{\text{dex}(-)}/C_{\text{total}}$ concentrations. Qualitative agreement is found for 8 %w/v.

for vertex trapping is canceled by introducing random interaction sites into the system (c.f. fig. 4.6b). As a consequence, mixed gels immobilize interacting particles regardless of spatial gel disorder and the sign of the particle charge. Lieleg and coworkers experimentally investigated the diffusion of charged nanoparticles in the ECM and found that steric hindrance effects imposed by the detailed structural organization of the ECM play only a minor role for the particle mobility [21]. Furthermore, Lieleg and coworkers found that nanoparticles of either sign are immobilized in the ECM [21] and in mucus [14] due to attractive electrostatic interactions with the gel fibers. Our model not only reproduces and confirms these experimental findings, but also elucidates the details of the microscopic mechanism.

We find that interaction disorder and spatial disorder have a qualitatively similar effect on the diffusive behavior of the particle. This is an interesting finding since for some simulations it may be useful to neglect spatial disorder. For example, for simulations with HI, spatial order allows for efficient computation of hydrodynamic interactions between particle and gel fibers [26]. If disorder is desired, e.g. to simulate biological systems, one could readily introduce interaction disorder using randomly mixed positive and negative interaction sites.

Diffusion experiments for charged Alexa488 fluorescent particles in mixtures of positively charged DEAE-dextran and negatively charged CM-dextran gels corroborate our theoretical findings that gels with mixed attractive and repulsive interactions immobilize interacting particles virtually as effectively as gels with purely attractive electrostatic interactions. Furthermore, we find that particle diffusion is strongly hindered, even if the concentration of attractive polymers inside the gel is significantly smaller than the concentration of repulsive polymers (c.f. fig. 4.8). In other words, even comparably few attractive interaction sites can have a strong trapping effect. For this reason, heterogeneous biopolymer gels consisting of functional groups with different biophysical properties are very efficient filters for interacting particles.

For figs. 4.3 and 4.6 our simulations were performed for neutral gels, i.e. with a balanced number of attractive and repulsive interaction sites ($\psi = 0.5$) of equal absolute strength. This indicates that a charge neutral polymer gel with both positive and negative functional groups can be used to filter out charged particles of either sign. Accordingly, uncharged particles [21, 47, 49, 68, 69] as well as net neutal particles with a high density of positive and negative charges on the surface [13, 23, 68, 87] have been reported to be highly mobile inside biogels. The latter strategy is employed by some viruses [2, 13, 87]. Note that in the present work we used the exponentially screened interaction potential eq. (4.7) to model electrostatic interactions, but an exponentially decaying potential also describes other types of nonsteric interactions such as hydrophobic interactions.

The permeability of nanoparticles through biogels such as mucus and the ECM is relevant for many in vivo processes. Designing nanoparticles which can rapidly overcome the diffusive barriers poses a significant challenge for many pharmaceutical and medical purposes. Our model reproduces a number of experimentally observed phenomena for particle trapping in heterogeneous gels and furthermore elucidates the microscopic particle trapping mechanisms. The knowledge of the microscopic particle trapping mechanisms in heterogeneous gels will be useful for the design of advanced drug delivery techniques.

4.5. Supplementary Information

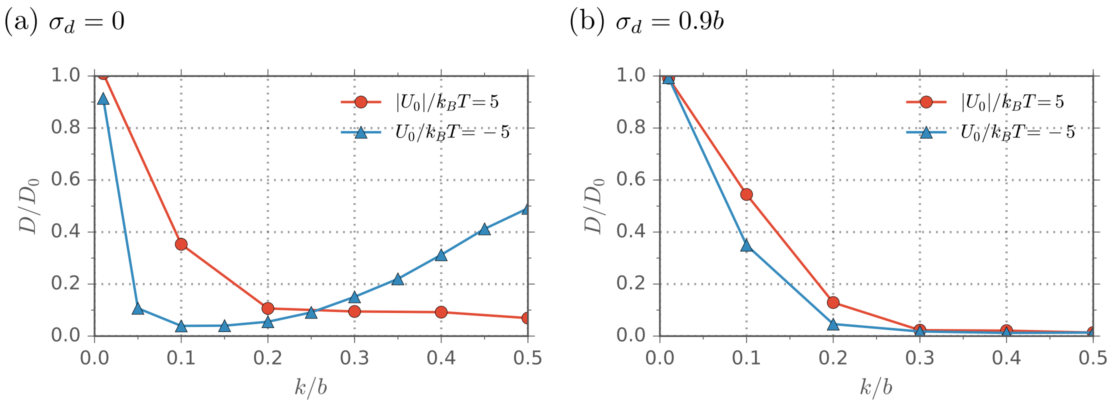
(a) $\sigma_d = 0$ (b) $\sigma_d = 0.9b$

Figure 4.9. Particle diffusivity as a function of the interaction potential range k without steric effects, i.e. for $s = 0$. In (a), the diffusivity for gels with purely attractive electrostatic particle-fiber interactions $U_0/k_BT = -5k_BT$ has a minimum at $k/b \sim 0.1$, beyond which D increases, since the attractive potentials of adjacent fibers start balancing each other as k becomes comparable to b. For ordered mixed gels, $|U_0|/k_BT = 5$, on the other hand, the diffusivity decreases monotonically, due to the random structure of the potential landscape inside the gel. For spatially disordered lattices, presented in (b), we observe very similar monotonic diffusive behavior for mixed and purely attractive gels since the potential landscape is already spatially disordered.

Estimate of optimal simulation parameters

We estimate the optimal parameters b and U_+, where U_- is fixed at $U_- = -2.25U_+$. For this, we calculate the sum of the squared differences between the experimental and the simulated diffusivities

$$\sigma^2 = \sum_{i=1}^{3}\sum_{j=1}^{6}[(D/D_0)_{\text{exp}}(C_{\text{total}}^{(i)}, C_{\text{dex}(-)}^{(j)}) - (D/D_0)_{\text{sim}}(C_{\text{total}}^{(i)}, C_{\text{dex}(-)}^{(j)})]^2/18\,, \tag{4.9}$$

where 6 is the number of data points for each of the 3 total dextran concentrations $C_{\text{total}} =$ 4, 6 and 8%w/v. In total we calculate σ^2 for $3 \times 6 = 18$ data points per U_+ value. The experimental data is linearly interpolated to calculate σ^2. First, we estimate the optimal U_+ by identifying the minimum of σ^2 for different values of b in figs. 4.11a to 4.11c. The mesh sizes for $C_{\text{total}} = 4$ %w/v in figs. 4.11a to 4.11c are 7.2, 11 and 15 nm, respectively. The value $b = 7.2$ nm is the smallest possible value of b and corresponds to a completely straight dextran polymer. For $C_{\text{total}} = 6$ and 8 %w/v, b is calculated with the expression

$$C_{\text{total},1}b_1^2 = C_{\text{total},2}b_2^2\,, \tag{4.10}$$

which follows from the relation between the mesh size b and the polymer concentration $C_{\text{total}} = (3/l_{\text{dex}}b^2)m_{\text{mon}}$. Note that using this expression we assume that the polymer

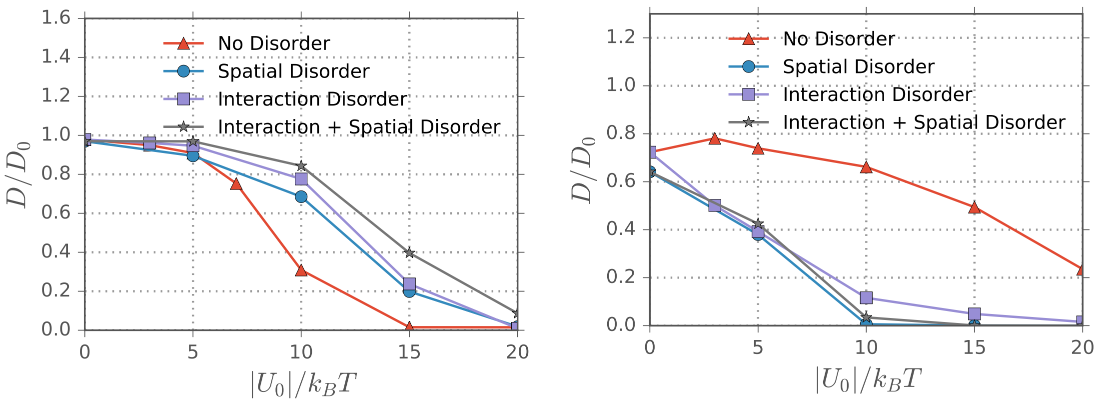
(a) $s/b = 0.1$

(b) $s/b = 0.5$

Figure 4.10. Particle diffusivity as a function of the interaction potential strength U_0 for (a) $s/b = 0.1$ and (b) $s/b = 0.5$. The curves for the ordered gel ($\sigma_d = 0$ and purely attractive $U_0 < 0$) differ significantly from the curves with disorder. Introducing either interaction disorder (mixed gels $\psi = 0.5$ and $-U_- = U_+ = U_0$) or spatial disorder ($\sigma_d/b = 0.9$) has a similar effect on the diffusivity. The curves with no disorder and with spatial disorder correspond to the attractive case $U_0 < 0$.

crumpling and thus the increase of the mesh size b is independent of the total polymer concentration. Next, the minimal σ^2 from figs. 4.11a to 4.11c are compared in fig. 4.11d. The optimal simulation parameters are thus estimated as $b = 11$ nm (for $C_{\text{total}} = 4$), $U_+/k_BT = 4.5$ and $U_-/k_BT = -10.1$, which corresponds to the global minimum of σ^2 with respect to b in fig. 4.11d. Note, that the fiber diameter $a = 0.74$ nm, which was calculated using the partial specific volume of neutral dextran $\nu_s = l_{\text{dex}}\pi a^2 N_A/m_{\text{mon}} = 0.61$ mL/g in reference [30], is not varied for the different mesh sizes in figs. 4.11a to 4.11c.

Alternative mixed gel model

In an alternative version of a gel model with mixed attractive and repulsive interaction sites, each gel fiber is either entirely attractive or entirely repulsive, instead of having attractive and repulsive fiber segments. The two models are shown in fig. 4.13, for comparison. In fig. 4.14 we present simulation data for both models and find that the diffusive behavior is very similar.

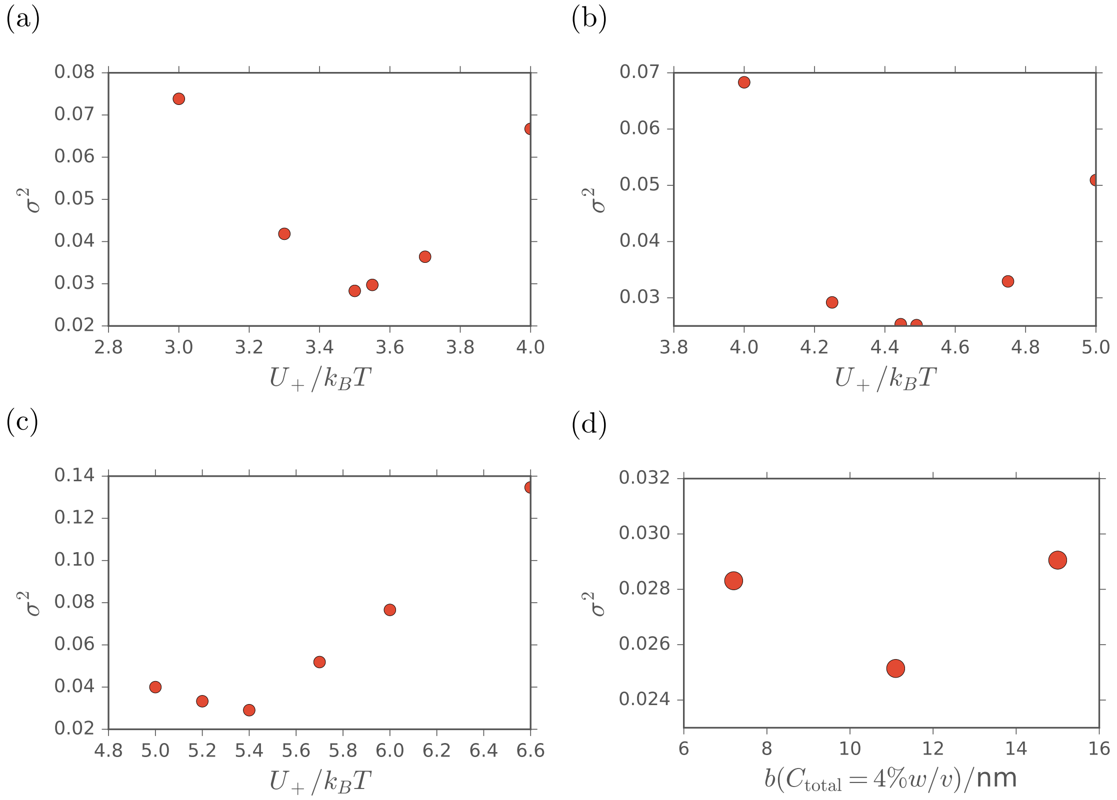

Figure 4.11. Squared residuals (eq. (4.9)) as a function of U_+ for different mesh sizes. For $C_{\text{total}} = 4$ %w/v the mesh size is (a) 7.2 nm, (b) 11 nm and (c) 15 nm. For $C_{\text{total}} = 6$ and 8 %w/v the mesh size follows from eq. (4.10). (d) Squared residuals as a function of $b(C_{\text{total}} = 4$ %w/v) for the respective optimal U_+.

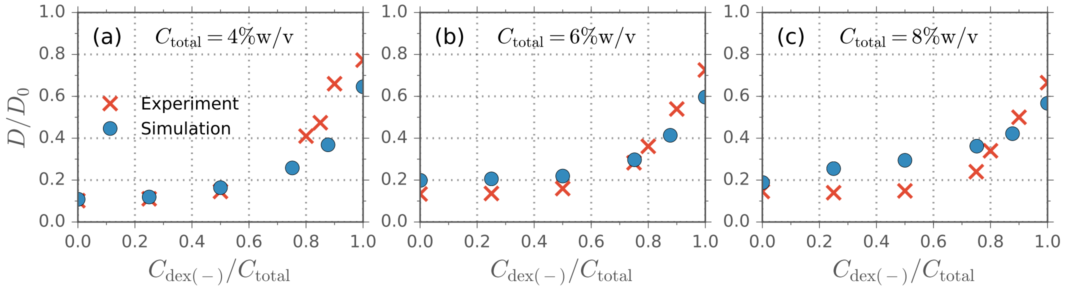

Figure 4.12. The diffusivity for Alexa488 in mixed solutions of oppositely charged dextran(+) and dextran(-) as a function of the dextran(-) to total dextran mass concentration ratio. The total mass concentration of the gel polymers is (a) 4 %w/v, (b) 6 %w/v and (c) 8 %w/v. For the simulations, we use the mesh sizes calculated for completely straight fibers $b = 7.2$, 5.9 and 5.1 nm, respectively, and the optimal potential strengths according to fig. 4.11a, $U_+/k_BT = 3.5$ and $U_-/k_BT = -7.88$. Qualitative agreement is found between the experiments and simulations.

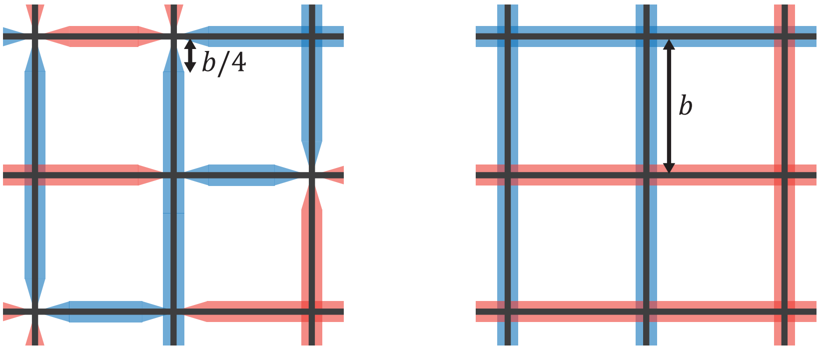

Figure 4.13. The sketch on the left demonstrates the sign and strength of the interaction potential (where blue and red stand for opposite signs) for the gel model used in the paper. On the right, the alternative model is illustrated, where each gel fiber is entirely attractive or repulsive.

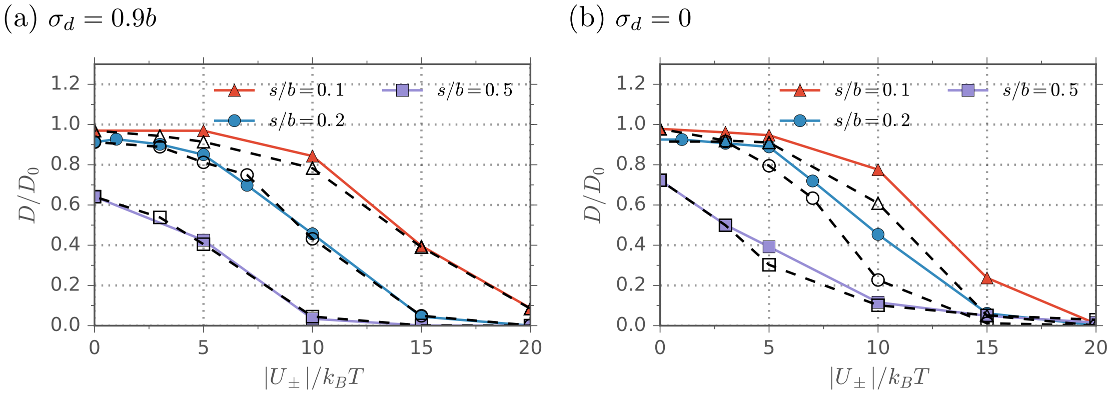

Figure 4.14. Particle diffusivity as a function of the absolute interaction potential strength for different steric parameters s for a rescaled interaction range of $k/s = 0.5$. In (a) spatially disordered and in (b) ordered lattices with $\sigma_d = 0.9b$ and $\sigma_d = 0$ are simulated, respectively. The data for the model for mixed gels used in the paper (colored symbols) and for the alternative mixed gel model for which individual fibers are entirely attractive or repulsive (empty symbols) (c.f. fig. 4.13 left and right, respectively) show very similar diffusive behavior. Similar to what is observed in fig. 4.3, the similarity between the different models is stronger for highly disordered lattices in (a), compared to ordered lattices in (b). For disordered lattices in (a) both versions agree quantitatively. For ordered lattices in (b) the alternative version leads to moderately smaller diffusivities than the version used in the paper, but qualitatively the curves correspond closely. The small deviations can be attributed to the increased number of strong potential minima at the vertices of the lattice, i.e. when all three fibers are attractive, that are present when each fiber has a constant interaction potential strength.

5. Hydrodynamic Effects on Particle Diffusion in Polymeric Hydrogels with Steric and Electrostatic Particle-Gel Interactions

Bibliographic information: Parts of this chapter and of appendices B to G have been published in a peer-reviewed journal. Reproduced with permission from Ref. [v]. Copyright 2018 American Chemical Society.

5.1. Introduction

The diffusive properties of nanoparticles and macromolecules in biogels and synthetic hydrogels is important for many biological and medical applications. For particle diffusion in purely steric gels, that means systems without hydrophobic or electrostatic particle-gel interactions, there exists a large body of theoretical and experimental research which highlights the importance of both hydrodynamic and steric interactions [9, 26, 27, 63, 66, 75, 88]. In recent years, the study of interacting hydrogels, that means gels where in addition to steric particle-gel interactions one also has attractive or repulsive finite-ranged interactions, received growing attention. In interacting gels, particle mobility is regulated via nonsteric interactions such as electrostatics or hydrophobicity, which turn such gels into very effective and often specific particle filters [1,14,21,54,71,89]. In fact, many biogels are interacting gels. Prominent examples are mucus [1, 14, 89], the extracellular matrix [1, 21] or the vitreous humor, a transparent gel in the eye of vertebrates [16, 17]. Many pertinent coarse-grained simulation models exist for particle diffusion in interacting gels [36–38, 60, 90, 91]. In most of these studies, hydrodynamic interactions (HI) are neglected. HI in conjunction with nonsteric particle-gel interactions were previously considered by Stylianopolous and coworkers who studied the diffusive behavior of nanoparticles that interact with the gel fibers via screened, repulsive electrostatic interactions [34]. Their work provides considerable insight into how repulsive electrostatic interactions influence the diffusion of particles in the extracellular matrix but does not consider the effects of hydrodynamic interactions in conjunction with attractive interactions. In other related research, Brownian dynamics simulations with HI have been used to investigate the short-time and long-time diffusive behavior for charged particles in dilute solutions of mobile polyelectrolytes [92].

Here, we employ a coarse-grained simulation model for the diffusion of nanoparticles in interacting, cross-linked polymer gels. The particle diffuses in a cubic lattice of immobile cylindrical fibers which interact with the particle via an exponentially decaying interaction potential that can be either repulsive or attractive. We have previously used a similar gel model to investigate diffusion in interacting gels without HI, and found that nonsteric interactions typically are dominant compared to steric interactions [54,71]. More recently, we studied the effects of spatial disorder of the gel on the particle diffusive properties [93]. Yet, the lack of HI caused significant discrepancies between our simulation results and experimentally observed diffusive behavior, in particular in the limit of weak interactions. In this chapter, we demonstrate that inclusion of HI mitigates the discrepancies between our model and experimental results for purely steric as well as for interacting gels. In particular for gels with electrostatic interactions, we previously only achieved agreement between experiment and simulations without HI when we rescaled the calculated diffusivities D by the diffusivity of nanoparticles in a neutral gel D_{neutral} according to D/D_{neutral} [71]. With HI, we obtain quantitative agreement of the unrescaled diffusivities. As a consequence, it is crucial to include HI in the calculation of particle diffusivities in hydrogels whenever there are attractive interaction sites present. Furthermore, we systematically compare simulations with and without HI in order to elucidate how the effect of HI on the diffusivity is modified in the presence of attractive and repulsive long-range particle-gel interactions. Our simulations reveal that attractive interactions can significantly increase the effect of HI on the particle diffusivity, whereas repulsive interactions decrease the effect of HI.

5.1.1. Theory

The inclusion of HI into our model is achieved along the lines described in the 2010 paper by Stylianopoulos and coworkers [34]. The method is based on the Stokesian dynamics method, developed by Durlofsky, Brady, Bossis and Phillips [94,95] and extended for the study of spherical particle diffusion in (immobile) fibrous media by Phillips, Deen and Brady [26]. The method is briefly outlined here and derived in detail in appendix B.

The cylindrical fibers are modeled by straight arrays of spheres, as indicated in section 5.1.1. The local mobility tensor $\mathbf{M}_{\mathrm{self}}(\vec{r})$ of the diffusing particle at position $\vec{r}$ is calculated in a three step process. In step 1, the position-dependent mobility matrix $\mathbf{M}^{\mathrm{pbc}}(\vec{r})$ which accounts for the far-field two-particle HI is calculated, using the Ewald-sum of the Rotne-Prager tensor in the presence of periodic boundary conditions [96]. In step 2, near-field HI is added to the inverted far-field mobility matrix in order to obtain the 3×3 particle self-resistance matrix $\mathbf{R}_{\mathrm{self}} = (\mathbf{M}^{\mathrm{pbc}})^{-1}_{00} + \mathbf{R}^{\mathrm{lub}}$, this step is referred to as lubrication approximation. In step 3, the particle self-resistance matrix is inverted to obtain the local mobility tensor for the particle that includes near-field and far-field HI between the particle and the fiber network according to

$$\mathbf{M}_{\mathrm{self}} = (\mathbf{R}_{\mathrm{self}})^{-1} \ . \tag{5.1}$$

Note that for a freely diffusing particle, $\mathbf{M}_{\mathrm{self}}$ has only diagonal components equal to $1/(3\pi\eta p)$, where p is the particle diameter and η is the fluid viscosity. A more detailed description of the method, including techniques we employ to decrease the computational cost, is given in appendices B, C and D.

To simulate the random Brownian motion of the particle, we employ the Euler algorithm

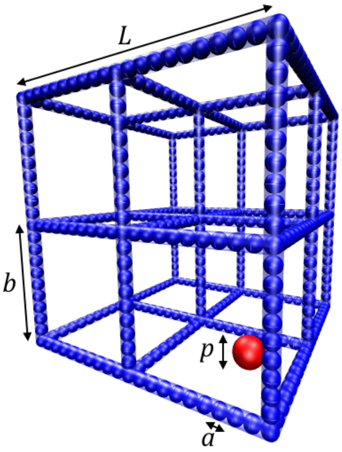

Figure 5.1. Sketch of the periodic simulation box with periodicity $L = 2b$ and mesh size b. The diffusing particle is shown as a red sphere of diameter $p/b = 0.2$. The rigid, cylindrical fibers (blue) are modeled as arrays of adjacent spheres of diameter $a/b = 0.1$.

to discretize the Langevin equation

$$\vec{r}(t+\Delta t)-\vec{r}(t) \;=\; (\mathbf{R}_{\text{self}}(\vec{r}(t)))^{-1}\cdot[\vec{F}(\vec{r}(t)) + \vec{F}_R(\vec{r}(t))]\,\Delta t + k_BT\vec{\nabla}\cdot(\mathbf{R}_{\text{self}}(\vec{r}(t)))^{-1}\,\Delta t \tag{5.2}$$

where $\vec{r}$ is the position of the particle, t is the time, the force $\vec{F} = -\vec{\nabla}U$ is the gradient of the interaction potential and the thermal energy k_BT is the product of the Boltzmann constant and the temperature. The random force $\vec{F}_R$ represents the fluctuating force exerted on the particle by the surrounding fluid. It is a stochastic Gaussian variable defined by $\langle\vec{F}_R\rangle = 0$ and $\langle\vec{F}_R(0)\vec{F}_R(t)\rangle = 2k_BT\mathbf{R}_{\text{self}}\delta(t)$ where $\delta(t)$ is the delta function. For our simulations, we calculate the random force as $\vec{F}_R = \sqrt{2/\Delta t}\,\mathbf{L}\cdot\vec{\zeta}$, where each component of $\vec{\zeta}$ is a Gaussian random number with zero mean and a variance of one and the matrix $\mathbf{L}$ is a lower triangular 3×3 matrix that is the result of the Cholesky decomposition $\mathbf{R}_{\text{self}} = \mathbf{L}\cdot\mathbf{L}^{\intercal}$. Since the self-mobility of the particle $(\mathbf{R}_{\text{self}})^{-1}$ is position dependent, the random force $\vec{F}_R$ is also position dependent. To balance the resulting drift term, the divergence of the mobility matrix $\vec{\nabla}\cdot(\mathbf{R}_{\text{self}})^{-1}$ is added in eq. (5.2) [44]. A modified mid-point scheme to calculate this term is outlined in appendix E.

The diffusivity D of the particle is obtained by linearly fitting the mean squared displacement (MSD) $\langle\Delta r^2(t)\rangle$ in the long-time limit according to

$$\langle\Delta r^2(t)\rangle \;=\; \int_0^{(T-t)} \frac{dt'}{T-t}(\vec{r}(t+t') - \vec{r}(t'))^2 \;=\; 6D\,t\;, \tag{5.3}$$

where T denotes the trajectory length. Without any fibers present in the solution the particle diffuses freely and $D = D_0$. In our simulation data, the error for the relative diffusivities D/D_0 is always below 5%. To demonstrate that the long-time limit for the MSD is reached, exemplary MSD plots are presented in fig. 5.9.

Interaction potentials

The particle interacts with the cylindrical fibers via hard-sphere steric interactions and a nonsteric exponential interaction potential. To account for hard sphere repulsion, a new particle position is not accepted, if at the new position the distance between the particle and any fiber is smaller than $(a+p)/2$, where p is the particle diameter and a the fiber diameter (c.f. section 5.1.1).

The long-range interaction potential is defined as

$$U(\vec{r}) = \sum_{n=1}^{N_f} U_0 \exp\left(-\frac{\rho_n}{k}\right) , \tag{5.4}$$

where ρ_n is the closest distance between the particle and the nth fiber, N_f is the number of fibers in the periodic simulation box, k is the interaction range and U_0 is the strength of the potential. For negative values of U_0 the potential is attractive and for positive values it is repulsive.

For electrostatic interactions, the interaction range k corresponds to the Debye screening length [55]

$$k^2 = \frac{1}{4\pi l_B I} , \tag{5.5}$$

where e is the elementary charge, $l_B = e^2/4\pi\epsilon k_B T$ the Bjerrum length and ϵ the permittivity. $I = 1/2\sum_j n_j z_j^2$ is the ionic strength and z_j the valence of salt ion j and n_j its bulk number density. The bulk number density n is related to the molar ion concentration through $C_{\mathrm{Ion}} = n/N_A$, where N_A is the Avogadro constant. U_0 can be interpreted as the product of the particle charge and the linear polymer charge density [71].

5.1.2. Simulations

Calculating HI with the Stokesian dynamics method is computationally costly, since it involves the inversion of the large far-field mobility matrix $\mathbf{M}^{\mathrm{pbc}}$. In our simulations, we can significantly reduce the computational cost by calculating the far-field HI, given by $(\mathbf{M}^{\mathrm{pbc}})^{-1}$, for 64,000 points on a regularly spaced 3D grid in the simulation box before the simulation commences. This is possible, since the geometry of the fiber lattice is fixed and periodic. The resulting precomputed far-field resistance tensors are stored in an array, which is used as a lookup table throughout the simulation. A more detailed description of this method is given in appendix F. Lubrication has to be calculated at every iteration step, since the near-field hydrodynamic resistance varies strongly for small particle distances [26]. For simulations without HI, we use a timestep of $\Delta t = 5 \times 10^{-6} b^2/(\mu_0 k_B T)$, where μ_0 is the bulk sphere mobility of the particle. When HI are present, the displacement of the particle at each timestep is smaller, thus a larger timestep of $10^{-5} b^2/(\mu_0 k_B T)$ can be used. Each simulation consists of a single particle trajectory of $\sim 10^9$ steps We limit our investigation to systems with fiber to particle diameter ratios $a/p \leq 0.5$. Furthermore, we only employ fiber diameters for which the ratio b/a is an integer, i.e. one edge of the simulation cell consists of an integer number of touching spheres. For example, in section 5.1.1 the ratio is $b/a = 10$.

We employ the Ewald summation technique to calculate the far-field mobility matrix (c.f. appendix C), which requires a completely periodic system with periodicity L. Consequently, the diffusing particle is also periodically repeated. To minimize spurious interactions between the particle and its periodic images, the simulation box has to be sufficiently large. In previous publications, this problem is tackled by extrapolating the diffusivity as a function of L with the help of finite-size correction function [92]. Due to the symmetry of our fiber lattice and the precomputation of the mobility matrix, we can increase L without much cost, so we do not need to use such an approximation. We find that for systems of size $L = 2b$, consisting of $2 \times 2 \times 2$ cubic unit cells, system size effects are negligible (c.f. fig. 5.10, supplementary information). Hence, $L = 2b$ is employed for all simulations with HI.

5.2. Results and Discussion

First, we present our simulation results for particle diffusion in purely steric gels to demonstrate that HI are relevant and that the inclusion of HI greatly improves the agreement of model results with published experimental data. Subsequently, our results for interacting gels are presented.

5.2.1. Purely steric gels

Figure 5.2a shows the particle diffusivity as a function of the fiber volume fraction ϕ for different fiber to particle diameter ratios a/p for purely steric gels, i.e. for zero interaction potential strength U_0. The polymer volume fraction of our system follows from the expression

$$\phi(a/b) = \frac{3\pi}{4}\left(\frac{a}{b}\right)^2 - \sqrt{2}\left(\frac{a}{b}\right)^3 \tag{5.6}$$

which corresponds to the volume of three overlapping orthogonal cylinders of diameter a and length b divided by the volume of the cubic cell of size b. The prefactor $\sqrt{2}$ in the second term in eq. (5.6) results from the shared volume of three orthogonal cylinders. As seen in fig. 5.2a, inclusion of HI leads to a pronounced decrease in diffusivity, in particular for intermediate polymer volume fractions around $\phi \approx 0.05 - 0.1$, where D is reduced by about a factor of two due to HI. Hydrodynamic simulations without lubrication exhibit slightly larger diffusivities than simulations with full HI.

The black lines in fig. 5.2a correspond to a stretched exponential function

$$D/D_0 = \exp(-\alpha\phi^n) \ , \tag{5.7}$$

fitted to the simulation data. The corresponding fit parameters are given in table 5.1. For simulations with HI (full HI and HI w/o lubrication in fig. 5.2a), the simulation data and the stretched exponential fit agree nicely. The data without HI is also well described by a stretched exponential function when we exclude the data point for $\phi = 0.21$, which corresponds to the situation where the particle diameter becomes as large as the mesh size minus the fiber diameter, $p = b - a$, resulting in near immobilization of the particle. When

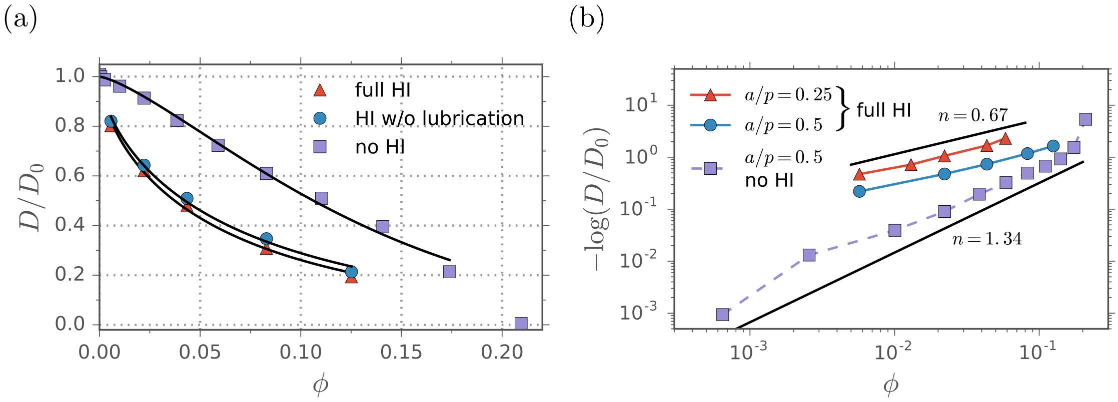

Figure 5.2. (a) The relative particle diffusivity D/D_0 as a function of the fiber volume fraction ϕ for purely steric particle-fiber interactions and a fiber-particle diameter ratio of $a/p = 0.5$. The colored symbols correspond to the data for simulations with lubrication (full HI), without lubrication (HI w/o lubrication) and without HI (no HI). The lines correspond to stretched exponential fits (c.f. eq. (5.7)) and the fit parameters are given in table 5.1. In (b) diffusivities for $a/p = 0.5$ and $a/p = 0.25$ with full HI (continuous line-connected symbols) and without HI (dashed line-connected symbols) are presented in a log-log versus log plot to demonstrate the stretched exponential scaling behavior.

Table 5.1. The fit parameters of a numerical stretched exponential fit, eq. (5.7), to the data presented in fig. 5.2. The relative errors of the fit parameters are on the order of 5%.

a/p		α	n
0.5	full HI	6.3	0.67
	HI w/o lubrication	6.0	0.68
	no HI	14.0	1.34

HI are included, the fit parameter n for purely steric simulations, listed in table 5.1, is very close to $n = 0.7$ similar to results in a previous theoretical paper including HI [33] and numerous experimental papers wich reported values of $n = 0.6-0.75$ [66], $0.73-0.84$ [63], $0.65-0.88$ [54], 0.7 [74].

In order to graphically demonstrate the stretched exponential scaling of the simulation data, we present fig. 5.2b where we clearly see a power law between $\log(D/D_0)$ and ϕ for the HI data. The data without HI also follows a straight line in this plot, except for large ϕ. The black lines in fig. 5.2b indicate the power law scaling of the numerical fits. Thus, we find that inclusion of HI leads to a significantly smaller exponent n. This trend is also seen for disordered gels where an exponent of $n = 1.09$ has been reported for simulations without HI [73], which is significantly larger then the exponent $n \sim 0.7$ reported for simulations of disordered lattices with HI [33].

Next, we perform a quantitative comparison between our simulation data and published theoretical and experimental results. Phillips [29] suggested a heuristic fit formula for the diffusivity of particles in a purely steric gel with HI which gives good agreement with published experimental data:

$$D/D_0 = \exp(-\pi\phi^m)\ \exp(-[0.84(1+p/a)^2\,\phi]^{1.09})\ , \tag{5.8}$$

where the heuristic expression for the exponent $m = 0.174\ln(59.6a/p)$ was obtained by fitting simulation data for ratios a/p between 0.1 and 2 [28]. The diffusivity is expressed as the product of a hydrodynamic and a steric contribution, corresponding to the first and the second exponential in eq. (5.8), respectively. The hydrodynamic contribution results from the average frictional drag of the particle in the presence of a disordered array of cylinders [75]. The constants 0.84 and 1.09 for the steric contribution were obtained by fitting simulation data for a spherical particle diffusing in disordered networks of randomly oriented straight fibers without HI [73]. In fig. 5.3 we compare our simulations to eq. (5.8) and to experimental data. Note, that in our simulations, the relative fiber diameter a/b determines ϕ (c.f. eq. (5.6)). The relative particle diameter p/b follows from the experimental ratio a/p. Figure 5.3a shows data for RNAse diffusion in polyacrylamide gel with a ratio $a/p = 0.32$ measured by Tong and Anderson [76]. When HI are neglected, our simulation data disagree with the experiments and also with eq. (5.8). For the simulations with HI, we find quantitative agreement to eq. (5.8), except for large $\phi \geq 0.12$, where D becomes zero in our simulations, since the particle gets immobilized inside the cubic cell if $a + p \geq b$. In comparison to the experimental data, our simulations with HI exhibit almost quantitative agreement for $\phi \leq 0.12$, but slightly underestimate the diffusivities. This tendency of underestimating the diffusivities compared to experiments becomes more pronounced for smaller ratios $a/p = 0.18$ and $a/p = 0.1$, respectively, in fig. 5.3b for BSA diffusion in polyacrylamide gel as measured by Tong and Anderson [76] and Park et al. [77] and in fig. 5.3c for BSA diffusion in calcium alginate by Amsden [28]. Nevertheless, except for large ϕ, we observe good qualitative agreement between our simulations and the experimental data, and in particular quantitative agreement with eq. (5.8). Note that the experimental a/p ratios are taken from [29]. In fig. 5.3d the simulation data for all different values of $a/p = 0.5, 0.32, 0.18$ and 0.1 are shown as function of the effective volume fraction ϕ_{eff}, which is the ratio of the gel volume that is accessible to the center of the particle to the total volume. We can calculate ϕ_{eff} analytically by use of eq. (5.6) with an effective fiber diameter of $a+p$, i.e. $\phi_{\text{eff}} = \phi((a+p)/b)$. Without HI, the data in fig. 5.3d all fall on the same line. For simulations with HI, the differences in D between the a/p curves are small, compared to their difference to the data without HI. Thus, for the study of hydrodynamic effects on particle diffusion in interacting gels in the next section, the specific ratio a/p chosen for the simulations is not a dominant factor. Note, that even in the limits $a \to 0$ and $p \to 0$ HI will not vanish (c.f. eq. (C.1)) since even a point particle exerts a finite force on the solvent which influences the fluid flow field. In fig. 5.3d we also include the line obtained by fitting eq. (5.7) the data with HI. For the fit, we exclude the points where the particle is immobilized for $\phi_{\text{eff}} > 0.93$. The resulting stretched exponential fit formula to predict the particle diffusivity,

$$D/D_0 = \exp(-2.1\phi_{\text{eff}}^{0.8})\,, \tag{5.9}$$

is independent of the ratio a/p.

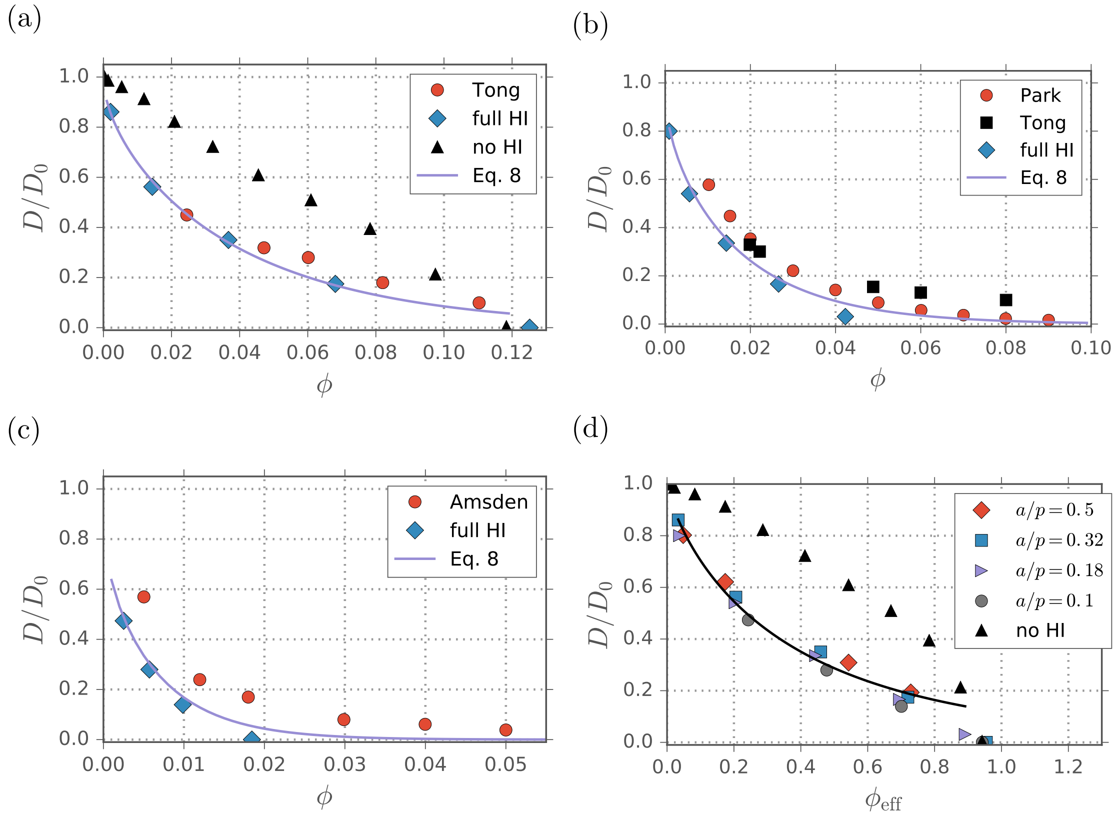

Figure 5.3. Relative particle diffusivity D/D_0 as a function of the fiber volume fraction ϕ. Experimental data is shown for (a) RNAse diffusion in polyacrylamide gel ($a/p = 0.32$) reported by Tong and Anderson [76], (b) BSA diffusion in polyacrylamide gel ($a/p = 0.18$) reported by Tong and Anderson [76] and Park et al [77], (c) BSA diffusion in calcium alginate gel ($a/p = 0.1$) reported by Amsden [28]. (d) shows the diffusivity as a function of the effective volume fraction ϕ_{eff} for different ratios a/p for simulations with hydrodynamics and without HI. Smaller a/p values lead to somewhat smaller diffusivities, but the effect of including hydrodynamics is much larger compared to the effect of changing the ratio a/p. The black line denotes eq. (5.9).

5.2.2. Interacting gels

In this section we study the effect of HI on particle diffusion in the presence of nonsteric long-range particle-gel interactions. We first test our model by comparing to experimental data. Subsequently, we investigate how HI affect the particle mobility for varying attractive and repulsive interaction potential strength, interaction range and particle diameter. Finally, we examine the effect of lubrication on the diffusivity.

Comparison to experiment

In previous experiments the diffusivity of the fluorophore Alexa488 in charged dextran hydrogels was determined by fluorescence correlation spectroscopy [54]. Alexa488 has a net negative charge. Dextran(+) and dextran(-) gels are positively and negatively charged, respectively (a detailed description of the experimental methods can be found in [54]). The following model parameters are dictated by the experiment. The particle diameter p corresponding to Alexa488 is 1.5 nm [54], the fiber diameter a corresponding to a hydrated dextran molecule is 0.8 nm [54] and the experimental dextran concentration is C_{poly} =1 %w/v. The interaction range k for the simulations is calculated from the salt concentration C_{Ion} by use of eq. (5.5). Figure 5.4a shows a comparison between the experimental diffusivities and data for simulations without HI as a function of added salt concentration. The experimental data is presented as full symbols and the simulation data is presented as line-connected crosses. The mesh size $b = 23$ nm and the potential strengths $U_0/k_BT = -7.5$ and 4.5 for the attractive and repulsive case are chosen for good agreement between simulation and experimental data. The estimation of the optimal parameters b and U_0 is outlined in the supplementary information (c.f. figs. 5.11 and 5.12). The ratio of attractive to repulsive interaction strength is approximately 5/3, as follows from the experimental charge ratio of the cationic and anionic dextran gels [54]. Note, that in our previous publication, slightly different interaction strengths $U_0/k_BT = -8$ and 5 were chosen for the attractive and repulsive cases, respectively [54]. The mesh size b can be calculated for completely straight dextran polymers using $C_{\text{poly}} \approx (3/l_{\text{dex}}b^2)m_{\text{mon}}$, where $l_{\text{dex}} = 0.39$ is the dextran monomer length [86], $3/l_{\text{dex}}b^2$ the dextran monomer density and $m_{\text{mon}} = 162$ Da the dextran monomer mass. The result is a mesh size of $b \approx 14$ nm, which is significantly smaller than $b = 23$ nm used for the simulations without HI in fig. 5.4a. This indicates that the individual dextran gel fibers are crumpled, which leads to a larger mesh size b for a fixed polymer concentration, compared to completely straight dextran polymers. As shown in fig. 5.4a, simulation and experimental data are in qualitative agreement for $b = 23$ nm when HI are neglected. For Alexa488 in similarly charged dextran(-), the diffusion is almost unhindered for most salt concentrations. On the other hand, the diffusivity of negative Alexa488 molecules in oppositely charged dextran(+) gels basically goes to zero for small C_{Ion}. With increasing screening of the electrostatic attraction between Alexa488 and the cationic dextran polymers, D strongly increases until it reaches the diffusivity of a neutral gel with completely screened electrostatic interactions, which is $D/D_0 \approx 1$ for the simulations and $D/D_0 \approx 0.9$ for the experiment, i.e. for a neutral gel the simulated diffusivity is about 10% larger than the experimental diffusivity. This is due to the simple way the model without HI treats the neutral gel. When HI are neglected,

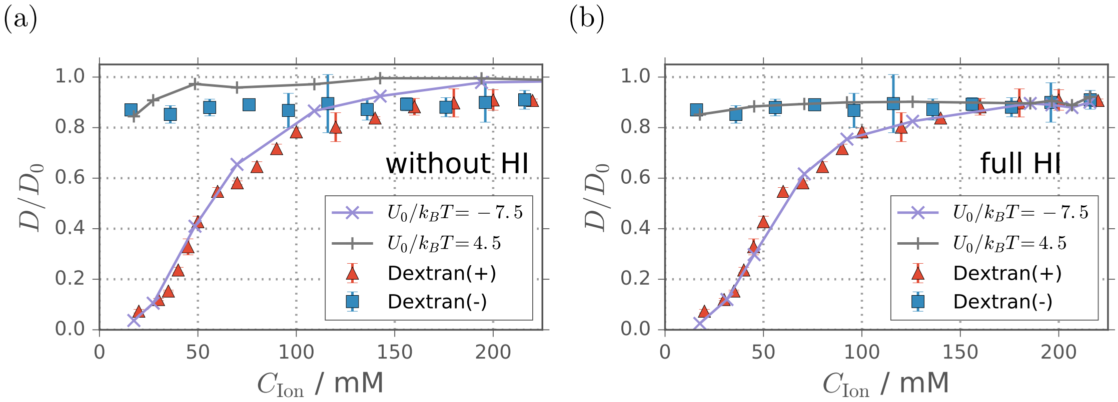

Figure 5.4. The diffusivity of negatively charged Alexa488 fluorophores in positive dextran(+) and negative dextran(-) hydrogels at a dextran concentration of 1%w/v, as a function of the salt concentration C_{Ion} including the counterions that enter the solution upon addition of the dextran polymers [54]. For the simulations, C_{Ion} is calculated from the interaction range by use of eq. (5.5). The model parameters are $p = 1.5$ nm, $a = 0.8$ nm and $b = 23$ nm, for the data without HI in (a). For simulations with HI in (b), the mesh size is increased to $b = 28$ nm. Inclusion of HI leads to quantitative agreement between the simulations and the experimental data. For all plots, the simulation data is presented as connected crosses and the experimental data as filled symbols.

there are only steric interactions between the particle and the fibers in the neutral gel, which are virtually negligible for the small Alexa488 molecule with $(a + p)/b = 0.1$ [71]. Note that in [54] we rescaled D by D_{neutral}, which is the diffusivity for a neutral gel, in order to make up for this systematic shift.

As shown in fig. 5.4b, inclusion of HI in our simulation model leads to a general downward shift of the simulated diffusivity for all salt concentrations. For the simulations with HI, we perform an independent estimation of the optimal simulation parameters b and U_0 as outlined in the supplementary information (c.f. fig. 5.14). Quantitative agreement between simulation and experimental data at nearly all salt concentrations is achieved for the same interactions strengths $U_0/k_BT = -7.5$ and 4.5 for the attractive and the repulsive case, respectively, and an increased mesh size of $b = 28$ nm. We find that our simple model for nanoparticle diffusion in gels with electrostatic interactions predicts diffusivities in quantitative agreement with experimental data, provided that HI between particle and fibers are taken into account.

Attractive and repulsive interactions change the effect of HI

In fig. 5.5, we study how the strength and the sign of the interaction potential influence the particle mobility. The relative diffusivity D/D_0 is shown as a function of the potential strength U_0 for simulations without and with HI in figs. 5.5a and 5.5b, respectively. We employ different particle diameters $p/b = 0.1, 0.2$ and 0.5 which are all significantly smaller than the mesh size b. In all cases, the fiber diameter is $a/b = 0.05$ which corresponds to a small volume fraction $\phi = 0.006$, in order to avoid the dominance of steric interactions.

Experimentally, ratios of $a/p = 0.5$, 0.2 and 0.1 correspond to nanoparticles with diameters of 20 nm to 100 nm that diffusive in mucus with fiber diameters of around 10 nm [97]. For all simulations, the interaction potential range is set to $k/b = 0.1$. For the data with HI in fig. 5.5b, increasing the magnitude of the interaction strength U_0 reduces the mobility of the particle for both the attractive case, $U_0 < 0$, and the repulsive case, $U_0 > 0$, although only weakly so for the largest particle with $p/b = 0.5$. The maximal diffusivity is thus achieved for zero interaction potential strength, i.e. for purely steric gels. For most data points, simulations without lubrication (dashed line-connected symbols in fig. 5.5b) exhibit slightly higher diffusivities than simulations with full HI (continuous line-connected symbols), in accordance to simulations in purely steric gels in fig. 5.2a.

The curves for simulations without HI in fig. 5.5a are shifted upwards compared to the data curves with HI in fig. 5.5b, the more so for larger particle diameters p. Otherwise, the curves in figs. 5.5a and 5.5b are qualitatively very similar. A closer look, however, reveals that there are qualitative differences between the diffusive behaviors with and without HI. For example, for the largest particle diameter $p/b = 0.5$ in fig. 5.5a we see a moderate gain in mobility for increasingly attractive interaction potentials, $U_0 < 0$. In contrast, when HI are included (fig. 5.5b) the diffusivity is maximal for $U_0 = 0$.

In order to investigate the effect of HI for $U_0 \neq 0$ more closely, we examine the ratio $(D_{\mathrm{no\,HI}} - D_{\mathrm{HI}})/D_{\mathrm{no\,HI}}$ in fig. 5.6. This ratio quantifies the decrease of the diffusivity when HI are included in the simulation, i.e. the hydrodynamic effect on the diffusivity. If the hydrodynamic effect on the diffusivity is small, the ratio is close to 0, when the hydrodynamic effect increases, the ratio becomes closer to 1. In fig. 5.6a we present $(D_{\mathrm{no\,HI}} - D_{\mathrm{HI}})/D_{\mathrm{no\,HI}}$ as a function of U_0, with D_{HI} from fig. 5.5b and $D_{\mathrm{no\,HI}}$ from fig. 5.5a. At first glance, one can see that the hydrodynamic effect in fig. 5.6a increases with increasing particle diameter p/b, in accordance to our qualitative observations in fig. 5.5b. Moreover, fig. 5.6a reveals that the hydrodynamic effect strongly depends on the sign of the interaction strength U_0. For repulsive interaction potentials ($U_0 > 0$) the hydrodynamic effect decreases, compared to purely steric gels ($U_0 = 0$). For attractive interaction potentials ($U_0 < 0$), by contrast, the hydrodynamic effect increases. The increase for $U_0 < 0$ is particularly pronounced for $p/b = 0.1$ and 0.2. For instance, for a purely steric gel ($U_0 = 0$) and $p/b = 0.2$ the hydrodynamic effect on the diffusivity corresponds to an approximately 30% reduction in particle mobility. For a strongly attractive interaction potential with $U_0/k_BT = -20$, by contrast, the reduction is about 60% for $p/b = 0.2$, thus it has doubled compared to $U_0 = 0$. In fig. 5.6b we present the effect of the interaction range k on the hydrodynamic effect. When eq. (5.4) is used to model electrostatic interactions, k corresponds to the Debye screening length (c.f. eq. (5.5)). With decreased screening of the long-range particle-gel interactions, i.e. with increasing k, the hydrodynamic effect on the diffusivity slightly decreases for repulsive potentials $U_0/k_BT = 5$ and 10 but significantly increases for attractive potentials $U_0/k_BT = -5$ and -10. Similarly to fig. 5.6a, we find asymmetric behavior with respect to the sign of the interaction and also that HI are particularly important for strongly attractive interaction potentials.

To understand why the hydrodynamic effect is asymmetric with respect to the sign of U_0, we calculate the mean distance $\langle \rho_{\mathrm{nearest}} \rangle = (\langle \rho^{(xy)}_{\mathrm{nearest}} \rangle + \langle \rho^{(yz)}_{\mathrm{nearest}} \rangle + \langle \rho^{(zx)}_{\mathrm{nearest}} \rangle)/3$ of the particle to the nearest fibers averaged over the three orthogonal planes along xy, yz and

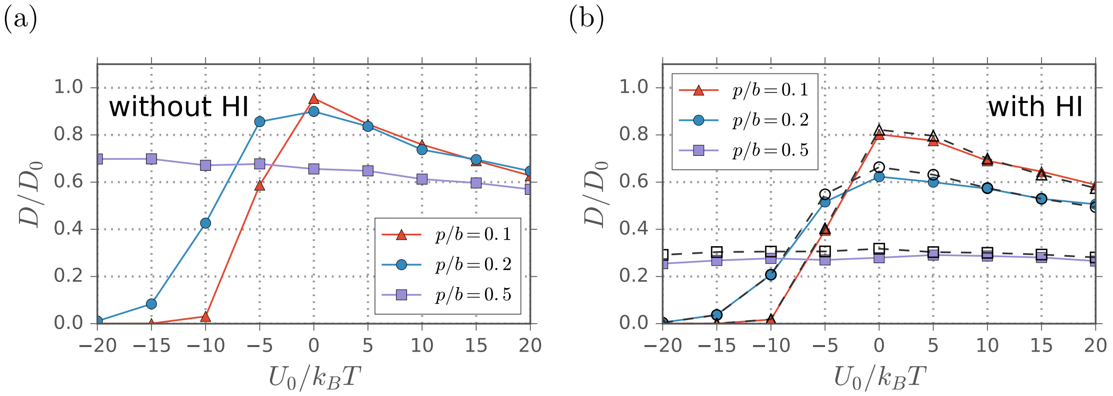

Figure 5.5. Particle diffusivity as a function of the interaction strength U_0 for an interaction range of $k/b = 0.1$ and a polymer diameter of $a/b = 0.05$ ($\phi = 0.006$) is presented for different particle diameters p. (a) shows data without HI. (b) shows simulations with full HI (solid line connected symbols). The dashed line connected unfilled symbols are for simulations without lubrication. Inclusion of HI decreases the diffusivity, in particular for larger particles.

zx. In fig. 5.7a we present $\langle \rho_{\text{nearest}} \rangle$ (right y-axis) in conjunction with the hydrodynamic effect on the diffusivity $(D_{\text{no HI}} - D_{\text{HI}})/D_{\text{no HI}}$ (left y-axis) as a function of U_0 for $p/b = 0.2$. One can see that $\langle \rho_{\text{nearest}} \rangle$ and the hydrodynamic effect are anticorrelated. For repulsive interactions ($U_0 > 0$), $\langle \rho_{\text{nearest}} \rangle$ increases since the particle tends to stay away from the repulsive fibers and is mostly found near the centers of the cubic lattice cells [71]. This is illustrated in fig. 5.7a in the inset figure on the right (blue beads) which depicts 2000 typical particle positions during the simulation. An increasing $\langle \rho_{\text{nearest}} \rangle$ leads to a decrease in HI between the fibers and the particle, compared to the purely steric case and thus a decreasing hydrodynamic effect. For attractive $U_0 < 0$, on the other hand, $\langle \rho_{\text{nearest}} \rangle$ decreases significantly since the particle stays close to the strongly attractive lattice vertices [71], as illustrated in the left inset figure with typical particle position shown as red beads, which causes a rising hydrodynamic effect. In fig. 5.7b we show the hydrodynamic effect with respect to k. Here, one can also see that the hydrodynamic effect and $\langle \rho_{\text{nearest}} \rangle$ are anticorrelated. The mean distances $\langle \rho_{\text{nearest}} \rangle$ for all data in figs. 5.6a and 5.6b are shown in the supplementary information in fig. 5.15

Nonsteric interactions reduce lubrication effect

To understand the effect of lubrication on the diffusivity ratio $(D_{\text{no HI}} - D_{\text{HI}})/D_{\text{no HI}}$ in fig. 5.6, we compare the data for simulations with full HI (filled symbols, solid lines) to the data for simulations with HI but without lubrication (unfilled symbols, dashed lines). For purely steric gels, $U_0 = 0$ in fig. 5.6a and $k = 0$ in fig. 5.6b, we observe an increased hydrodynamic effect for simulations with full HI compared to simulations without lubrication, in accordance to fig. 5.5. However, both in the case of strongly attractive ($U_0 < -5k_BT$) and strongly repulsive ($U_0 > 5k_BT$) interaction potentials in fig. 5.6a, as well as for long screening lengths $k/b > 0.1$ in fig. 5.6b, the difference between

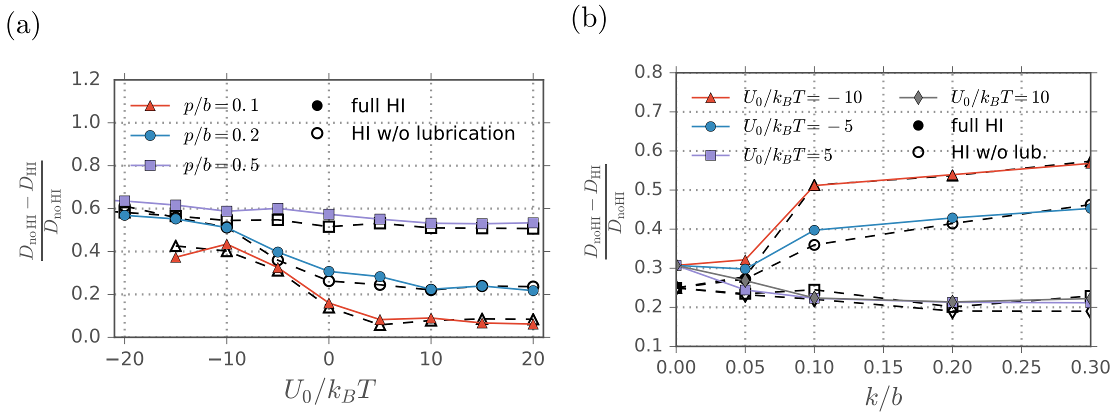

Figure 5.6. The hydrodynamic effect on the diffusivity $(D_{\mathrm{no\,HI}} - D_{\mathrm{HI}})/D_{\mathrm{no\,HI}}$ for different particle diameters $p/b = 0.1$, 0.2 and 0.5 for simulations with full HI and without lubrication shown as filled and empty symbols, respectively. In (a), the hydrodynamic effect is shown as a function of the interaction potential strength. Note that for $U_0 = -20k_BT$ and $p/b = 0.1$ data are not converged and therefore omitted. In (b) the hydrodynamic effect is plotted as a function of the interaction range k. For attractive interaction potentials, $U_0 < 0$, the hydrodynamic effect increases, compared to a purely steric gel ($U_0 = 0$ or $k = 0$). For repulsive interaction potentials on the other hand, the hydrodynamic effect becomes weaker compared to purely steric gels. The effect of lubrication becomes small for strong nonsteric interactions, i.e. large U_0 and k.

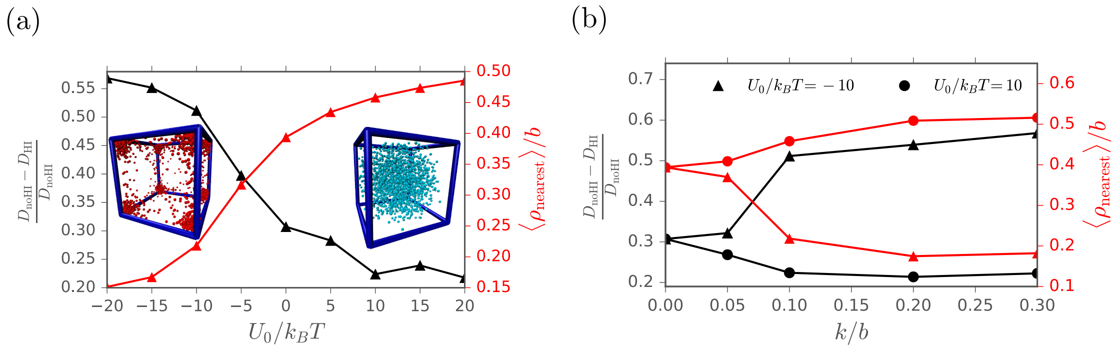

Figure 5.7. We compare the hydrodynamic effect on the diffusivity $(D_{\mathrm{no\,HI}} - D_{\mathrm{HI}})/D_{\mathrm{no\,HI}}$ (left y-axis) and the mean distance $\langle \rho_{\mathrm{nearest}} \rangle$ of the particle to the nearest fibers averaged over the three planes xy, yz and zx (right y-axis). In (a), the data is shown as a function of the interaction potential strength for $k/b = 0.1$ and in (b) as a function of the interaction range k for $p/b = 0.2$. The hydrodynamic effect and mean distance are anticorrelated. The inset figures in (a) depict simulation snapshots to illustrate the particle positions during simulation. For $U_0 \ll 0$, the particle is trapped at the vertices, causing small $\langle \rho_{\mathrm{nearest}} \rangle$. For $U_0 \gg 0$, the particle moves to the center of the lattice cell which results in larger $\langle \rho_{\mathrm{nearest}} \rangle$.

simulations with and without lubrication becomes very small. This indicates that the effect of lubrication on the diffusivity nearly vanishes for strong nonsteric interactions. In the repulsive case $U_0 > 0$ the reason for the weak lubrication effect on the diffusivity is relatively intuitive. The particle stays away from the fibers, as shown in figs. 5.7a and 5.7b, which decreases the effect of near-field HI. For the attractive case, on the other hand, the particle stays close to the fibers (c.f. figs. 5.7a and 5.7b), which, intuitively, should lead to an increased effect of lubrication on the diffusivity. However, in figs. 5.6a and 5.6b the effect of lubrication on the long-time diffusivity is almost negligible for $p/b = 0.1$ and 0.2 and $U_0 \ll 0$. In order to understand why lubrication has such little effect on the diffusivity for $U_0 \ll 0$, let us consider the diffusive behavior of the particle. For most of the time during the simulation, the particle is trapped at the strong local potential minima at the fiber lattice vertices [71], as illustrated in the left inset figure with typical particle positions (red beads) in fig. 5.6a. The long-time diffusive behavior is determined by intermittend crossings between the vertices [71]. An example for a trajectory with trapping at the vertices is shown in appendix G in fig. G.1a. The barrier crossing process between two vertices is equivalent to the Kramers problem. The particle has to overcome a potential barrier to escape from the potential well at the initial vertex [71]. The Kramers mean-first-passage time is given by [42]

$$\tau_{\mathrm{mfp}} = \frac{1}{D'_b} \theta \exp(\Delta U / k_B T) \tag{5.10}$$

where ΔU is the barrier height, θ is a constant that depends on the curvatures of the potential well and top and the thermal energy $k_B T$ and D'_b is the diffusion coefficient at the barrier top. Thus, we note that the long-time diffusive behavior depends on the hydrodynamic friction at the barrier top, which determines D'_b. For our simulations, we can calculate the average diffusion coefficient $\langle D' \rangle$ by averaging the diagonal elements of the particle self-mobility matrix during the simulation [75]. In fig. 5.8 we plot the fraction $1 - \langle D'_{\mathrm{full\,HI}} \rangle / \langle D'_{\mathrm{no\,Lub}} \rangle$, which represents the relative effect of lubrication on the average diffusion coefficient $\langle D' \rangle$ (left y-axis, colored bars) during barrier crossing and in the trapped state for $U_0/k_B T = -15$, -10 and $p/b = 0.1$, 0.2. We explain how we differentiate between trapping and barrier crossing events in appendix G. In fig. 5.8, the effect of lubrication is shown to be significantly smaller during barrier crossing than during trapping. Thus, D'_b in eq. (5.10) depends only weakly on lubrication and the long-time diffusivity for simulations with strong particle trapping is nearly independent of lubrication.

To show why $\langle D' \rangle$ depends only weakly on lubrication, we include a second y-axis on the right in fig. 5.8 for the mean distance of the particle to the nearest fibers $\langle \rho_{\mathrm{nearest}} \rangle$ indicated by black circles during barrier crossing and during trapping. The magnitude of $\langle \rho_{\mathrm{nearest}} \rangle$ is clearly anticorrelated with $1 - \langle D'_{\mathrm{full\,HI}} \rangle / \langle D'_{\mathrm{no\,Lub}} \rangle$. Thus, we conclude that the reduced effect of lubrication during barrier crossing is due to the fact that the particle moves away from two of the three fibers that meet at a vertex during the barrier crossing process. Interestingly, we also note in fig. 5.8 that the effect of lubrication during trapping is much more pronounced for smaller $p/b = 0.1$ particles than for larger $p/b = 0.2$ particles. However, we see nearly no effect of lubrication for $p/b = 0.1$ in figs. 5.6a and 5.6b, since

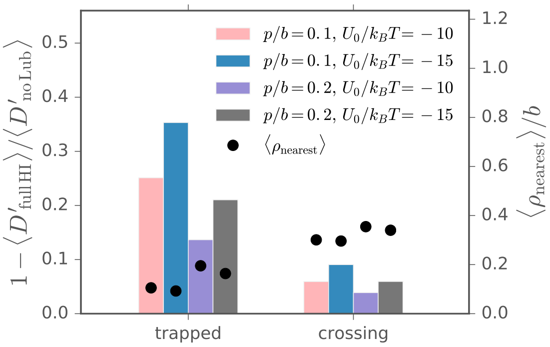

Figure 5.8. The left y-axis and colored bars show the fraction $1-\langle D'_{\rm full\,HI}\rangle/\langle D'_{\rm no\,Lub}\rangle$, which represents the change of the diffusion coefficient due to lubrication during barrier crossing between vertices (to the right) and during trapping (to the left). During barrier crossing, lubrication has only a small effect on the diffusion coefficient D', whereas during trapping, the effect of lubrication is about three to five times larger. The right y-axis and black circles represent the mean distance $\langle\rho_{\rm nearest}\rangle$ of the particle to the nearest fibers averaged over the three planes xy, yz and zx. The mean distances $\langle\rho_{\rm nearest}\rangle$ are anticorrelated with $1-\langle D'_{\rm full\,HI}\rangle/\langle D'_{\rm no\,Lub}\rangle$. The fraction of time during which the particle is in the process of barrier crossing is about 0.68% and 0.08% for $p/b=0.1$ and 15.8% and 1.7% for $p/b=0.2$ and $U_0/k_BT=-10$ and -15, respectively.

during barrier crossing $\langle\rho_{\rm nearest}\rangle$ has approximately the same magnitude for both $p/b=0.1$ and 0.2 in fig. 5.8.

5.3. Summary and Conclusion

We examine the diffusion of nanoparticles in interacting polymer gels with and without HI. For purely steric gels, inclusion of HI leads to good agreement between our simulations and published experimental data, as well as published theoretical results. For high fiber volume fractions our simulations underestimate the diffusivity, since the particle becomes caged due to the completely ordered cubic structure of the model network. Thus, our model is most appropriate for simulating small to intermediate fiber volume fractions (c.f. fig. 5.2). We provide a fit formula based on the effective volume fraction $\phi_{\rm eff}$ to predict the particle diffusivity independent of the fiber-particle diameter ratio a/p (c.f. eq. (5.9)).

For particle diffusion in the presence of long-range attractive and repulsive particle-gel interactions, we verify our model predictions by comparing with previously published experimental data for negatively charged Alexa488 diffusion in positive and negative dextran gels under varying salt concentrations and find quantitative agreement between simulation and published experimental data. With HI we are able to predict absolute diffusivities, whereas without HI we previously achieved agreement between simulation and experiment only for rescaled diffusivities [71]. We note that our current model assumed a perfectly cubic hydrogel structure, since it would be numerically costly to account for long-ranged hydrodynamic effects in the presence of spatial disorder. In a recent paper we have systematically investigated the effect of spatial disorder of the hydrogel on the particle diffusivity an found that the inclusion of spatial gel disorder improves the agreement with experimental particle diffusivity data [93]. Future modeling will be needed to understand the combined influence of spatial gel disorder and hydrodynamic interaction on the particle diffusivity.

By examining the hydrodynamic effect on the diffusivity, we find that repulsive interactions decrease the effect of HI, compared to purely steric gels. This occurs, since the particle moves away from the repulsive fibers, which causes a decrease in HI (c.f. fig. 5.7). For attractive interaction potentials, we report a pronounced increase of the hydrodynamic effect. The attractive interaction potential causes the particle to move very close to the fibers, which increases the HI between the particle and the polymer lattice (c.f. fig. 5.7). As a consequence, even for small particles the diffusivity is strongly affected by HI, when attractive long-range particle-fiber interactions are present. Thus, we conclude that for simulations with strongly attractive long-range particle-gel interactions in particular, HI are very important in order to obtain quantitatively correct diffusivities. In fig. 5.6b we observed that weak screening of the nonsteric interaction potential, i.e. a long interaction range k, has a similar impact on the hydrodynamic effect as a strong interaction strength U_0: For weakly screened attractive interaction potentials the hydrodynamic effect is increased, for weakly screened repulsive interaction potentials the hydrodynamic effect is reduced, compared to strong screening. For simulations at physiological conditions, the salt concentration is normally high, which corresponds to strong screening of electrostatic interactions.

We find that, compared to the effect of far-field HI, the effect of lubrication on the diffusivity becomes small for strong interaction potentials of either sign (c.f. fig. 5.6). This is a noteworthy result, since the numerical computation of lubrication is technically involved and computationally costly. Thus, it may be justified to neglect lubrication for simulations with strong nonsteric interactions between the gel and diffusing particle. This is true for diffusion in gels with attractive particle-gel interactions, for which the effect of nonsteric interactions on the particle diffusivity is usually much stronger compared to the effect of HI.

5.4. Supplementary Information

Estimate of optimal simulation parameters

In order to estimate the optimal parameters for the simulations without HI, we calculate the sum of the squared differences between the linearly interpolated experimental and the simulated rescaled diffusivities

$$\sigma^2 = \sum_{i=1}^{N_{\text{sim}}} ((D/D_{\text{neut}})_{\text{exp}}(C_{\text{Ion}}^{(i)}) - (D/D_{\text{neut}})_{\text{sim}}(C_{\text{Ion}}^{(i)}))^2 / N_{\text{sim}} \, , \tag{5.11}$$

where the diffusivity is rescaled by D_{neut} which is the particle diffusivity in a neutral gel, like in our previous publication [54]. $N_{\text{sim}} \geq 6$ is the number of simulation data points for each value of U_0. First, we estimate the optimal U_0 for different values of b by identifying the minimum of σ^2 in figs. 5.11a to 5.11d. The ratio between U_0 for the attractive and the

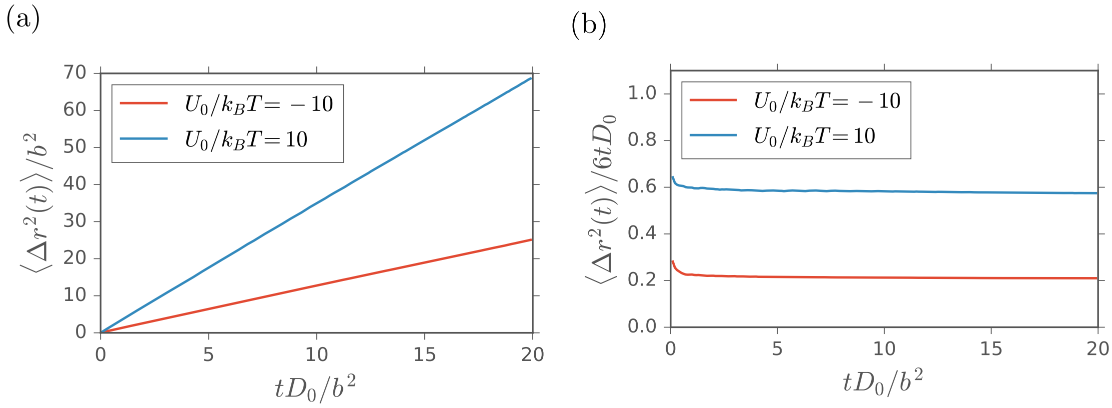

Figure 5.9. Exemplary results for (a) the mean squared displacement $\langle \Delta r^2(t) \rangle / b^2$ and (b) the mean squared displacement divided by time, $\langle \Delta r^2(t) \rangle / 6tD_0$, for simulations with hydrodynamic interactions. The interaction potential is attractive ($U_0/k_BT = -10$) or repulsive ($U_0/k_BT = 10$) and the interaction range is $k/b = 0.1$ with a fiber diameter of $a/b = 0.05$ and a particle diameter of $p/b = 0.2$. The slope of the mean squared displacement reaches a constant value in the long-time limit after a displacement of roughly $\langle \Delta r^2(t) \rangle > k^2$ for attractive potentials and $\langle \Delta r^2(t) \rangle > b^2$ for repulsive potentials, which reflects the distance the particle has to travel in order to escape the potential minimum [71].

repulsive case is fixed at 5/3 [54]. Next, the minima of σ^2 for the different b are compared in fig. 5.12. A mesh size of $b = 23$ nm with $U_0/k_BT = -7.5$ and 4.5 for the attractive and repulsive case, respectively, corresponds to the global minimum of σ^2 with respect to b and U_0. Figure 5.13 shows the rescaled diffusivities for the estimated optimal simulation parameters ($b = 23$ nm and $U_0/k_BT = -7.5$, 4.5) and the experiment.

For simulations with HI, optimal simulation parameters b and U_0 are estimated as follows: We calculate the squared differences between the experimental and the simulated diffusivities rescaled by the free-solution diffusivity D_0

$$\sigma^2_{\mathrm{HI}} = \sum_{i=1}^{N_{\mathrm{sim}}} ((D/D_0)_{\mathrm{exp}}(C^{(i)}_{\mathrm{Ion}}) - (D/D_0)_{\mathrm{sim}}(C^{(i)}_{\mathrm{Ion}}))^2 / N_{\mathrm{sim}} \, . \tag{5.12}$$

First, we estimate an optimal mesh size b for quantitative agreement between simulation and experiment at high salt concentrations C_{Ion} between 180 and 210 mM. Here, $N_{\mathrm{sim}} = 8$ and the potential strengths are $U_0/k_BT = -7.5$ and 4.5 for the attractive and repulsive case, respectively. Note that, at high $C_{\mathrm{Ion}} \geq 180$ mM the effect of the interaction potential on the diffusivity is nearly negligible [54]. In fig. 5.14a we find a minimum for σ^2_{HI} for a mesh size of $b = 28$ nm. Subsequently, for fixed $b = 28$ nm the optimal potential strength U_0 is estimated with fixed ratio 5/3 between the attractive $U_0 < 0$ and the repulsive scenarios $U_0 > 0$ for the full range of C_{Ion} between 20 and 210 mM. In fig. 5.14b the minimal σ^2_{HI} is found for $U_0/k_BT = -7.5$ and 4.5. Note, that the fiber diameter $a = 0.8$ nm, which corresponds to the diameter of a hydrated dextran polymer [54] is not varied for the different mesh sizes in figs. 5.11 and 5.14a.

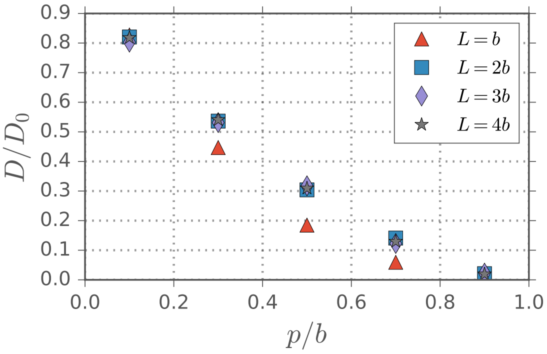

Figure 5.10. Relative diffusivities D/D_0 as a function of the particle diameter p with $a/b = 0.05$ for different system sizes L without lubrication. For $L \geq 2b$ the diffusivities are the same, i.e. there are no significant effects due to periodic boundary conditions. Hence, a system size of $L = 2b$ is employed for all simulations with HI.

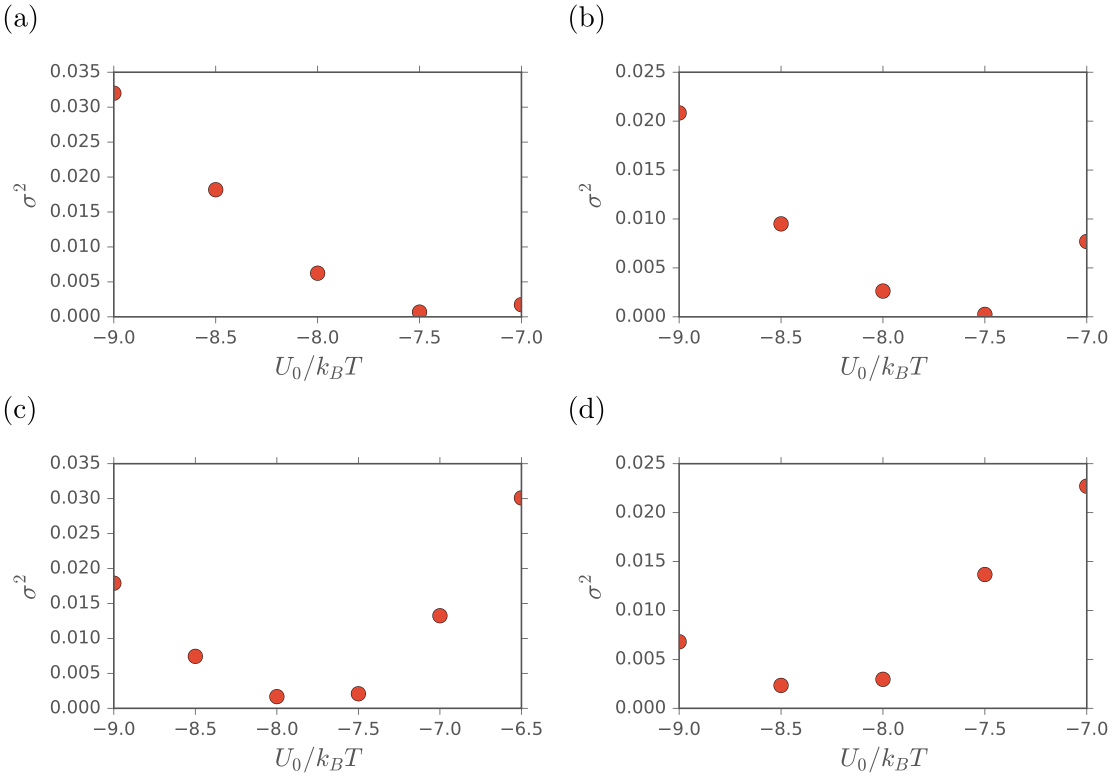

Figure 5.11. Squared differences between the experimental and the simulated rescaled diffusivities D/D_{neut} (c.f. eq. (5.11)) for simulations without HI as a function of U_0 for C_{poly} =1 %w/v. The x-axis shows the attractive interaction strength $U_0 < 0$. The particle diameter is $p = 1.5$ nm, the fiber diameter is $a = 0.8$ nm and the mesh size is (a) $b = 21$ nm, (b) $b = 23$ nm, (c) $b = 26$ nm and (d) $b = 29$ nm.

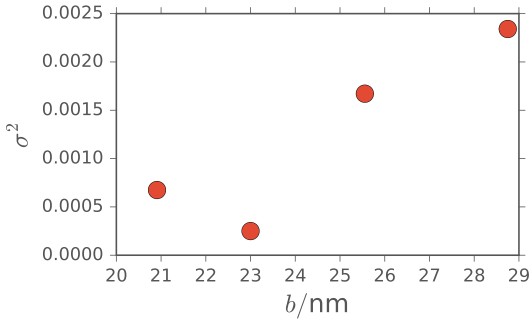

Figure 5.12. Squared differences between the experimental and the simulated rescaled diffusivities D/D_{neut} for simulations without HI as a function of the mesh size b for the optimal values of U_0 (as determined in fig. 5.11) for C_{poly} =1 %w/v.

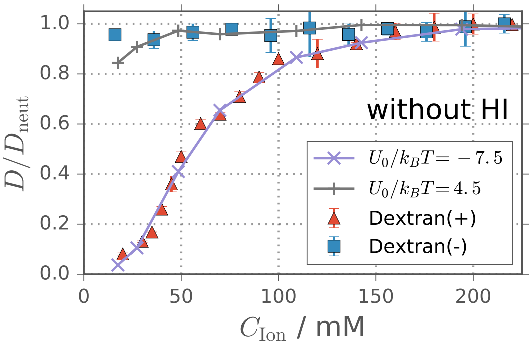

Figure 5.13. The rescaled diffusivity of Alexa488 in positive dextran(+) and negative dextran(-) at a dextran concentration of 1%w/v, as a function of the salt concentration C_{Ion} in comparison to simulations without HI for the estimated optimal model parameters $p = 1.5$ nm, $a = 0.8$ nm and $b = 23$ nm (c.f. figs. 5.11 and 5.12).

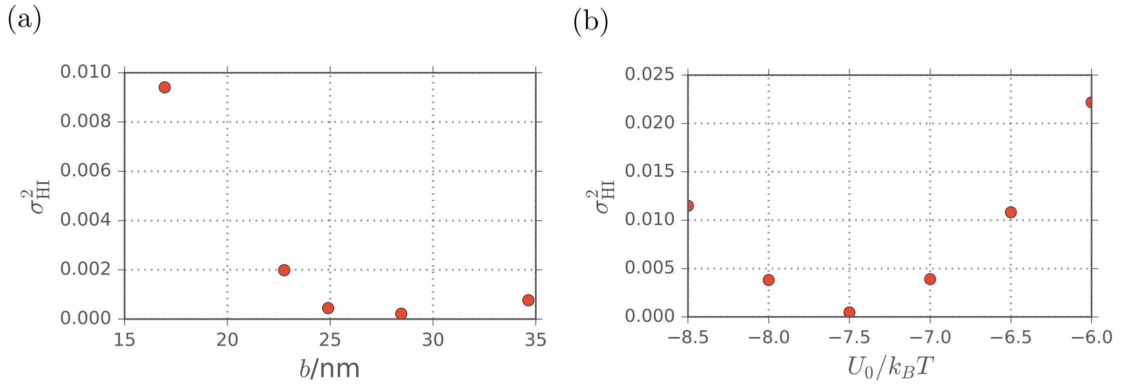

Figure 5.14. Squared differences (c.f. eq. (5.12)) between the experimental and the simulated diffusivities D/D_0 for simulations with HI for C_{poly} =1 %w/v. The particle diameter is $p = 1.5$ nm and the fiber diameter is $a = 0.8$ nm. (a) For high salt concentrations C_{Ion} between 180 and 210 mM, σ^2_{HI} is minimal for $b = 28$ nm. (b) For fixed $b = 28$ nm and C_{Ion} between 20 and 210 mM, the optimal potential strength is $U_0/k_BT = -7.5$ for the attractive case, while 4.5 follows from the charge ratio 5/3. The x-axis shows the attractive case potential strengths.

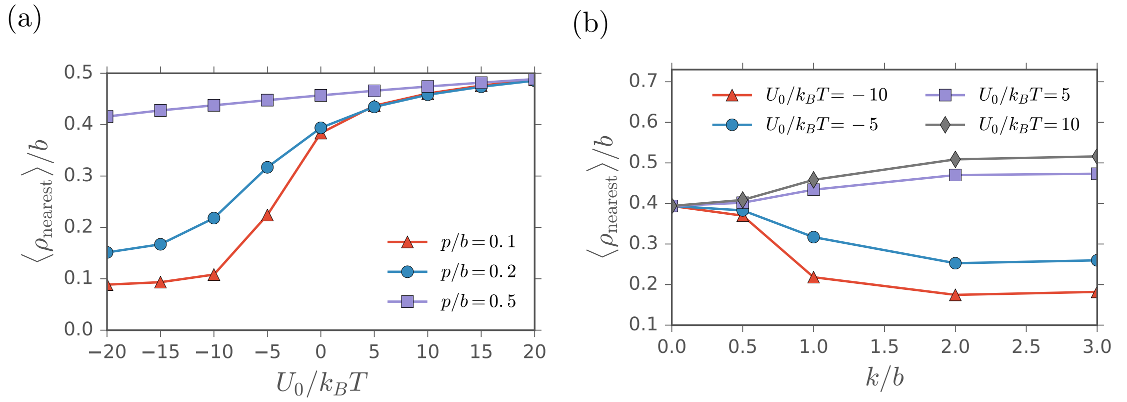

Figure 5.15. The mean distance $\langle\rho_{\mathrm{nearest}}\rangle$ of the particle to the nearest fibers averaged over the three planes xy, yz and zx for $a/b = 0.05$ as a function of the interaction strength U_0 for $k/b = 0.1$ (a) and of the interaction range for $p/b = 0.2$ (b). For attractive interaction potentials, $U_0 < 0$, the distance decreases and for repulsive interaction potentials the distance increases. The change in $\langle\rho_{\mathrm{nearest}}\rangle$ is anticorrelated with the change in the hydrodynamic effect in figs. 5.6a and 5.6b.

6. Summary and Outlook

In this thesis we present models for the diffusion of particles in hydrogels. We focus on the effect of exponentially screened particle-gel interactions on particle mobility inside gels. Such interactions form the basis for the experimentally observed phenomenon of interaction filtering, where particles are immobilized inside gels according to their surface chemistry. A particular focus is drawn on the asymmetric diffusive behavior with respect to the sign of the interactions. Furthermore, the effect of various other model parameters, such as particle versus mesh size, ionic strength, spatial disorder and interaction disorder are examined in detail. Quantitative comparisons to experiments are drawn for all models presented.

In chapters 2 and 3 we investigate particle diffusion in hydrogels with attractive or repulsive particle-gel interactions and varying degrees of spatial disorder. We observe highly asymmetric behavior with respect to the sign of the interaction; attractive particle-gel interactions normally lead to much stronger trapping of particles smaller than the mesh size than repulsive particle-gel interactions. While in purely steric gels disorder only weakly affects the diffusivity of particles smaller than the mesh size, spatial disorder becomes crucial for particle diffusion in the presence of long-range particle-gel interactions. The asymmetry with respect to the sign of the particle-gel interaction becomes more pronounced with increasing spatial disorder strength. The reason for this is that spatial disorder leads to the presence of regions with locally increased fiber density inside the gel. Therein, particles are strongly trapped in the presence of attractive particle-gel interactions. On the other hand, strong spatial disorder also creates abundant passageways of low fiber density. As a consequence, particles are relatively mobile in purely repulsive spatially disordered gels, even for strong repulsive interactions. A number of experimentally observed phenomena are naturally reproduced by our gel model: Size-filtering behavior observed in experiments [16], where a range of differently sized particles diffuse equally fast and only large particles are immobilized, occurs in simulations with repulsive particle-gel interactions in spatially ordered gels, since the particle can diffusive relatively freely between the repulsive fibers unless its diameter becomes larger than the mesh size. Anti-size filtering behavior [10], where small particles are hindered more strongly than larger particles, is reproduced in our simulations with spatially ordered attractive particle-gel interactions, since smaller particles move closer to the potential minima at the vertices of the fiber network. In experiments, increasing the polymer concentration has been observed to lead to an increase in particle diffusivity in the presence of attractive electrostatic particle-gel interactions [54]. Our simulations show that this is due to an increase in salt concentration upon addition of ionic polymers. In terms of electrostatic interactions, we find that charged particles always diffusive slower than neutral particles. Furthermore, electrostatic attraction strongly hinders particle mobility in the gel, whereas electrostatic repulsion has a much weaker effect. Favorable comparisons to experimental data for diffusion of

Alexa488 fluorophore in charged dextran gels confirm our theoretical results.

In chapter 4 we study diffusion in gels with mixed attractive and repulsive particle-gel interactions. Our model is primarily aimed at simulating diffusion in biogels which consist of functional groups with different biophysical properties. Our simulations show that attractive particle-gel interactions determine the diffusive behavior of the particle when randomly mixed attractive and repulsive interaction sites are present. The particle is trapped in regions with locally increased density of attractive fiber segments, qualitatively similar to diffusion in purely attractive gels. Our results affirm experimental findings showing that charged particles of either sign are immobilized in many biogels due to attractive electrostatic interactions with the polymer lattice, while charge-neutral particles diffuse rapidly. In collaboration with the group of Jason DeRouchey, we are able to show in theory and with experiments that already a small fraction of attractive interaction sites versus repulsive interaction sites leads to strong trapping of the particle.

Our results from chapters chapters 2 to 4 provide detailed insights into the microscopic transport mechanisms for particles in biopolymer networks. Due to the ubiquitous presence of polymer networks in biological systems our findings are relevant for medical science such as for the development of advanced drug delivery systems, e.g. with hydrogel based drug carrier systems, where it is important to know that through changes in ion concentration, the mobility of particles inside the gel carrier can be regulated. For the design of nanoparticles for targeted drug delivery our research shows that particles should ideally be charge neutral in order to rapidly overcome biogel barriers. In addition, our studies of the effect of spatial disorder and interaction disorder on the particle diffusivity can be used as a basis for future simulation studies on diffusion in crowded media.

In chapter 5 we investigate the effect of hydrodynamic interactions in combination with exponentially screened particle-gel interactions. Inclusion of hydrodynamics improves agreement between simulations and published experimental data. In fact, we achieve quantitative agreement to experimental data for diffusion in gels with electrostatic interactions as a function of the salt concentration, where previously only qualitative agreement was achieved without hydrodynamics. Repulsive particle-gel interactions decrease the effect of hydrodynamic interactions on the particle diffusivity compared to purely steric gels by reducing both far-field and near-field hydrodynamic interactions. Attractive particle-gel interactions, on the other hand, strongly increase the hydrodynamic effect on the diffusivity. This asymmetric behavior with respect to the sign of the interaction is due to the preferred positioning of the particle during the simulations. For repulsive interactions, the particle avoids the fibers, which reduces the hydrodynamic effect, whereas for attractive interactions the particle stays near the fibers, which increases the hydrodynamic effect. Lubrication corrections become practically negligible for small particles when strong exponentially screened particle-gel interactions are present. This is an interesting result for the design of simulation studies, since the inclusion of lubrication is computationally expensive. In future work, we could examine whether in a spatially disordered gel lubrication also becomes negligible for strongly attractive interactions, as is the case for spatially ordered gels. For gels with mixed interactions, we expect an increased hydrodynamic effect on the diffusivity similar to purely attractive gels, since as shown in chapter 4, attractive long-range interactions are dominant in gels with mixed interactions.

The exponential interaction potential employed in this work is used mostly to model electrostatic interaction due to the available experimental data to compare to our simulations. It would be interesting to model other types of interaction as well. In principle, our general interaction potential applies to any exponentially screened interaction. In particular for gels with mixed interactions one could investigate hydrophobic interactions in conjunction with electrostatics. Eperimental research indicates that the spatial configuration of charged monomers along a peptide chain has a significant impact on the peptide diffusivity in mucin gel [23]. In order to investigate the underlying mechanisms, our spatially disordered hydrogel model could be used to simulate the diffusion of charged peptides with various configurations of anionic and cationic monomers in charged gels.

A. Saddle-point potential

In order to obtain an analytic approximation for eq. (2.14), we first approximate the effective potential in eq. (2.13) by saddle point methods. For repulsive interactions, $U_0 > 0$, we expand the total interaction potential eq. (2.8) in y and z to first (nonzero) order around $y_0 = z_0 = 0.5b$,

$$\begin{aligned} U^{\mathrm{i}}(x,y,z) \approx U^{\mathrm{i}}(x,y_0,z_0) &+ \frac{(y-y_0)^2}{2}\partial_y^2 U^{\mathrm{i}}(x,y,z)|_{y_0,z_0} \\ &+ \frac{(z-z_0)^2}{2}\partial_z^2 U^{\mathrm{i}}(x,y,z)|_{y_0,z_0} \end{aligned} \tag{A.1}$$

and perform the integration in eq. (2.13). Shifting the integration boundaries to infinity, we obtain the Gaussian integral

$$\begin{aligned} &\int_0^b \mathrm{d}y \mathrm{e}^{-U^{\mathrm{i}}(x,y,z)/k_B T} \\ &\approx \int_{-\infty}^{\infty} \mathrm{d}y \mathrm{e}^{-[U^{\mathrm{i}}(x,y_0,z)+\frac{(y-y_0)^2}{2}\partial_y^2 U^{\mathrm{i}}(x,y,z)|_{y_0}]/k_B T} \\ &= \sqrt{\frac{2\pi k_B T}{\partial_y^2 U^{\mathrm{i}}(x,y,z)|_{y_0}}}\, e^{-U^{\mathrm{i}}(x,y_0,z)/k_B T} \,. \end{aligned} \tag{A.2}$$

Thus, we obtain the following analytic approximation for the effective potential for positive $U_0 > 0$

$$\begin{aligned} U_+(x) = U^{\mathrm{i}}(x,y_0,z_0) &+ \frac{k_B T}{2}\log[\partial_y^2 U^{\mathrm{i}}(x,y,z)/k_B T]_{y_0,z_0} \\ &+ \frac{k_B T}{2}\log[\partial_z^2 U^{\mathrm{i}}(x,y,z)/k_B T]_{y_0,z_0} \,, \end{aligned} \tag{A.3}$$

where we neglect an irrelevant constant. This approximate analytic expression for the effective potential has a minimum at $x_1^+ = 0.5b$ and a maximum at $x_2^+ = 0$, hence, for large U_0 and performing a second saddle-point approximation, we obtain from eq. (2.14)

$$\begin{aligned} \frac{D^+}{D_0} \approx & b^2 \left[\int_{-\infty}^{\infty} \mathrm{d}x\, \mathrm{e}^{[U_+(x_2^+)+\frac{(x-x_2^+)^2}{2}U_+''(x_2^+)]/k_B T} \right. \\ &\left. \times \int_{-\infty}^{\infty} \mathrm{d}x\, \mathrm{e}^{-[U_+(x_1^+)+\frac{(x-x_1^+)^2}{2}U_+''(x_1^+)]/k_B T} \right]^{-1} \\ = & b^2 \frac{\sqrt{-U_+''(x_1^+)\, U_+''(x_2^+)}}{2\pi k_B T} \mathrm{e}^{(U_+(x_1^+)-U_+(x_2^+))/k_B T} \,. \end{aligned} \tag{A.4}$$

Here, the prime represents a differentiation in x. The expressions for the derivatives of U and U_+ can be found in eqs. (A.10) to (A.14).

In the case of an attractive interaction potential ($U_0 < 0$) the first derivative of $U^{\mathrm{i}}(\vec{r})$ is not well defined at the potential minimum at $\vec{r} = (0,0,0)$. Hence, it is not possible to obtain a simple first-order approximation for U_{eff} for negative U_0 in the same way we did for $U_0 > 0$. Nevertheless, one can, in good approximation, write for $U_0 < 0$,

$$U_-(x) = U^{\mathrm{i}}(x,0,0)\ . \tag{A.5}$$

In fig. 2.4b one can see, that the potential along the edge of the simulation box resembles the shape of the effective potential U_{eff} in the attractive case quite closely. To establish an analytical expression for the relative diffusivity we again expand the effective potential around its maximum at $x_2^- = 0.5b$ and its minimum at $x_1^- = 0$, where special care has to be taken for the latter:

$$U_-(x) \approx U_-(0) + x\,U_-'(0+)\ , \quad x > 0\ . \tag{A.6}$$

Hence, we obtain

$$\begin{aligned}\frac{D^-}{D_0} \approx & b^2 \left[\int_{-\infty}^{\infty} \mathrm{d}x \mathrm{e}^{[U_-(x_2^-)+\frac{(x-x_2^-)^2}{2}U_-''(x_2^-)]/k_BT} \right.\\ & \left. \times 2\int_0^{\infty} \mathrm{d}x \mathrm{e}^{-[U_-(x_1^-)+(x-x_1^-)\lim_{x\searrow x_1^-} U_-'(x)]/k_BT}\right]^{-1}\\ = & b^2 \sqrt{\frac{-U_-''(x_2^-)}{2\pi k_BT}}\,\frac{U_-'(x_1^-)}{2k_BT}\,\mathrm{e}^{(U_-(x_1^-)-U_-(x_2^-))/k_BT}\ .\end{aligned} \tag{A.7}$$

The expressions for the derivatives of U_- can be found below. Figure 2.4 shows a sketch of the potentials U_-, U_+, U_{eff} and $U^{\mathrm{i}}(x,0.5b,0.5b)$.

The full expressions for the parameters c_- and c_+ are

$$c_+ = 2\sum_{m,n=1-l}^{l}\left(\mathrm{e}^{\frac{-b\sqrt{(0.5-m)^2+(0.5-n)^2}}{k}} - \mathrm{e}^{\frac{-b\sqrt{(0.5-n)^2+m^2}}{k}}\right) \tag{A.8}$$

$$c_- = 2\sum_{m,n=1-l}^{l}\left(\mathrm{e}^{\frac{-b\sqrt{m^2+n^2}}{k}} - \mathrm{e}^{\frac{-b\sqrt{(0.5-n)^2+m^2}}{k}}\right)\ , \tag{A.9}$$

where l equals 1 in the case of a first order or 2 in the case of a second order summation of adjacent rods.

The derivatives of the interaction potential are

$$\begin{aligned}\partial_z U(\vec{r}) =& U_0 \sum_{q=x,y} \sum_{m,n} \mathrm{e}^{-\rho_{m,n}(q,z)/k} \\ & \times \left[-\frac{(z-mb)}{k\rho_{m,n}(q,z)} \right] , \end{aligned} \tag{A.10}$$

$$\begin{aligned}\partial_z^2 U(\vec{r}) =& U_0 \sum_{q=x,y} \sum_{m,n} \mathrm{e}^{-\rho_{m,n}(q,z)/k} \\ & \times \left[\frac{(z-mb)^2}{k^2\rho_{m,n}^2(q,z)} - \frac{(q-nb)^2}{k\rho_{m,n}^3(q,z)} \right] , \end{aligned} \tag{A.11}$$

$$\lim_{x\searrow x_1^-=0} U'_-(x) = -\frac{U_0}{k} , \tag{A.12}$$

$$U''_+(x) = \partial_x^2 U(x,y_0,z_0) + \left. \frac{\partial_x^2 \partial_z^2 U(x,y,z)}{\partial_z^2 U(x,y,z)} \right|_{y_0,z_0} \tag{A.13}$$

where $\rho_{m,n}(q,z) = \sqrt{(q-nb)^2 + (z-mb)^2}$ and

$$\begin{aligned} \partial_x^2 \partial_z^2 U(\vec{r}) = U_0 \sum_{m,n} \frac{1}{k^4} \mathrm{e}^{-\frac{\rho}{k}} \\ \times \Bigg(\left[\frac{k}{\rho^5} - \frac{(x-nb)^2}{\rho^6} - \frac{5k(x-nb)^2}{\rho^7} \right] \\ \times \big[k^2\big(\rho^2 - 3(z-mb)^2\big) - \rho^2(z-mb)^2 \\ + k\rho\big(\rho^2 - 3(z-mb)^2\big) \big] \\ + \frac{k(x-nb)^2}{\rho^6} \big[2k^2\rho + 3k(x-nb)^2 - 2(z-mb)^2\rho \big] \Bigg) . \end{aligned} \tag{A.14}$$

Here, ρ is a short-hand notation for $\rho_{m,n}(x,z)$.

B. Modified Stokesian dynamics method

The Stokesian Dynamics method allows to calculate HI in a suspension of spheres based on the pairwise additivity of forces and velocities. For widely spaced spheres, far-field HI can be efficiently calculated based on far-field mobilities using the additivity of solvent velocities, since corrections scale as $O(1/r^4)$ with distance r, in contrast to a summation of resistances, where corrections scale as $O(1/r^2)$ [94]. On the other hand, lubrication forces, i.e. near-field HI that are important for closely spaced spheres, must be accounted for via pairwise addition of forces in the resistance picture [94]. Thus, the Stokesian dynamics method entails both the calculation of far-field HI by adding mobilities and near-field HI by adding resistances. In the following, we will briefly outline the necessary steps.

In the first step, one calculates the $3(N+1)\times 3(N+1)$ far-field mobility matrix

$$\mathbf{M}^{\mathrm{pbc}} \cdot \vec{F} = \vec{V} \ ,$$

$$\mathbf{M}^{\mathrm{pbc}} = \begin{pmatrix} \mathbf{M}^{\mathrm{pbc}}_{00} & \mathbf{M}^{\mathrm{pbc}}_{01} & \dots & \mathbf{M}^{\mathrm{pbc}}_{0N} \\ \mathbf{M}^{\mathrm{pbc}}_{10} & & & \\ \vdots & & & \\ \mathbf{M}^{\mathrm{pbc}}_{N0} & & & \mathbf{M}^{\mathrm{pbc}}_{NN} \end{pmatrix} . \tag{B.1}$$

Here, $\vec{F} = (\vec{F}_0, \vec{F}_1, ..., \vec{F}_i, ..., \vec{F}_N)$ is the vector of forces that act on a collection of particles, $i = 1, .., N$ is the index of the N spheres comprising the fibers and the index 0 denotes the diffusing particle. $\vec{V} = (\vec{v}_0, ..., \vec{v}_N)$ is a vector of all solute velocities. The mobility matrix $\mathbf{M}^{\mathrm{pbc}}$ includes only far-field HI, which are calculated for periodic boundary conditions (pbc) using the Ewald sum of the Rotne-Prager (RP) tensor. The details of this calculation are given in appendix C. Next, the far-field mobility matrix $\mathbf{M}^{\mathrm{pbc}}$ is inverted and we move into the resistance picture. Through inversion of $\mathbf{M}^{\mathrm{pbc}}$ all two-particle far-field HI and their reflections are summed. This leads to a many-body approximation of the far-field resistance matrix that reproduces the screening behavior characteristic of a porous medium [94]. In step two, we include lubrication by adding near-field two-particle HI to the far-field self-resistance matrix of the particle according to

$$\mathbf{R}_{\mathrm{self}} = (\mathbf{M}^{\mathrm{pbc}})^{-1}_{00} + \mathbf{R}^{\mathrm{lub}} \ . \tag{B.2}$$

We obtain $\mathbf{R}^{\mathrm{lub}}$ by calculating the two-particle resistance matrix according to Jeffrey and Onishi [98] and subsequently subtracting the far-field HI that are already included in $(\mathbf{M}^{\mathrm{pbc}})^{-1}$. The details of this procedure are outlined in appendix D. Finally, in step 3, one inverts the self-resistance of the particle $\mathbf{R}_{\mathrm{self}}$ to obtain the self-mobility tensor of the particle

$$\mathbf{M}_{\mathrm{self}} = (\mathbf{R}_{\mathrm{self}})^{-1} \ . \tag{B.3}$$

Inverting only the particle resistance matrix corresponds to setting the velocity of all the fiber spheres to zero, i.e. fixing their positions.

C. Ewald sum of the Rotne-Prager tensor

To implement the Ewald sum of the Rotne-Prager tensor in the presence of periodic boundary conditions we follow the description in the original 1986 paper by Beenakker [96]. We use the RP tensor for two spheres of unequal diameter [96], such that

$$\mathbf{M}^{\mathrm{RP}}(\vec{r}_{ij}) = \begin{cases} \left(1 + \frac{a_i^2+a_j^2}{24}\nabla^2\right)\mathbf{T}_0(\vec{r}_{ij}) & \text{if } i \neq j \; , \\ \frac{\mathbf{1}}{3\pi\eta a_i} & \text{if } i = j \; , \end{cases} \tag{C.1}$$

where

$$\mathbf{T}_0(\vec{r}) = \frac{1}{8\pi\eta r}(\mathbf{1} + \hat{r}\hat{r}) \tag{C.2}$$

is the Oseen tensor, a_i and a_j are the diameters of particle i and j and $\hat{r}_{ij} = \vec{r}_{ij}/r_{ij}$ is the unit vector along the interparticle axis. The far-field mobility matrix $\mathbf{M}^{\mathrm{pbc}}$ consists of submatrices of the form [96]

$$\begin{aligned} 3\pi\eta a_i\,\mathbf{M}_{ij}^{\mathrm{pbc}}(\vec{r}_{ij}) = {} & 3\pi\eta a_i \sum_{\vec{n}} \mathbf{M}^{\mathrm{RP}}(\vec{r}_{ij,\vec{n}}) \\ \approx {} & \mathbf{1}\left(1 - \frac{a_i}{2}\frac{6\alpha}{\sqrt{\pi}} + \frac{a_i}{2}\frac{40\bar{a}^2\alpha^3}{3\sqrt{\pi}}\right)\delta_{ij} \\ & + \sum_{\substack{\vec{n} \\ \vec{r}_{ij,\vec{n}}\neq 0}}^{r_{ij,\vec{n}}<r_c} \mathbf{M}^{(1)}(\vec{r}_{ij,\vec{n}}) + \sum_{\vec{k_r}\neq 0}^{k_r<k_c} \mathbf{M}^{(2)}(\vec{k_r})\cos(\vec{k_r}\cdot\vec{r}_{ij}) \; , \end{aligned} \tag{C.3}$$

where $\bar{a} = (a_i + a_j)/4$ and $\vec{r}_{ij,\vec{n}} = \vec{r}_j - \vec{r}_i + \vec{n}b$ with b being the unit cell width and the lattice vector $\vec{n} = (n_x, n_y, n_z)$. The vector $\vec{k_r} = 2\pi\vec{n}/b$ is the lattice vector in reciprocal space. r_c and k_c are the cutoffs for the sums, defined below. The summation is split into two rapidly converging sums over $\mathbf{M}^{(1)}$ in real space and over $\mathbf{M}^{(2)}$ in reciprocal space. The real space sum covers the near-field contributions and the reciprocal space sum the far-field contributions of the periodic lattice. The respective expressions are [96]

$$\begin{aligned} \mathbf{M}^{(1)}(\vec{r}) = {} & \mathbf{1}\,\frac{a_i}{2}\left[\mathrm{erfc}(\alpha r)\left(\frac{3}{4r} + \frac{\bar{a}^2}{2r^3}\right)\right. \\ & \left. + \frac{\exp(-\alpha^2 r^2)}{\sqrt{\pi}}\left(3\alpha^3 r^2 - \frac{9\alpha}{2} + 4\bar{a}^2\alpha^7 r^4 - 20\bar{a}^2\alpha^5 r^2 + 14\bar{a}^2\alpha^3 + \frac{\bar{a}^2\alpha}{r^2}\right)\right] \\ & + \hat{r}\hat{r}\,\frac{a_i}{2}\left[\mathrm{erfc}(\alpha r)\left(\frac{3}{4r} - \frac{3\bar{a}^2}{2r^3}\right)\right. \\ & \left. + \frac{\exp(-\alpha^2 r^2)}{\sqrt{\pi}}\left(\frac{3\alpha}{2} - 3\alpha^3 r^2 - 4\bar{a}^2\alpha^7 r^4 + 16\bar{a}^2\alpha^5 r^2 - 2\bar{a}^2\alpha^3 - \frac{3\bar{a}^2\alpha}{r^2}\right)\right] \; , \end{aligned} \tag{C.4}$$

where erfc denotes the complementary error function, and

$$\mathbf{M}^{(2)}(\vec{k_r}) = \frac{a_i}{2}\left(\mathbf{1} - \hat{k_r}\hat{k_r}\right)\left(1 - \frac{\bar{a}^2 k_r^2}{3}\right)\left(1 + \frac{k_r^2}{4\alpha^2} + \frac{k_r^4}{8\alpha^4}\right)\frac{6\pi}{k_r^2 b^3}\exp\left(\frac{-k_r^2}{4\alpha^2}\right) . \tag{C.5}$$

The parameter α is a weighting factor that determines the rate of convergence of the two sums. It is set to $\alpha = \sqrt{\pi}/b$ [96], such that both sums are weighted equally, i.e. the computational burden is distributed equally between both sums.

For the implementation of the two sums, a cutoff distance has to be set that determines the accuracy and speed of the simulations. According to Jain and coworkers [43] an appropriate cutoff distance r_c for the real space sum should be chosen such that $\exp(-\alpha^2 r_c^2)$ in eq. (C.4) is very small. The reciprocal space sum in eq. (C.5) is weighted by the factor $\exp(-k_r^2/4\alpha^2)$. Hence, the appropriate cutoff for the reciprocal space sum k_c follows from the condition $-k_c^2/4\alpha^2 = -\alpha^2 r_c^2$ as $k_c = 2\alpha^2 r_c$.

D. Lubrication approximation

The two-particle resistance matrix in low-Reynolds-number flow, neglecting torque, can be expressed as

$$\begin{pmatrix} \vec{F}_1 \\ \vec{F}_2 \end{pmatrix} = \eta \begin{pmatrix} \mathbf{R}_{11}^{2\mathrm{P}} & \mathbf{R}_{12}^{2\mathrm{P}} \\ \mathbf{R}_{21}^{2\mathrm{P}} & \mathbf{R}_{22}^{2\mathrm{P}} \end{pmatrix} \cdot \begin{pmatrix} \vec{v}_1 \\ \vec{v}_2 \end{pmatrix} , \tag{D.1}$$

where $\mathbf{R}^{2\mathrm{P}}$ is the two-particle resistance matrix for two hydrodynamically interacting spheres. According to Jeffrey and Onishi [98], the 3×3 submatrices can be expressed as

$$\mathbf{R}_{ij}^{2\mathrm{P}} = \hat{r}\hat{r}\,(X_{ij} - Y_{ij}) + \mathbf{1}X_{ij} , \tag{D.2}$$

where X_{ij} and Y_{ij} are scalar functions that both depend on the rescaled variables $\lambda = a_2/a_1$ and $s = 4r/(a_1+a_2)$. Here, r is the distance between the two spheres. For our simulations, we only require the 3×3 self-mobility matrix of the particle, which is the inverse of the 3×3 resistance submatrix $\mathbf{R}_{\mathrm{self}}$, as shown in eq. (B.3), which becomes

$$\mathbf{R}_{\mathrm{self}} = (\mathbf{M}^{\mathrm{pbc}})_{00}^{-1} + \sum_{j=1}^{N} \left(\mathbf{R}_{11}^{2\mathrm{P}}(s_j, \lambda) - (\mathbf{M}^{\mathrm{RP}}(\vec{r}_{0j}))_{00}^{-1} \right) , \tag{D.3}$$

where s_i is the rescaled distance between the particle and fiber sphere j and $(\mathbf{M}^{\mathrm{RP}})^{-1}$ is the inverse of the 6×6 two-particle RP matrix (c.f. eq. (C.1)). The lubrication approximation corresponds to the second part of eq. (D.3):

$$\mathbf{R}^{\mathrm{lub}} = \sum_{j=1}^{N} \left(\mathbf{R}_{11}^{2\mathrm{P}}(s_j, \lambda) - (\mathbf{M}^{\mathrm{RP}}(\vec{r}_{0j}))_{00}^{-1} \right) . \tag{D.4}$$

To determine the $\mathbf{R}_{11}^{2\mathrm{P}}(s, \lambda)$ terms for the two-particle interaction between the diffusing particle and all N fiber spheres the scalar functions are given by Jeffrey and Onishi [98] as

$$\begin{aligned} X_{11}(s,\lambda) =& g_1(\lambda)(1-4s^{-2})^{-1} - g_2(\lambda)\ln(1-4s^{-2}) - g_3(\lambda)(1-4s^{-2})\ln(1-4s^{-2}) \\ & - g_1(\lambda) + f_0^X(\lambda) + \sum_{\substack{m=2 \\ m \text{ even}}} \left[\frac{f_m^X(\lambda)}{2^m(1+\lambda)^m} - g_1(\lambda) - \frac{2g_2(\lambda)}{m} + \frac{4g_3(\lambda)}{mt(m)} \right] \left(\frac{2}{s}\right)^m , \end{aligned} \tag{D.5}$$

where the auxiliary functions are defined as

$$
\begin{aligned}
g_1(\lambda) =& 2\lambda^2(1+\lambda)^{-3} \;, && \text{(D.6)}\\
g_2(\lambda) =& \frac{1}{5}\lambda(1+7\lambda+\lambda^2)(1+\lambda)^{-3} \;, && \text{(D.7)}\\
g_3(\lambda) =& \frac{1}{42}(1+18\lambda-29\lambda^2+18\lambda^3+\lambda^4)(1+\lambda)^{-3}, && \text{(D.8)}\\
t(m) =& -2\delta_{m2}+(m-2) \;. && \text{(D.9)}
\end{aligned}
$$

and

$$
\begin{aligned}
Y_{11}(s,\lambda) =& -g_4(\lambda)\ln(1-4s^{-2}) - g_5(\lambda)(1-4s^{-2})\ln(1-4s^{-2}) + f_0^Y(\lambda)\\
&+ \sum_{\substack{m=2\\ m\text{ even}}} \left[\frac{f_m^Y(\lambda)}{2^m(1+\lambda)^m} - \frac{2g_4(\lambda)}{m} + \frac{4g_5(\lambda)}{mt(m)}\right]\left(\frac{2}{s}\right)^m \;, \qquad \text{(D.10)}
\end{aligned}
$$

with

$$
\begin{aligned}
g_4(\lambda) =& \frac{4}{15}\lambda(2+\lambda+2\lambda^2)(1+\lambda)^{-3} \;, && \text{(D.11)}\\
g_5(\lambda) =& \frac{2}{375}(16-45\lambda+58\lambda^2-45\lambda^3+16\lambda^4)(1+\lambda)^{-3} \;. && \text{(D.12)}
\end{aligned}
$$

For a listing of the f_m^X and f_m^Y functions we refer to the original manuscript [98]. For the sums in eqs. (D.5) and (D.10) a cutoff of $m_{\max} = 12$ is employed. A larger value for $m_{\max}$ leads only to marginal differences in X_{11} and Y_{11} of less than one percent.

Inverting the 6×6 two-particle RP matrix $\mathbf{M}^{\mathrm{RP}}$ in eq. (D.3) for all N spheres at every iteration step would be computationally extremely costly. To avoid this, we fit the inverted RP submatrix $(\mathbf{M}^{\mathrm{RP}})^{-1}_{00}$ in the beginning of each simulation and use the resulting fit function to calculate eq. (D.3). As fit function, we use

$$
(\mathbf{M}^{\mathrm{RP}})^{-1}_{00} = \sum_{n=0}^{7}\left(\frac{c_n}{s^n}\mathbf{1} + \frac{d_n}{s^n}\hat{r}\hat{r}\right) , \qquad \text{(D.13)}
$$

where c_n and d_n are fit parameters. A cutoff $n = 5$ of the sum in eq. (D.13) leads to almost perfect agreement between the inverted RP and the fit result. In our calculations, we employ the larger cutoff of $n = 7$. An exemplary fit result is presented in fig. D.1.

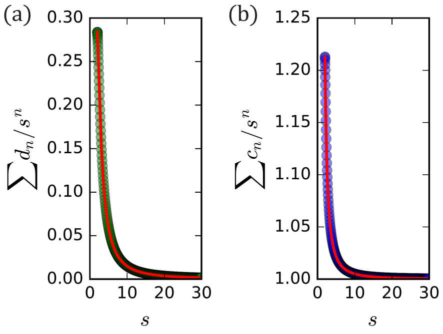

Figure D.1. Fit of eq. (D.13) (*red lines*) to $(\mathbf{M}^{\mathrm{RP}})^{-1}_{00}$ over the rescaled distance s for an arbitrarily chosen ratio $\lambda = 0.5$. The filled circles are the fit data points obtained by numerically inverting $\mathbf{M}^{\mathrm{RP}}$ (eq. (C.1)) for two particles at different distances. (a) The result of fitting the second sum in eq. (D.13), i.e. the prefactors d_n, (b) the result of fitting the first sum in eq. (D.13), i.e. the prefactors c_n.

E. Mid-point-scheme

The modified mid-point scheme by Bancho and Brady [44] is fast and readily implemented into the existing code. First one calculates the velocity without drift for the particle at the current position $\vec{r}^0$,

$$\vec{v}^0 = \vec{v}(\vec{r}^0) = (\mathbf{R}^0)^{-1} \cdot (\vec{F}^0 + \vec{F}_R^0) \ . \tag{E.1}$$

Next, one moves the particle to an intermediate position $\vec{r}'$ in direction of $\vec{v}^0$

$$\vec{r}' = \vec{r}^0 + \vec{v}^0 \, \Delta t' \ , \tag{E.2}$$

where $\Delta t' = \frac{\Delta t}{m}$ is a fraction of the timestep, i.e. $m = 200$ in our simulations. Subsequently, the drift velocity is approximated by

$$\vec{\nabla} \cdot (\mathbf{R}_{\text{self}})^{-1} = \frac{\Delta t}{2\Delta t'} \left((\mathbf{R}')^{-1} - (\mathbf{R}^0)^{-1} \right) \cdot (\vec{F}^0 + \vec{F}_R^0) \ , \tag{E.3}$$

where $\mathbf{R}'$ is the resistance matrix at the intermediate position $\vec{r}'$. Finally, according to eq. (3.1), the particle is moved to a new position

$$\vec{r} = \vec{r}^0 + \left(\vec{v}^0 + \vec{\nabla} \cdot (\mathbf{R}_{\text{self}})^{-1} \right) \Delta t \ . \tag{E.4}$$

F. Precomputing the far-field mobility matrix

A common method to decrease the computational cost is to only reevaluate the far-field HI if the particle has moved further than a certain threshold distance since the last evaluation. The threshold distance has to be sufficiently small, such that the far-field HI will have changed very little. In our simulations, we use a different approach. We calculate the inverse of the far-field mobility matrix $(\mathbf{M}^{\text{pbc}})^{-1}$ at each point on a regularly spaced $40 \times 40 \times 40$ grid in the cubic lattice cell with side length b (c.f. section 5.1.1). Thus, the separation of the grid points is $b/40 = 0.025b$. We store the 3×3 submatrix $(\mathbf{M}^{\text{pbc}})^{-1}_{00}$ needed for the calculation of the particle self-lubrication $\mathbf{R}_{\text{self}}$ (c.f. eq. (D.3)) in a lookup table. When the particle moves inside the periodic cell during the simulation, we use the precomputed far-field HI at the grid point nearest to the particle position to calculate eq. (D.3). For the inversion of the mobility matrix an iterative conjugate gradient method is employed, which supplies a reliable and fast matrix inversion. Since we precompute the Ewald summed far-field HI, we can choose a very large cutoff $r_c = 8b$ (c.f. appendix C) without adding much computational cost.

G. Hydrodynamic friction during trapping and barrier crossing

To determine when the particle is trapped at a vertex, or when it is in the process of crossing the barrier between two vertices, we examine the particle trajectory. We define a barrier crossing event if the particle moves further than a distance of $d = (p + a)$ away from a vertex *and* does not return to the same vertex. An example particle trajectory with multiple trapping and barrier crossing events is shown in fig. G.1a. A close up of a barrier crossing event is presented in fig. G.1b. The average diffusion coefficients $\langle D' \rangle$ in fig. 5.8 are calculated by separately averaging the diagonal elements of the particle self-mobility matrix during trapping (c.f. fig. G.1b, black circles) and during barrier crossing (c.f. fig. G.1b, red circles).

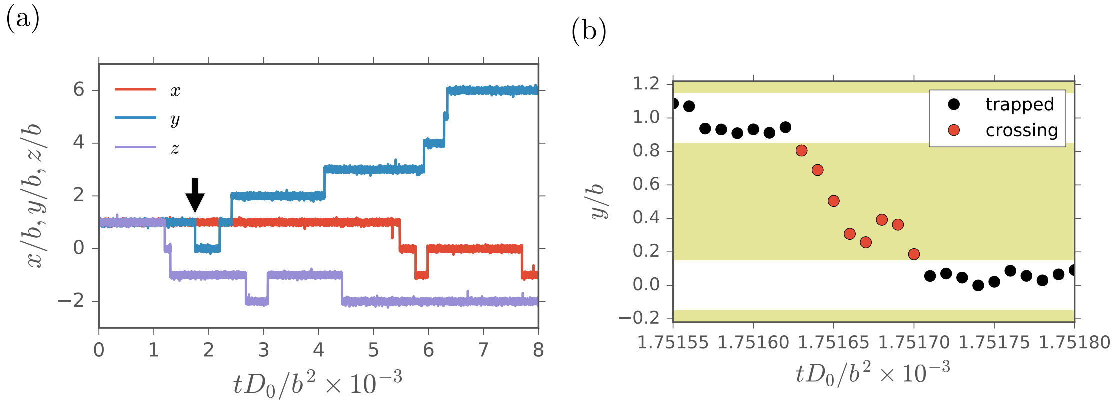

Figure G.1. (a) Three dimensional trajectory for a particle with a diameter of $p/b = 0.1$ for a strongly attractive interaction potential $U_0/k_BT = -15$, $k/b = 0.1$ and with full HI. The particle experiences trapping at the lattice vertices (positioned at integer values of x/b, y/b, z/b) for most of the time and intermittently crosses between adjacent vertices. The black arrow in (a) indicates the barrier crossing in y-direction shown in detail in (b). The colored regions in (b) indicate where the distance to the vertex is less than $a + p$ in y-direction.

List of Publications

The present thesis is based on the following manuscripts, which have been published in peer-reviewed journals:

[i] Xiaolu Zhang, Johann Hansing, Roland R. Netz, and Jason E. DeRouchey, ”Particle Transport through Hydrogels Is Charge Asymmetric,” *Biophysical Journal*, vol. 108, pp. 530-9, 2015, DOI: https://doi.org/10.1016/j.bpj.2014.12.009

[ii] Johann Hansing, Catrin Ciemer, Won Kyu Kim, Xiaolu Zhang, Jason E. DeRouchey, and Roland R. Netz, ”Nanoparticle filtering in charged hydrogels: Effects of particle size, charge asymmetry and salt concentration,” *The European Physical Journal E*, vol. 39, p. 53, 2016, DOI: https://doi.org/10.1140/epje/i2016-16053-2

[iii] Johann Hansing and Roland R. Netz, ”Particle Trapping Mechanisms are Different in Spatially Ordered and Disordered Interacting Gels”, *Biophysical Journal*, vol. 114, pp. 2653 - 2664, 2018, DOI: https://doi.org/10.1016/j.bpj.2018.04.041

[iv] Johann Hansing, Joseph R. Duke III, Emily B. Fryman, Jason E. DeRouchey and Roland R. Netz, ”Particle Diffusion in Polymeric Hydrogels with Mixed Attractive and Repulsive Interactions”, *Nano Letters*, vol. 18, pp. 5248-5256, 2018, DOI: https://doi.org/10.1021/acs.nanolett.8b02218

[v] Johann Hansing and Roland R. Netz, ”Hydrodynamic Effects on Particle Diffusion in Polymeric Hydrogels with Steric and Electrostatic Particle-Gel Interactions”, *Macromolecules*, 2018, DOI: https://doi.org/10.1021/acs.macromol.8b01494

Bibliography

[1] O. Lieleg and K. Ribbeck, “Biological hydrogels as selective diffusion barriers.,” *Trends in Cell Biology*, vol. 21, pp. 543–51, Sept. 2011.

[2] S. Lai, Y. Wang, and J. Hanes, “Mucus-penetrating nanoparticles for drug and gene delivery to mucosal tissues,” *Advanced drug delivery reviews*, vol. 61, no. 2, pp. 158–171, 2009.

[3] S. Dünnhaupt, O. Kammona, C. Waldner, C. Kiparissides, and A. Bernkop-Schnürch, “Nano-carrier systems: Strategies to overcome the mucus gel barrier,” *European Journal of Pharmaceutics and Biopharmaceutics*, vol. 96, pp. 447–453, 2015.

[4] J. Shin, A. G. Cherstvy, and R. Metzler, “Sensing viruses by mechanical tension of dna in responsive hydrogels,” *Physical Review X*, vol. 4, p. 021002, Apr. 2014.

[5] E. Wischerhoff, N. Badi, J.-F. Lutz, and A. Laschewsky, “Smart bioactive surfaces,” *Soft Matter*, vol. 6, pp. 705–713, Feb. 2010.

[6] A. Vashist, A. Vashist, Y. K. Gupta, and S. Ahmad, “Recent advances in hydrogel based drug delivery systems for the human body,” *Journal of Materials Chemistry B*, vol. 2, p. 147, Dec. 2014.

[7] W. Hennink, H. Talsma, J. Borchert, S. De Smedt, and J. Demeester, “Controlled release of proteins from dextran hydrogels,” *Journal of Controlled Release*, vol. 39, no. 1, pp. 47–55, 1996.

[8] J. Kirch, A. Schneider, B. Abou, A. Hopf, U. F. Schaefer, M. Schneider, C. Schall, C. Wagner, and C.-M. Lehr, “Optical tweezers reveal relationship between microstructure and nanoparticle penetration of pulmonary mucus.,” *Proceedings of the National Academy of Sciences of the United States of America*, vol. 109, pp. 18355–60, Nov. 2012.

[9] T. Stylianopoulos, B. Diop-Frimpong, L. L. Munn, and R. K. Jain, “Diffusion anisotropy in collagen gels and tumors: the effect of fiber network orientation.,” *Biophysical Journal*, vol. 99, pp. 3119–28, Nov. 2010.

[10] S. K. Lai, D. E. O’Hanlon, S. Harrold, S. T. Man, Y.-Y. Wang, R. Cone, and J. Hanes, “Rapid transport of large polymeric nanoparticles in fresh undiluted human mucus,” *Proceedings of the National Academy of Sciences of the United States of America*, vol. 104, no. 5, pp. 1482–1487, 2007.

[11] F. Arends, R. Baumgärtel, and O. Lieleg, “Ion-specific effects modulate the diffusive mobility of colloids in an extracellular matrix gel.,” *Langmuir : the ACS journal of surfaces and colloids*, vol. 29, pp. 15965–73, Dec. 2013.

[12] W. M. Saltzman, M. L. Radomsky, K. J. Whaley, and R. A. Cone, “Antibody diffusion in human cervical mucus.,” *Biophysical Journal*, vol. 66, pp. 508–15, Feb. 1994.

[13] R. Cone, “Barrier properties of mucus,” *Advanced drug delivery reviews*, vol. 61, no. 2, pp. 75–85, 2009.

[14] O. Lieleg, I. Vladescu, and K. Ribbeck, “Characterization of particle translocation through mucin hydrogels,” *Biophysical Journal*, vol. 98, pp. 1782–9, May 2010.

[15] Y. Cu and W. M. Saltzman, “Mathematical modeling of molecular diffusion through mucus,” *Advanced Drug Delivery Reviews*, vol. 61, no. 2, pp. 101–114, 2009.

[16] Q. Xu, N. J. Boylan, J. S. Suk, Y.-Y. Wang, E. A. Nance, J.-C. Yang, P. J. McDonnell, R. A. Cone, E. J. Duh, and J. Hanes, “Nanoparticle diffusion in, and microrheology of, the bovine vitreous ex vivo,” *Journal of Controlled Release*, vol. 167, no. 1, pp. 76–84, 2013.

[17] B. T. Käsdorf, F. Arends, and O. Lieleg, “Diffusion regulation in the vitreous humor.,” *Biophysical Journal*, vol. 109, pp. 2171–81, Nov. 2015.

[18] L. Rusu, D. Lumma, and J. O. Rädler, “Charge and size dependence of liposome diffusion in semidilute biopolymer solutions.,” *Macromolecular Bioscience*, vol. 10, pp. 1465–72, Dec. 2010.

[19] A. Birjiniuk, N. Billings, E. Nance, J. Hanes, K. Ribbeck, and P. S. Doyle, “Single particle tracking reveals spatial and dynamic organization of the escherichia coli biofilm matrix,” *New Journal of Physics*, vol. 16, no. 8, p. 085014, 2014.

[20] R. G. Thorne, A. Lakkaraju, E. Rodriguez-Boulan, and C. Nicholson, “In vivo diffusion of lactoferrin in brain extracellular space is regulated by interactions with heparan sulfate.,” *Proceedings of the National Academy of Sciences of the United States of America*, vol. 105, pp. 8416–21, June 2008.

[21] O. Lieleg, R. Baumgärtel, and A. Bausch, “Selective filtering of particles by the extracellular matrix: an electrostatic bandpass,” *Biophysical Journal*, vol. 97, pp. 1569–77, Sept. 2009.

[22] J. S. Crater and R. L. Carrier, “Barrier properties of gastrointestinal mucus to nanoparticle transport,” *Macromolecular Bioscience*, vol. 10, pp. 1473–1483, Dec. 2010.

[23] L. D. Li, T. Crouzier, A. Sarkar, L. Dunphy, J. Han, and K. Ribbeck, “Spatial configuration and composition of charge modulates transport into a mucin hydrogel barrier,” *Biophysical Journal*, vol. 105, no. 6, pp. 1357–1365, 2013.

[24] F. Laffleur, F. Hintzen, G. Shahnaz, D. Rahmat, K. Leithner, and A. Bernkop-Schnürch, "Development and in vitro evaluation of slippery nanoparticles for enhanced diffusion through native mucus," *Nanomedicine*, vol. 9, pp. 387–396, Mar. 2014.

[25] A. G. Ogston, "The spaces in a uniform random suspension of fibres," *Transactions of the Faraday Society*, vol. 54, p. 1754, Jan. 1958.

[26] R. J. Phillips, W. M. Deen, and J. F. Brady, "Hindered transport of spherical macromolecules in fibrous membranes and gels," *AIChE Journal*, vol. 35, pp. 1761–1769, Nov. 1989.

[27] R. J. Phillips, W. M. Deen, and J. F. Brady, "Hindered transport in fibrous membranes and gels: Effect of solute size and fiber configuration," *Journal of Colloid and Interface Science*, vol. 139, pp. 363–373, Oct. 1990.

[28] B. Amsden, "Solute diffusion within hydrogels. mechanisms and models," *Macromolecules*, vol. 31, pp. 8382–8395, Nov. 1998.

[29] R. J. Phillips, "A hydrodynamic model for hindered diffusion of proteins and micelles in hydrogels.," *Biophysical Journal*, vol. 79, pp. 3350–3, Dec. 2000.

[30] L. Johansson, C. Elvingson, and J. E. Löfroth, "Diffusion and interaction in gels and solutions. 3. theoretical results on the obstruction effect," *Macromolecules*, vol. 24, pp. 6024–6029, Oct. 1991.

[31] L. Johansson and J.-E. Löfroth, "Diffusion and interaction in gels and solutions. 4. hard sphere Brownian dynamics simulations," *The Journal of Chemical Physics*, vol. 98, p. 7471, May 1993.

[32] P. A. Netz and T. Dorfmüller, "Computer simulation studies of diffusion in gels: Model structures," *The Journal of Chemical Physics*, vol. 107, p. 9221, Dec. 1997.

[33] H. Masoud and A. Alexeev, "Permeability and diffusion through mechanically deformed random polymer networks," *Macromolecules*, vol. 43, pp. 10117–10122, Dec. 2010.

[34] T. Stylianopoulos, M.-Z. Poh, N. Insin, M. G. Bawendi, D. Fukumura, L. L. Munn, and R. K. Jain, "Diffusion of particles in the extracellular matrix: the effect of repulsive electrostatic interactions.," *Biophysical Journal*, vol. 99, pp. 1342–9, Sept. 2010.

[35] P. Licinio and A. Teixeira, "Anomalous diffusion of ideal polymer networks," *Physical Review E*, vol. 56, pp. 631–634, July 1997.

[36] H. Zhou and S. Chen, "Brownian dynamics simulation of tracer diffusion in a cross-linked network," *Physical Review E*, vol. 79, p. 021801, Feb. 2009.

[37] T. Miyata, A. Endo, and T. Ohmori, “Brownian dynamics simulation study of self-diffusion of a charged particle in swollen counter-charged hydrogel modeled as cubic lattice,” *Journal of Chemical Engineering of Japan*, vol. 35, no. 7, pp. 640–648, 2002.

[38] T. Miyata, “Brownian dynamics simulation of self-diffusion of ionic large solute molecule in modeled polyelectrolyte gel,” *Journal of the Physical Society of Japan*, vol. 81, p. SA010, Nov. 2012.

[39] A. Wedemeier, H. Merlitz, C.-X. Wu, and J. Langowski, “Modeling diffusional transport in the interphase cell nucleus,” *The Journal of Chemical Physics*, vol. 127, no. 4, p. 045102, 2007.

[40] A. Godec, M. Bauer, and R. Metzler, “Collective dynamics effect transient subdiffusion of inert tracers in flexible gel networks,” *New Journal of Physics*, vol. 16, p. 092002, Sept. 2014.

[41] N. Kamerlin and C. Elvingson, “Tracer diffusion in a polymer gel: simulations of static and dynamic 3d networks using spherical boundary conditions,” *Journal of Physics: Condensed Matter*, vol. 28, p. 475101, Nov. 2016.

[42] H. Risken, *The Fokker-Planck Equation: Methods for Solution and Application.* Springer, 3 ed., 1996.

[43] A. Jain, P. Sunthar, B. Dünweg, and J. R. Prakash, “Optimization of a Brownian-dynamics algorithm for semidilute polymer solutions,” *Physical Review E*, vol. 85, p. 066703, June 2012.

[44] A. J. Banchio and J. F. Brady, “Accelerated stokesian dynamics: Brownian motion,” *The Journal of Chemical Physics*, vol. 118, p. 10323, June 2003.

[45] Y. Cu and W. Saltzman, “Controlled surface modification with poly (ethylene) glycol enhances diffusion of plga nanoparticles in human cervical mucus,” *Molecular pharmaceutics*, vol. 6, no. 1, pp. 173–181, 2009.

[46] X. Yang, K. Forier, L. Steukers, S. Van Vlierberghe, P. Dubruel, K. Braeckmans, S. Glorieux, and H. J. Nauwynck, “Immobilization of pseudorabies virus in porcine tracheal respiratory mucus revealed by single particle tracking.,” *PloS One*, vol. 7, p. e51054, Jan. 2012.

[47] B. S. Schuster, J. S. Suk, G. F. Woodworth, and J. Hanes, “Nanoparticle diffusion in respiratory mucus from humans without lung disease,” *Biomaterials*, vol. 34, no. 13, pp. 3439–3446, 2013.

[48] S. K. Lai, Y.-Y. Wang, K. Hida, R. Cone, and J. Hanes, “Nanoparticles reveal that human cervicovaginal mucus is riddled with pores larger than viruses.,” *Proceedings of the National Academy of Sciences of the United States of America*, vol. 107, pp. 598–603, Jan. 2010.

[49] S. K. Lai, J. S. Suk, A. Pace, Y.-Y. Wang, M. Yang, O. Mert, J. Chen, J. Kim, and J. Hanes, "Drug carrier nanoparticles that penetrate human chronic rhinosinusitis mucus.," *Biomaterials*, vol. 32, pp. 6285–90, Sept. 2011.

[50] B. Amsden, "An obstruction-scaling model for diffusion in homogeneous hydrogels," *Macromolecules*, vol. 32, pp. 874–879, Feb. 1999.

[51] S. P. Zustiak, H. Boukari, and J. B. Leach, "Solute diffusion and interactions in cross-linked poly(ethylene glycol) hydrogels studied by fluorescence correlation spectroscopy.," *Soft Matter*, vol. 6, pp. 3609–3618, Aug. 2010.

[52] T. Canal and N. A. Peppas, "Correlation between mesh size and equilibrium degree of swelling of polymeric networks.," *Journal of biomedical materials research*, vol. 23, pp. 1183–93, Oct. 1989.

[53] M. Jardat, B. Hribar-Lee, and V. Vlachy, "Self-diffusion of ions in charged nanoporous media," *Soft Matter*, vol. 8, no. 4, p. 954, 2012.

[54] X. Zhang, J. Hansing, R. R. Netz, and J. E. DeRouchey, "Particle transport through hydrogels is charge asymmetric.," *Biophysical Journal*, vol. 108, pp. 530–9, Feb. 2015.

[55] J. Israelachvili, *Intermolecular and Surface Forces*. Intermolecular and Surface Forces, Elsevier Science, 2010.

[56] R. R. Netz and J. Joanny, "Adsorption of semiflexible polyelectrolytes on charged planar surfaces: charge compensation, charge reversal, and multilayer formation," *Macromolecules*, vol. 32, no. 26, pp. 9013–9025, 1999.

[57] M. Jardat, B. Hribar-Lee, and V. Vlachy, "Self-diffusion coefficients of ions in the presence of charged obstacles," *Physical Chemistry Chemical Physics*, vol. 10, pp. 449–57, Jan. 2008.

[58] H. Risken, *The Fokker-Planck Equation: Methods fo Solution and Application*. Springer, 3 ed., 1996.

[59] P. Hänggi and M. Borkovec, "Reaction-rate theory: fifty years after kramers," *Reviews of Modern Physics*, vol. 62, pp. 251–341, Apr. 1990.

[60] S. K. Ghosh, A. G. Cherstvy, and R. Metzler, "Non-universal tracer diffusion in crowded media of non-inert obstacles.," *Physical Chemistry Chemical Physics*, vol. 17, pp. 1847–58, Jan. 2015.

[61] M. Hinczewski, X. Schlagberger, M. Rubinstein, O. Krichevsky, and R. R. Netz, "End-monomer dynamics in semiflexible polymers.," *Macromolecules*, vol. 42, pp. 860–875, Jan. 2009.

[62] G. G. Putzel, M. Tagliazucchi, and I. Szleifer, "Nonmonotonic diffusion of particles among larger attractive crowding spheres," *Physical Review Letters*, vol. 113, p. 138302, Sept. 2014.

[63] A. Michelman-Ribeiro, F. Horkay, R. Nossal, and H. Boukari, "Probe diffusion in aqueous poly(vinyl alcohol) solutions studied by fluorescence correlation spectroscopy.," *Biomacromolecules*, vol. 8, pp. 1595–600, May 2007.

[64] M. Kanduč, E. Schneck, and R. R. Netz, "Attraction between hydrated hydrophilic surfaces," *Chemical Physics Letters*, vol. 610-611, pp. 375–380, Aug. 2014.

[65] D. S. Tsai and W. Strieder, "Effective conductivities of random fiber beds," *Chemical Engineering Communications*, vol. 40, pp. 207–218, Apr. 1986.

[66] G. D. J. Phillies, "The hydrodynamic scaling model for polymer self-diffusion," *The Journal of Physical Chemistry*, vol. 93, pp. 5029–5039, June 1989.

[67] G. Modesti, B. Zimmermann, M. Börsch, A. Herrmann, and K. Saalwächter, "Diffusion in model networks as studied by nmr and fluorescence correlation spectroscopy.," *Macromolecules*, vol. 42, pp. 4681–4689, July 2009.

[68] M. Abdulkarim, N. Agulló, B. Cattoz, P. Griffiths, A. Bernkop-Schnürch, S. G. Borros, and M. Gumbleton, "Nanoparticle diffusion within intestinal mucus: Three-dimensional response analysis dissecting the impact of particle surface charge, size and heterogeneity across polyelectrolyte, pegylated and viral particles," *European Journal of Pharmaceutics and Biopharmaceutics*, vol. 97, pp. 230–238, Nov. 2015.

[69] Y. Wang, S. Lai, and J. Suk, "Addressing the peg mucoadhesivity paradox to engineer nanoparticles that "slip" through the human mucus barrier," *Angewandte Chemie International Edition*, pp. 9726–9729, 2008.

[70] L. J. Colwell, M. P. Brenner, and K. Ribbeck, "Charge as a selection criterion for translocation through the nuclear pore complex.," *PLoS Computational Biology*, vol. 6, p. e1000747, Apr. 2010.

[71] J. Hansing, C. Ciemer, W. K. Kim, X. Zhang, J. E. DeRouchey, and R. R. Netz, "Nanoparticle filtering in charged hydrogels: Effects of particle size, charge asymmetry and salt concentration," *The European Physical Journal E*, vol. 39, no. 5, p. 53, 2016.

[72] S. Lai, Y. Wang, D. Wirtz, and J. Hanes, "Micro-and macrorheology of mucus," *Advanced drug delivery reviews*, vol. 61, no. 2, pp. 86–100, 2009.

[73] E. M. Johnson, D. A. Berk, R. K. Jain, and W. M. Deen, "Hindered diffusion in agarose gels: test of effective medium model.," *Biophysical Journal*, vol. 70, pp. 1017–23, Feb. 1996.

[74] S. Seiffert and W. Oppermann, "Diffusion of linear macromolecules and spherical particles in semidilute polymer solutions and polymer networks," *Polymer*, vol. 49, no. 19, pp. 4115–4126, 2008.

[75] D. S. Clague and R. J. Phillips, "Hindered diffusion of spherical macromolecules through dilute fibrous media," *Physics of Fluids*, vol. 8, p. 1720, July 1996.

[76] J. Tong and J. L. Anderson, "Partitioning and diffusion of proteins and linear polymers in polyacrylamide gels.," *Biophysical Journal*, vol. 70, pp. 1505–13, Mar. 1996.

[77] I. H. Park, C. S. Johnson, and D. A. Gabriel, "Probe diffusion in polyacrylamide gels as observed by means of holographic relaxation methods: search for a universal equation," *Macromolecules*, vol. 23, pp. 1548–1553, Sept. 1990.

[78] C. E. Castro, F. Kilchherr, D.-N. Kim, E. L. Shiao, T. Wauer, P. Wortmann, M. Bathe, and H. Dietz, "A primer to scaffolded dna origami," *Nature Methods*, vol. 8, pp. 221–229, Mar. 2011.

[79] A. Wedemeier, H. Merlitz, C.-X. Wu, and J. Langowski, "How proteins squeeze through polymer networks: A cartesian lattice study," *The Journal of Chemical Physics*, vol. 131, no. 6, p. 064905, 2009.

[80] P.-O. Gendron, F. Avaltroni, and K. J. Wilkinson, "Diffusion coefficients of several rhodamine derivatives as determined by pulsed field gradient–nuclear magnetic resonance and fluorescence correlation spectroscopy," *Journal of Fluorescence*, vol. 18, no. 6, p. 1093, 2008.

[81] S. Maiti, U. Haupts, and W. W. Webb, "Fluorescence correlation spectroscopy: Diagnostics for sparse molecules," *Proceedings of the National Academy of Sciences*, vol. 94, no. 22, pp. 11753–11757, 1997.

[82] S. T. Hess, S. Huang, A. A. Heikal, and W. W. Webb, "Biological and chemical applications of fluorescence correlation spectroscopy: A review," *Biochemistry*, vol. 41, no. 3, pp. 697–705, 2002. PMID: 11790090.

[83] E. L. Elson and D. Magde, "Fluorescence correlation spectroscopy. i. conceptual basis and theory," *Biopolymers*, vol. 13, no. 1, pp. 1–27, 1974.

[84] M. Eigen and R. Rigler, "Sorting single molecules: application to diagnostics and evolutionary biotechnology," *Proceedings of the National Academy of Sciences*, vol. 91, no. 13, pp. 5740–5747, 1994.

[85] T. Cherdhirankorn, A. Best, K. Koynov, K. Peneva, K. Muellen, and G. Fytas, "Diffusion in polymer solutions studied by fluorescence correlation spectroscopy.," *The Journal of Physical Chemistry B*, vol. 113, pp. 3355–9, Mar. 2009.

[86] C. Guizard, H. Chanzy, and A. Sarko, "Molecular and crystal structure of dextrans: a combined electron and x-ray diffraction study. 1. the anhydrous, high-temperature polymorph," *Macromolecules*, vol. 17, no. 1, pp. 100–107, 1984.

[87] S. S. Olmsted, J. L. Padgett, A. I. Yudin, K. J. Whaley, T. R. Moench, and R. A. Cone, "Diffusion of macromolecules and virus-like particles in human cervical mucus.," *Biophysical Journal*, vol. 81, pp. 1930–7, Oct. 2001.

[88] R. I. Cukier, "Diffusion of Brownian spheres in semidilute polymer solutions," *Macromolecules*, vol. 17, pp. 252–255, Mar. 1984.

[89] O. Lieleg, C. Lieleg, J. Bloom, C. B. Buck, and K. Ribbeck, "Mucin biopolymers as broad-spectrum antiviral agents.," *Biomacromolecules*, vol. 13, pp. 1724–32, June 2012.

[90] L. Johansson, U. Skantze, and J. E. Löfroth, "Diffusion and interaction in gels and solutions. 6. charged systems," *The Journal of Physical Chemistry*, vol. 97, pp. 9817–9824, Sept. 1993.

[91] A. Wedemeier, H. Merlitz, and J. Langowski, "Anomalous diffusion in the presence of mobile obstacles," *EPL (Europhysics Letters)*, vol. 88, p. 38004, Nov. 2009.

[92] T. Zhou and S. B. Chen, "A Brownian dynamics study on the self-diffusion of charged tracers in dilute polyelectrolyte solutions," *The Journal of Chemical Physics*, vol. 122, p. 124905, Mar. 2005.

[93] J. Hansing and R. R. Netz, "Particle trapping mechanisms are different in spatially ordered and disordered interacting gels," *Biophysical Journal*, vol. 114, no. 11, pp. 2653 – 2664, 2018.

[94] L. Durlofsky, J. F. Brady, and G. Bossis, "Dynamic simulation of hydrodynamically interacting particles," *Journal of Fluid Mechanics*, vol. 180, pp. 21 – 49, Apr. 1987.

[95] J. F. Brady, R. J. Phillips, J. C. Lester, and G. Bossis, "Dynamic simulation of hydrodynamically interacting suspensions," *Journal of Fluid Mechanics*, vol. 195, pp. 257–280, Apr. 1988.

[96] C. W. J. Beenakker, "Ewald sum of the rotne–prager tensor," *The Journal of Chemical Physics*, vol. 85, p. 1581, Aug. 1986.

[97] R. Shogren, T. A. Gerken, and N. Jentoft, "Role of glycosylation on the conformation and chain dimensions of O-linked glycoproteins: light-scattering studies of ovine submaxillary mucin," *Biochemistry*, vol. 28, pp. 5525–5536, jun 1989.

[98] D. J. Jeffrey and Y. Onishi, "Calculation of the resistance and mobility functions for two unequal rigid spheres in low-reynolds-number flow," *Journal of Fluid Mechanics*, vol. 139, pp. 261–290, Apr. 1984.

Abstract

Understanding particle transport in hydrogels is an important step for the development of advanced drug delivery techniques. A large body of experimental research has shown that besides excluded volume effects and hydrodynamics, other nonsteric particle-gel interactions can also determine particle mobility in hydrogels. In this thesis, we aim to systematically investigate the effect of long-ranged repulsive or attractive particle-gel interactions on the particle mobility and to determine general particle diffusion mechanisms in hydrogels. For this, we present general models to simulate diffusion of particles in gels with different particle-gel interactions.

First, we introduce a model for the diffusion of particles smaller than the mesh size in hydrogels with electrostatic particle-gel interactions. The gel is comprised of a spatially ordered, cubic symmetric fiber lattice. The diffusive behavior is highly charge asymmetric: Particles are slowed down more strongly by attractive than by repulsive electrostatic interactions. Furthermore, the particle mobility is highly sensitive to the ionic strength, particularly for electrostatic attraction, in agreement with experimental data.

Second, we examine the effect of spatial disorder of the polymer lattice on the particle diffusive behavior. The effect of spatial disorder is linked to the presence of long-ranged particle-gel interactions. For repulsive interactions, an intermediate degree of disorder minimizes the particle mobility inside the gel but for high degrees of disorder, the diffusivity increases again. For attractive interactions, disorder slows down diffusion since particles are immobilized in regions with locally increased fiber density. A comparison between simulations with spatially disordered gels and published experimental data reveals qualitative agreement.

Third, we extend our model to simulate the diffusion of particles in heterogeneous gels with mixed electrostatically attractive and repulsive interaction sites, as relevant for biological hydrogels. Mixed interaction sites are modeled with a random distribution of attractive and repulsive fiber sections. Interaction disorder, in the form of randomly mixed interaction sites, and spatial disorder have a qualitatively similar effect on the particle diffusivity. Charged particles of either sign are immobilized, since attractive particle-gel interactions determine the diffusive behavior. Qualitative agreement between simulation and experiments carried out by our collaborators from the group of Prof. Dr. DeRouchey is found.

Finally, we examine the effect of hydrodynamic interactions in conjunction with long-ranged particle-gel interactions. Repulsive interactions decrease the effect of hydrodynamic interactions on the particle diffusivity, whereas attractive interactions increase the effect of hydrodynamic interactions, due to spatial particle-fiber correlations.

With our simulations we elucidate the effects of various model features such as spatial disorder, interaction disorder and hydrodynamic interactions on the particle mobility and the detailed microscopic mechanisms governing particle diffusion in hydrogels.

Zusammenfassung

Die Diffusion von Partikeln in Hydrogelen ist die Grundlage vieler wichtiger biologischer Prozesse. Die extrazelluläre Matrix, zum Beispiel, reguliert den Austausch von Proteinen, Ionen und Molekülen zwischen Zellen, Schleim schützt den Körper vor Krankheitserregern. Experimentelle Studien belegen, dass die Mobilität von Partikeln in Hydrogelen stark durch verschiedene Arten der Wechselwirkung zwischen den Partikeln und dem Gel bestimmt wird, zum Beispiel sterischer, hydrodynamischer oder elektrostatischer Wechselwirkung. Ziel dieser Arbeit ist es, den Effekt von abstoßenden und anziehenden Partikel-Gel-Wechselwirkungen auf die Partikelmobilität systematisch aufzuklären und allgemeine Mechanismen der Partikeldiffusion in Hydrogelen zu identifizieren. Dazu präsentieren wir verschiedene Simulationsmodelle für die Diffusion von Partikeln in Gelen mit unterschiedlichen Partikel-Gel-Wechselwirkungen.

Zuerst untersuchen wir die Diffusion eines Nanopartikels in Hydrogel mit elektrostatischer Partikel-Gel-Wechselwirkung. Das Polymernetzwerk ist als räumlich geordnetes, kubisches Gitter angenähert. Das Diffusionsverhalten des Partikels ist asymmetrisch hinsichtlich seiner Oberflächenladung: Attraktive elektrostatische Wechselwirkung verlangsamt das Partikel stärker als repulsive elektrostatische Wechselwirkung. Darüber hinaus wird die Beweglichkeit des Partikels stark durch die Salzkonzentration beeinflusst, in Übereinstimmung mit experimentellen Ergebnissen. Zweitens untersuchen wir, wie sich räumliche Unordnung des Polymernetzwerks auf das Diffusionsverhalten des Partikels auswirkt. Im Beisein attraktiver oder repulsiver elektrostatischer Partikel-Gel-Wechselwirkung, hat räumliche Unordnung einen großen Einfluss auf die Partikelbewegung. Bei abstoßender Wechselwirkung minimiert ein mittlerer Grad an Unordnung die Partikelmobilität innerhalb des Gels. Bei anziehender Wechselwirkung wird die Diffusion des Partikels stark verlangsamt, da Teilchen in Regionen mit lokal erhöhter Polymerdichte immobilisiert werden. Simulationen mit räumlich ungeordneten Gelen stimmen mit publizierten experimentellen Daten qualitativ überein. Drittens simulieren wir die Diffusion von Partikeln in Hydrogelen mit einer Kombination aus attraktiver und repulsiver elektrostatischer Wechselwirkung zwischen dem Partikel und dem Gel. In Übereinstimmung mit Experimenten zeigen wir, dass sowohl positiv als auch negativ geladene Partikel in gemischt anionischen/kationischen Gelen immobilisiert werden, da attraktive Partikel-Gel-Wechselwirkungen das diffusive Verhalten bestimmen. Schließlich untersuchen wir den Effekt hydrodynamischer Wechselwirkung in Verbindung mit elektrostatischer Partikel-Gel-Wechselwirkung. Repulsive elektrostatische Wechselwirkung verringert den Einfluss von Hydrodynamik auf den Diffusionskoeffizienten des Partikels, während attraktive elektrostatische Wechselwirkung den Einfluss von Hydrodynamik verstärkt. Zusammengefasst, zeigen unsere Simulationen, dass sich die diffusive Bewegung von Partikeln in komplexen Hydrogelen durch vereinfachte Simulationsmodelle gut annähern lässt.

Erklärung

Hiermit erkläre ich, dass ich die vorliegende Dissertationsschrift mit dem Titel

Particle Trapping Mechanisms in Biological Hydrogels

selbständig angefertigt und hierfür keine anderen als die angegebenen Hilfsmittel verwendet habe. Die Arbeit ist weder in einem früheren Promotionsverfahren angenommen noch als ungenügend beurteilt worden.

Berlin, den 22. Mai 2018

Danksagung

Ich bedanke mich bei allen, die mich während der letzten Jahre bei der Anfertigung meiner Doktorarbeit unterstützt haben. Insbesondere möchte ich mich bei meinem Doktorvater Prof. Roland Netz bedanken, für die Betreuung und dass er diese Arbeit ermöglicht hat, und bei meiner Frau Anna, für ihre Unterstützung im Privaten.

Darüber hinaus bedanke ich mich für die Zusammenarbeit bei meinen Kooperationspartnern Prof. Jason DeRouchey, Xiaolu Zhang, Catrin Ciemer, Dr. Won Kyu Kim, Joseph R. Duke III und Emily B. Fryman. Meinen ehemaligen Kollegen in der AG Netz danke ich für die tolle Arbeitsatmosphäre und die vielen netten Gespräche. Außerdem bedanke ich mich bei Annette Schumann-Welde für ihre Hilfsbereitschaft und Unterstützung.

Ich möchte mich auch bei meinen Eltern bedanken, für ihre Unterstützung, und bei meinen Kindern dafür, dass sie so viel Glück in mein Leben bringen und außerdem immer dafür sorgen, dass ich morgens nicht verschlafe.